CIVIL ENGINEERING JOURNAL

číslo 1/2023

Obsah:

CIVIL ENGINEERING JOURNAL

Article no. 1

THE CIVIL ENGINEERING JOURNAL 1-2023

POSSIBLE APPROACHES FOR PROCESSING OF SPHERICAL IMAGES USING SFM

David Zahradník and Jakub Vynikal

Czech Technical University in Prague, Faculty of Civil Engineering, Department of Geomatics, Thákurova 7, Praha 6, Czech Republic; david.zahradnik@fsv.cvut.cz, jakub.vynikal@fsv.cvut.cz

ABSTRACT

Spherical cameras are being used more frequently in surveying because of their low cost and possibility to process spherical images with conventional Structure from Motion (SfM) method. Fish-eye lenses are now frequently found on modern 360° cameras, allowing for the capture of the entire scene and subsequent model reconstitution by a non-photogrammetrist specialist. Gyrospherics are a feature of cameras that ensure image stabilization to reduce blur when the camera is moving. This feature allows it to capture moving scenes in time-lapse mode. However, two main factors - hardware parameters and software algorithms - affect the quality of the images that are captured. The 360° camera design allows for a variety of data processing methods by SfM. These images were created using multiple image sensors and lenses from each 360° camera. These images can be processed individually or by applying rules to define relationships between images. Also, images from cameras can be stitched and processed with a spherical camera model. In this paper is proposed processing methods of data from 360° cameras and estimated accuracy of each method.

KEYWORDS

Spherical camera, 360 cameras, SfM, Agisoft

INTRODUCTION

Spherical cameras are mainly used for virtual tours to visualize the first-person perspective from a computer. These applications are used both indoors and outdoors for navigation. The advantage of this type of camera is that it captures the overall view by stitching together multiple images with a large field of view (FOV). Most low-cost 360° cameras on the market contain two image sensors with fisheye lenses.

Spherical images can also be used for photogrammetry. Their capabilities in this field are currently tested in indoor modelling, heritage documentation, street mapping and many more use-cases. While the quality of low-cost spherical camera footage can't compete with DSLR cameras, the omni-directional field of view is quite useful for alignment or connecting areas modelled with conventional frame cameras.

Some problems arise from the use of spherical images, the construction of the cameras, the non-identical centre of projection and the excessive distortion of the fisheye lenses, which leads to blurring at the edges of images. The distortion of composite panoramic images cannot be characterized with a standard distortion model (Brown etc.) [1] for planar/fisheye lenses for SfM. The inability to correct for lens distortion can be a serious problem in accurate reconstruction. One solution to mitigate this problem is to split the source images between the two original fisheye cameras and evaluate the alignment along with their internal parameters. In this paper, a comparison of different processing methods of data from spherical cameras is proposed.

The reason for the comparison is the increasing use of spherical cameras in surveying [3], [4], [5]. It is also a cheaper alternative to mobile mapping using simultaneous localisation and mapping (SLAM) technology [6], [7]. The accuracy of the results of SfM from spherical images is comparable to mobile mapping with SLAM in places with good light conditions and abundant features with distinct texture (unlike white walls). The advantages of using spherical imagery, such as low cost, fast data collection and guaranteed overlap, provide an interesting alternative for mobile mapping. [3], [8], [9], [10].

Video capture is the optimal option to achieve the same mobility as SLAM technology. Conventional photography is the better option for image quality, but as time intervals between photos are too long, better overlap can be more desirable than higher image quality. To achieve sufficient overlap, it is better to set the frequency of the images to 0.5s. Previous experience shows that images with an interval larger than 1s can be hard to process [7]. Insta360 cameras also offer Interval camera mode, which takes regular photos every fixed time interval. However, the shortest possible interval is 3s, which as mentioned is way too long.

Next problem with spherical images is the stitching step. Stitching has an impact on results of SfM. Some software does not differentiate the project centre of images, this causes inaccuracies of SfM methods [11]. Other possibilities allow calibrating spherical cameras to achieve interior orientation parameters (IOPs) and exterior orientation parameters (EOPs) of each individual's lens [12]. In this paper, we explore some of the possible reconstruction approaches with regards to stitching, evaluating their accuracy, reliability and convenience. One of the questions answered is whether to process the footage already stitched as a spherical photo (with discontinuity and resulting error along the seamline), or to process them unstitched as fisheye cameras.

METHODS

Material

Two devices were used for data collection. The first device, made of inexpensive components, will be referred to as the camera rig later in the text. Four Raspberry Pi HQ cameras with fisheye lenses were used for the camera rig. The camera sensor used is an IMX477R with 12.3 MP resolution. The pixel size of the camera sensor is 1.55 μm. The lens used has a variable focal length from 2.8 mm to 12 mm. The corresponding field of view ranges from 43° to 125°. During the measurement, the lenses were set to 3.4 mm focal length. The cameras are controlled sequentially by the Raspberry Pi4B to capture one image at a time. The device is not able to capture all four images at the same time because the port on the Raspberry control unit only communicates with one camera at a time. To take a picture, one camera must be active and the others must be set off.

The second device was a commercial 360° camera Insta360 One RS with a 360° module that covers the entire 360x180° scene and consists of two fisheye sensors. The spherical images of the 360° module have resolution of 18 MPx and size of 6080x3040 px. The pixel size of the camera sensor is 1.2 μm, lens with 7.2 mm equiv. focal length and F2.0. The camera is equipped with a gyroscope to achieve image stabilization in all conditions.

Fig. 1 – Camera rig (left) Insta360 One RS (right)

Case study

Testing took place in the laboratory of calibrations of surveying equipment. The laboratory is part of the Faculty of Civil Engineering at CTU in Prague and the laboratory is 27m long and 7.5m wide. Coded targets were set around the laboratory on the walls to be used as control and check points.

First operation was to define the reference system of coded targets. Concrete columns with joints for total stations are placed in line at the centre of the laboratory. One of the columns was set as the origin of the reference system and the link to the farthest column was set as the interlaced horizontal axis. Coded targets were measured with Leica TCR 403 from columns to obtain coordinates with accuracy of 3 mm+2 ppm in distance measurement and 3' in angle measurement. Final spatial accuracy for a target was 3mm. Three targets were used as control points, remaining 27 targets were used as check points for estimations of accuracy

Measurement methods

The measurement method utilized in this paper contradicts the photogrammetry recommendation for SfM. Data collected primarily along the centreline of the laboratory are unsuitable for SfM processing. SfM requires high overlap between images and, for improved accuracy, images captured from different angles. Methods in this paper presume high image overlaps, but images are in the same perspective with quite large leaps between them. Another drawback is that the target (the room) is not surrounded by images and images are not captured from different angles. This can lead to insufficient data for successful alignment. Reconstructed objects are floor, walls and ceiling.

Two approaches were used for data acquisition by camera rig with larger and smaller distances between rig positions.

Positions with larger gaps were predefined by columns in the laboratory. Distance between columns is from 1 to 1.5 meters. Camera images were captured from two angles of the camera rig rotated by 45°, thus the total number of images from one position was 8. The reason for this is that only 4 images with such a small overlap were not sufficient to be processed by SfM. Ten positions with eight images each were captured during measurement.

Second approach used positions 0.5 meters apart with each position containing 4 images. Direction of the images aimed to the middle between the axes. Main quadrant is defined as the direction of measurement and as the axis of the reference system. A total of twenty-two positions were measured in the line defined by the columns.

Data from the Insta360 camera was captured using a time-lapse function every 0.5 seconds, with all recording flow stabilization turned on. Each image was corrected by pitch and roll values from the gyroscope. Camera was mounted on a helmet and the two approaches were used: the same line track was used as for the camera rig and it was used as the maximum allowed track in the

laboratory for capturing time-lapse video. Camera lenses were heading perpendicular to the capturing direction to minimize lens distortion issue on closed objects in the scene.

Fig. 2 – unprocessed Insta360 fisheye images

Processing methods

Data was processed using four methods to estimate its accuracy. Two image datasets were captured and each dataset was processed using these methods. Methods differ in the choice of camera settings: free, station, master-slave camera and spherical. Each method is standardly processed in the Agisoft Metashape workflow.

Video-sequence from time-lapse mode on Insta360 One RS is in insv format, which is mp4 video format with metadata from gyroscope and camera information for stitching. To extract spherical frames, the files must be stitched in Insta360 Studio software. After stitching, users are able to export 360 time-lapse videos to mp4 format to extract the individual frames. Time-lapse mode does not allow saving images like images, instead images are saved to video sequence with 29.97 fps. To use the individual images from each fisheye sensor, insv files must be renamed to mp4 format. After renaming, it is possible to extract individual frames from each sensor.

Photos from the Raspberry HQ camera are processed like jpg images. Agisoft Metashape was used for spherical images stitching and panorama export, with images from the same position in one folder, which is set as a station.

Individual (free) camera images are processed with the “Align photos” function in Agisoft Metashape. Each image is individually represented by position and orientation. Alignment accuracy was set to High, detected points were set to 40 000 key points per image, filtered to 5 000 tie points. Station cameras contain images taken from the same position. Images from the same station have the same image center. Orientation is independent and is estimated by aligned photos. To use the station option, images from the same position must be separated into subfolders. Subfolder in the project is marked as a station, so in the alignment process camera positions from the subfolder are the same.

Master-slave camera approach works with images taken at the same time, but compared to the station option, image centres are not the same. Master-slave option allows to predefine relative position and orientation between images on one camera rig. This option is suitable for multiple camera systems with two and more cameras with different offsets. One of the cameras is set as master and the others as slave. Orientation and position of slave cameras is related to the master camera. With calibrated relative position and orientation, the processes of Structure from Motion

should be faster. To use the master-slave approach, images of each camera must be separated into subfolders and must be in alphabetical order. Agisoft Metashape automatically allows importing photos in such folders as a multi-camera system.

Spherical images are the product of stitching multiple individual images. The mathematical model for spherical images of Agisoft Metashape [21] consists only of:

$$u = \frac{1}{2}w + \frac{w}{2\pi}\frac{X}{Z} \qquad v = \frac{1}{2}w + \frac{w}{2\pi}\frac{Y}{\sqrt{X^2+Y^2}} \tag{1}$$

where (X, Y, Z) are the point coordinates in the local camera coordinate system. As the spherical model doesn't take in account any other variable, distortion and dispositions of the image centre can only be eliminated before stitching in the fisheye model.

All images were set to fisheye type, except for spherical images. The lens on the Insta360 One RS and the camera rig have high distortion, which shows up as chromatic aberration and other lens flaws. Images taken with the Raspberry HQ Camera captured in the lab at 4 meters distance result in sampling distance of 1.6mm. At the same distance, the Insta360 One sampling distance was 3.6mm.

Three control points from measured coded targets were used as references for each approach. Control points were evenly spaced across the lab, and two of them were positioned at the beginning and at the end of the laboratory wall, which is parallel to the capturing line track. Due to lens distortion, the perpendicular wall on the capturing line track was not chosen. The third control point was placed in the middle of the wall opposite the wall with the other two control points.

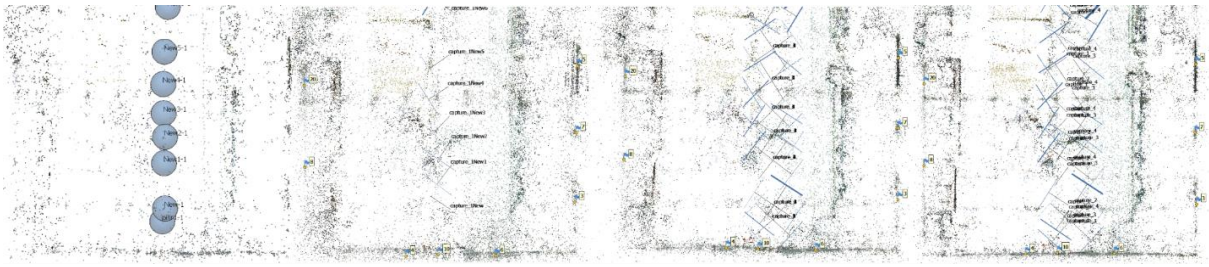

Fig. 3 – Camera rig (spherical, master-slave, station, free, left to right)

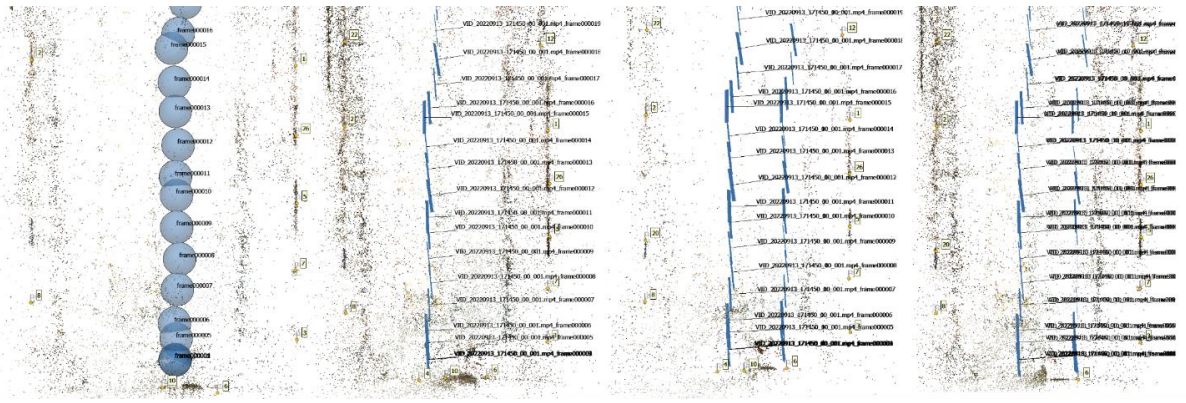

Fig. 4 – Insta360 (spherical, master-slave, station, free, left to right)

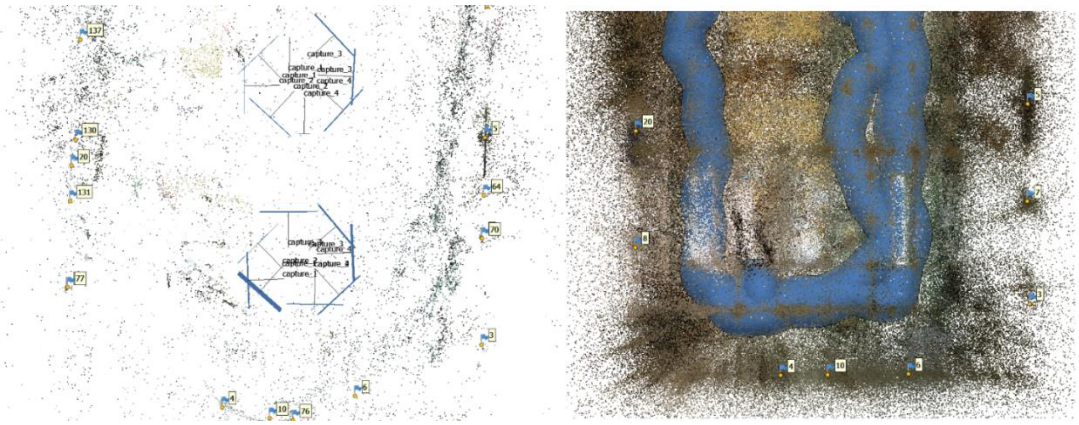

Fig. 5 – Raspberry HQ camera - 8 images station (left), Insta360 one rs - long track (right)

RESULTS

The data obtained from Raspberry PI HQ cameras and Insta360 One RS were examined and validated by position differences on checkpoints. Check points were always marked at least on four close images. Coded maskers had to be manually targeted on some images because of small image resolution. Large lens distortion and small image resolution make it difficult to automatically detect coded markers.

Data was processed on the Lenovo Legion 5 Pro laptop. The laptop contains AMD Ryzen 7 5800H with Radeon Graphics with 32GB ram memory and Nvidia GeForce RTX 3070 Laptop GPU. Process time is related to the working station and can be analysed only relatively. Spherical images from raspberry HQ Camera are 16000x8000 with 18 MB storage size. Original pictures are 4056x3040 with 24MB storage size. Spherical images from Insta360 One RS are 5760x2880 with 12 MB store size. Individual images from each sensor are 2880x2880 with 7 MB storage size. For a small dataset the results are only informative and in the future on a larger dataset the time-consuming data will be rediscovered.

Tab. 1 - Methods processing time

	Methods	**Matching time [s]**	**Alignment time [s]**	**Memory usage [MB]**
Raspberry HQ	spherical	78	3	5500
	master-slave	43	25	530
	station	40	32	530
	free	43	32	650
Insta360	spherical	46	24	400
	master-slave	54	23	720
	station	51	31	450
	free	46	26	400
Raspberry HQ	8x long distance	29	60	550
Insta360	long track	2160	480	1300
	upscale	450	5	12000

The phases of image matching, tie point (TP) extraction, and camera position estimation are primarily responsible for the accuracy on checkpoints.

Dataset from Raspberry HQ camera with eight images per station with longer distance between positions was not properly processed. Cameras closer to walls were discarded from position estimation. Long distance between positions degraded accuracy to more than 1 meter. This method with high overlap from one position is not suitable for further processing and usage.

Dataset from Insta360 with long track and spherical camera methods is comparable with spherical methods from capturing line track. More photos from the same spherical camera did not increase the accuracy of testing objects.

Master-slave and station methods have better accuracy than the spherical method from the Raspberry HQ camera. The cause lies in the stitching phase, where the stitching process in Agisoft Metahape assumes the same image centre. As a result, spherical pictures are incorrectly joined from different angles. The issue is depicted in the figure below.

Fig. 6 – Bad stitching of images from camera rig

Free camera option from Insta360 One RS dataset was not able to process all at one. Small overlap between images from the same position at part of image with high lens distortion excluded one sensor from the Estimation position phase.

Worst results of Raspberry HQ Camera were caused by lenses with changeable focal length. The cameras were not secured with the precisely same focal length. Small variance of focal lens degraded four same images sensors and lenses to four cameras with a bit different camera IOPs.

Best results are shown by the dataset which was processed with a free camera option. Accuracy of the free camera method is 2 times better than other methods from Raspberry HQ Camera. In the case of Insta360, there are not very high differences between processing methods except for the station option. Spherical stitching in insta360 studio is at a good level, so the camera model must count with different images centres and lens distortion. The station option groups images to the same image centre and causes worse accuracy.

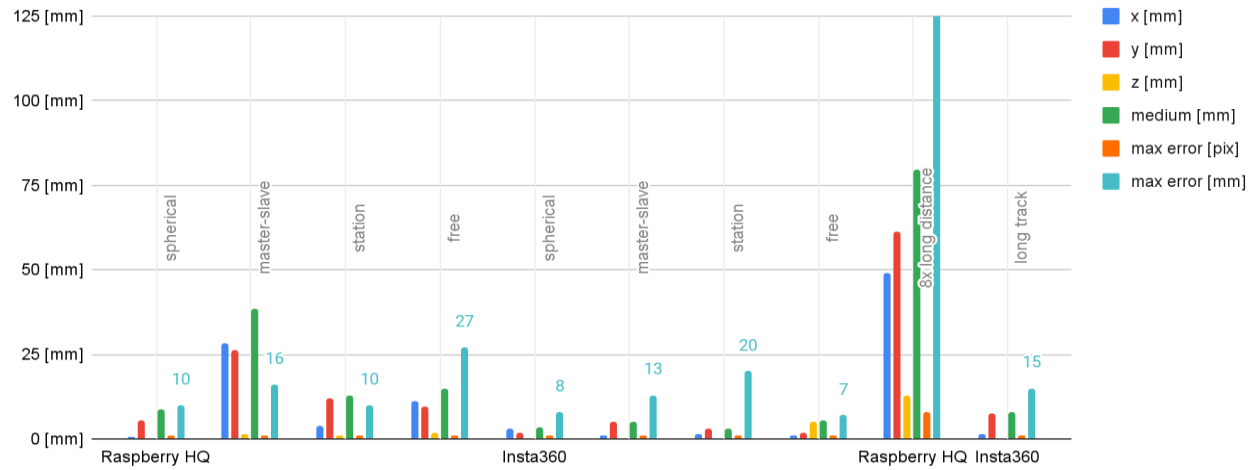

Fig. 7 – Accuracy test – check points

Values x, y and z in Figure 7 and 8 describe errors in individual axes. Medium and max values correspond with x, y and z values.

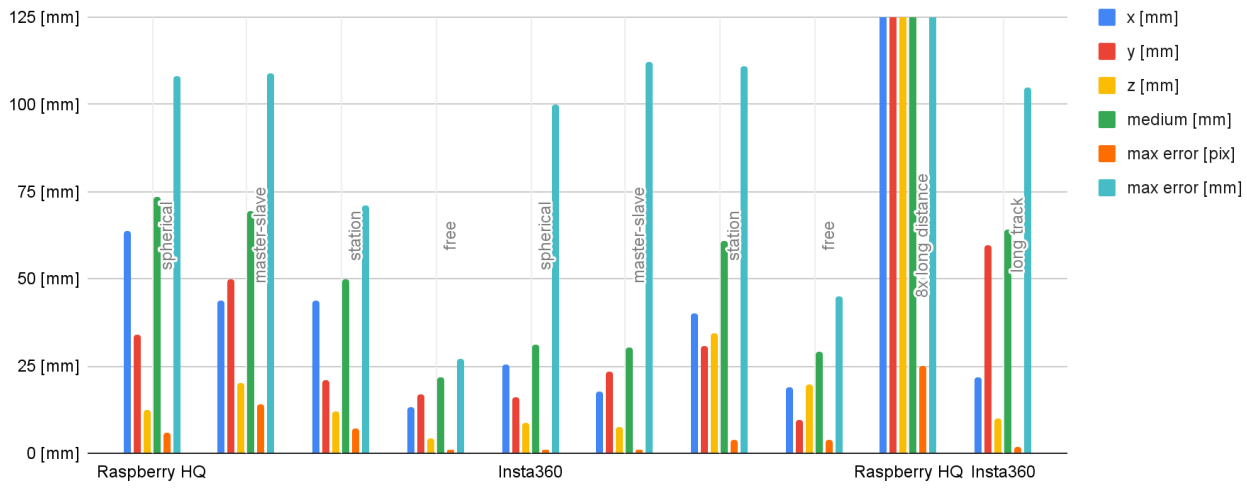

Fig. 8 – Accuracy test – control points

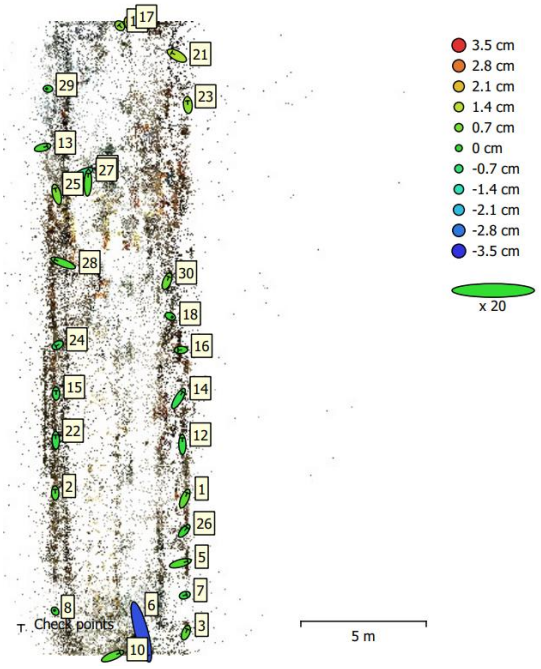

Fig. 9 – Checks and control points position

Check points of each method have the same relative value to corresponding accuracy. The worst accuracy was reached by the checkpoint on the perpendicular wall to capture line track. Hedging of lenses was on a parallel wall with a captured line track, so the checkpoint on this wall has better accuracy (Figure 9).

CONCLUSION

Images were processed with several approaches: free, station, master-slave and spherical option. Free option estimates the position and orientation of images individually. The station option assigns one image centre to images taken from a single position. Master-slave option defines relative position and orientation of images from one camera (master) and applies it to other cameras (slaves). Spherical images created or directly captured were processed as spherical in Agisoft Metashape software.

Best results are achieved with the free method when image position and orientation is independently estimated. Maximal error from camera rig dataset was 27 mm. Better results are achieved by the Insta 360 dataset with a maximum error of 45 mm. Other methods achieve worse results. For the Insta360 camera of the other methods, the maximum error at the control points is twice as large due to the failure to process a series of photos from one side of the camera. For the master-slave method with the camera rig, the maximum error on the control points is three times larger due to differences in IOP's. The individual lenses only had an approximate set focal length. Insta360 has median control point errors of around 30 mm for all methods except station, where the error is doubled. This is caused by the non-identical center of projection of images. Camera rig median control point error for free method is 22 mm. Other methods have more than twice the error due to errors in focal length evaluation.

Check points placed on the edge of images with high lens distortion show worse accuracy than primarily focused check points in image centers.

Mobile mapping with a 360° camera is possible in good light conditions and scenes without homogenous texture, i.e. white walls. 360° cameras with high resolution in good conditions can achieve 3 cm spatial accuracy on a 5–6-meter distance. As the distance increases, the sampling distance decreases and so does the accuracy.

ACKNOWLEDGEMENTS

This work was supported by the Grant Agency of the Czech Technical University in Prague, grants SGS23/052/OHK1/1T/11 and SGS23/050/OHK1/1T/11

REFERENCES

[1] Luhmann, Thomas, et al. *Close-range photogrammetry and 3D imaging*. Walter de Gruyter, 2013.

[2] Pavelka, Karel, Cinzia Pappi, and Karel Pavelka jr. (2021) "Modern Possibilities of Documentation and Replication of Archaeological Finds." The International Archives of Photogrammetry, Remote Sensing and Spatial Information Sciences 46: 531-538.

[3] Castanheiro, L. F., et al. "3D Reconstruction of Citrus Trees Using an Omnidirectional Optical System." 2020 IEEE Latin American GRSS & ISPRS Remote Sensing Conference (LAGIRS). Ieee, 2020.

[4] Abate, D., Toschi, I., Sturdy-Colls, C., Remondino, F., 2017. A low-cost panoramic camera for the 3d documentation of contaminated crime scenes. Int. Arch. Photogramm. Remote Sens. Spatial Inf. Sci., XLII-2/W8, pp. 1–8.

[5] Zhao, C. (2021). Creating point clouds, textured meshed models and orthophotos with Weiss AG Civetta - 230 magapixels 360° HDR camera. Technical Report available on the Internet, https://docplayer.net/209971609-Civetta-agisoft-metashape.html, last accessed December 2021, 5 pages

[6] Teppati Losè, Lorenzo, Filiberto Chiabrando, and Fabio Giulio Tonolo. "Documentation of complex environments using 360 cameras. The Santa Marta Belltower in Montanaro." Remote Sensing 13.18 (2021): 3633.

[7] Pavelka, K., et al. (2022) "Analysis of data joining from different instruments for object modelling." The International Archives of the Photogrammetry, Remote Sensing and Spatial Information Sciences 43: 853-860.

[8] Barazzetti, L., et al. "Connecting inside and outside through 360 imagery for close-range photogrammetry." The International Archives of Photogrammetry, Remote Sensing and Spatial Information Sciences 42 (2019): 87-92.

[9] Barazzetti, L., M. Previtali, and F. Roncoroni. "3D modelling with the Samsung Gear 360." 2017 TC II and CIPA-3D Virtual Reconstruction and Visualization of Complex Architectures. Vol. 42. No. 2W3. International Society for Photogrammetry and Remote Sensing, 2017.

[10] Barazzetti, L., M. Previtali, and F. Roncoroni. "3D MODELING WITH 5K 360° VIDEOS." 9th International Workshop on 3D Virtual Reconstruction and Visualization of Complex Architectures, 3D-ARCH 2022. Vol. 46. No. 2. International Society for Photogrammetry and Remote Sensing, 2022.

[11] Kwiatek, K., Tokarczyk, R., 2015. Immersive Photogrammetry in 3D Modelling. Geomatics and Environmental Engineering, Volume 9, Number 2, pp. 51-62.

[12] Aghayaria, S., Saadatsereshta, M., Omidalizarandi, M., Neumannb, I., 2017. Geometric Calibration of Full Spherical Panoramic Ricoh Theta Camera. In: ISPRS Annals of the Photogrammetry, Remote Sensing and Spatial Information Sciences, Vol. 4(1/W1), pp. 237-245.

[13] Fangi, G. (2017). The book of spherical photogrammetry: Theory and experiences. Edizioni Accademiche Italiane.

[14] Fangi, G., Pierdicca, R., Sturari, M., & Malinverni, E. S. (2018). IMPROVING SPHERICAL PHOTOGRAMMETRY USING 360° OMNI-CAMERAS: USE CASES AND NEW APPLICATIONS. International Archives of the Photogrammetry, Remote Sensing & Spatial Information Sciences, 42(2).

[15] Schneider, D., & Maas, H. G. (2003). Geometric modelling and calibration of a high-resolution panoramic camera. Optical 3-D Measurement Techniques VI, 2, 122-129.

[16] Barazzetti, L., Previtali, M., & Roncoroni, F. (2018). Can we use low-cost 360 degree cameras to create accurate 3D models?. International Archives of the Photogrammetry, Remote Sensing & Spatial Information Sciences, 42(2).

[17] Pisa, C., Zeppa, F., & Fangi, G. (2010, October). Spherical photogrammetry for cultural heritage: san galgano abbey, siena, italy and roman theatre, sabratha, libya. In Proceedings of the second workshop on eHeritage and digital art preservation (pp. 3-6).

[18] Suman, S., Rastogi, U., & Tiwari, R. (2016). Image Stitching Algorithms-A Review. Circulation in Computer Science Vol.1, No.2, pp: (14-18),

[19] Szeliski, R. (2007). Image alignment and stitching: A tutorial. Foundations and Trends® in Computer Graphics and Vision, 2(1), 1-104.

[20] Otero, R., Lagüela, S., Garrido, I., & Arias, P. (2020). Mobile indoor mapping technologies: A review. Automation in Construction, 120, 103399.

[21] Agisoft PhotoScan http://www.agisoft.com

[22] Insta 360 One rs twin edition https://www.insta360cam.cz/insta360-one-r-twin-edition/

[23] Pagani, A., & Stricker, D. (2011, November). Structure from motion using full spherical panoramic cameras. In 2011 IEEE International Conference on Computer Vision Workshops (ICCV Workshops) (pp. 375-382). IEEE.

[24] Kwiatek, K., & Tokarczyk, R. (2014). Photogrammetric applications of immersive video cameras. ISPRS Annals of the Photogrammetry, Remote Sensing and Spatial Information Sciences, 2(5), 211.

[25] Dlesk, Adam, Karel Vach, and Karel Pavelka. (2020) "Structure from motion processing of analogue images captured by rollei metric camera digitized with various scanning resolution."

[26] Dlesk, A., K. Vach, and P. Holubec. (2019) "Analysis of Possibilities of Low-Cost Photogrammetry for Interior Mapping." The International Archives of Photogrammetry, Remote Sensing and Spatial Information Sciences 42: 27-31.

[27] Barazzetti, L. (2022) Metric Rectification of Spherical Images. ISPRS Int. J. Geo-Inf., 11, 248. https://doi.org/10.3390/ijgi11040248

[28] Pagani, Alain, and Didier Stricker. (2011 "Structure from motion using full spherical panoramic cameras." 2011 IEEE International Conference on Computer Vision Workshops (ICCV Workshops)

[29] Pavelka, K., and E. Matoušková. (2019) "THE CONTRIBUTION OF GEOMATIC TECHNOLOGIES TO BIM." International Archives of the Photogrammetry, Remote Sensing & Spatial Information Sciences.

[30] Pavelka, Karel, David Zahradník, and Jaroslav Sedina. (2021) "New Measurement Methods for Structure Deformation and Objects Exact Dimension Determination." IOP Conference Series: Earth and Environmental Science. Vol. 906. No. 1. IOP Publishing

APPENDIX A

Table of test accuracy follows in Figure 7 and 8.

	Methods	points	x [mm]	y [mm]	z [mm]	medium [mm]	max error [pix]	max error [mm]
Raspberry	spherical	control	1	6	0	9	1	10
		checks	64	34	13	73	6	108
	master-	control	28	26	1	38	1	16
	slave	checks	44	50	20	69	14	109
	station	control	4	12	1	13	1	10
		checks	44	21	12	50	7	71
	free	control	11	10	2	15	1	27
		checks	13	17	4	22	1	27
Insta360	spherical	control	3	2	0	4	1	8
		checks	26	16	9	31	1	100
	master-	control	1	5	0	5	1	13
	slave	checks	18	23	7	30	1	112
	station	control	1	3	0	3	1	20
		checks	40	31	34	61	4	111
	free	control	1	2	5	5	1	7
		checks	19	10	20	29	4	27

Raspberry	8x long -	control	49	61	13	80	8	130
	distance	checks	1173	528	133	1294	25	2318
Insta360	long -	control	1	8	0	8	1	15
	track	checks	22	60	10	64	2	105

CIVIL ENGINEERING JOURNAL

Article no. 2

THE CIVIL ENGINEERING JOURNAL 1-2023

STUDY ON REMOTE INTELLIGENT MONITORING SYSTEM OF SLOPE BASED ON SARMA ALGORITHM AND ARCGIS

Jian Gong[1], Kexin Zhang[2], Houji Zhang[3] and Honglei Zhang[3]

1. China Railway Fifth Survey and Design Institute Group Co. LTD, Design Department, Beijing, No.9 Kangzhuang Road, PR of China; 67543320@qq.com

2. Shenyang Jianzhu University, Department of Bridge Engineering, Shenyang, No.25 Hunnan Zhong Road, PR of China; jt_zkx@sjzu.edu.cn

3. Beijing Xinqiao Technology Development Co., Ltd, Bridges and Tunnels Department, Beijing, No.8 Xitucheng, PR of China; Hongleizhang_Xq@163.com, 765310906@qq.com

ABSTRACT

This article is devoted to promote the remote intelligent monitoring system of slope research, reduce the threat of natural disaster to the highway. Firstly, a typical slope on Liu-An highway was selected as the research object. Then, based on the Sarma algorithm and considering the influence factors such as inhomogeneous boundary conditions, water content and reinforcement angle, a slope stability analysis system based on the improved Sarma algorithm is developed to build an engineering geological model and a remote intelligent monitoring system platform for the slope. On this basis, we selected the slope of typical road sections for remote monitoring and pre-warning. ArcGIS technology is used to carry out difference analysis of monitoring data, realize GIS 3D visualization, and verify the 3D visualization monitoring effect of the system. The results show that the system is stable and reliable. The range and precision meet the specification requirements and can effectively realize the 3D visualization monitoring of highway slope. It can also realize four-level pre-warning, which lays a foundation for the long-term safe operation of highway.

KEYWORDS

Highway slope, Sarma algorithm, ArcGIS, 3D visualization, Intelligent monitoring

INTRODUCTION

Since the reform and opening-up, China's highway construction has developed rapidly. By the end of 2019, China's total highway mileage was 5,012,500km, including 149,600km of expressway, 518,600km of trunk highway, and 4,200,500km of rural road. Nearly two thirds of China's land area is mountainous. A considerable part of highways intersperses in the mountains, forming a large number of complex high cutting slopes, which destroy the balance state of the original mountain slope. Natural disasters such as landslide, debris flow and water destruction have become the most serious natural disasters threatening highways, causing serious economic losses [1]. A series of social behaviours, such as mining, explosion and logging, further aggravate the occurrence of highway slope landslide [2].

At present, the United States, Canada, the Netherlands and other countries and regions have developed relatively mature in slope intelligent monitoring and landslide warning. Sensor research and development, geological model calculation, intelligent monitoring system design, disaster warning and long-distance signal transmission have all been widely applied [3-4]. In China, remote

identification, monitoring and pre-warning of highway slopes are still in the stage of theoretical simulation and experimental research and development [5-9]. Slope monitoring methods mainly include deformation monitoring, stress monitoring, water monitoring, rock mass failure acoustic emission monitoring, etc., among which deformation monitoring is the most widely used. Slope monitoring equipment and technology mainly include sensor technology, 3S technology (GPS, GIS, RS), robot technology, time domain reflection technology, perception node network, Internet of things technology, etc.

There are limitations to using these techniques alone. The main reason is that the landslide has many conditions, such as deformation, moisture content, friction resistance in soil body, shear Angle, etc. The development of the remote intelligent slope monitoring system based on Sarma algorithm and ArcGIS technology can "monitor the essence" rather than just "monitor the phenomenon". According to the influencing factors of landslide, the monitoring of non-homogeneous boundary conditions, water content and reinforcement Angle is integrated into the system for analysis, and the calculation model is improved to make the analysis results more consistent with the reality.

MECHANICAL MODEL OF IMPROVED SARMA ALGORITHM

Based on the limit equilibrium theory and homogeneous boundary conditions, Sarma proposed an algorithm for stability analysis of slopes or other structures in 1979, called Sarma algorithm, without considering various drainage conditions and complex stress conditions [10]. He believed that the sliding body should overcome the shear strength of the main sliding surface and its own strength. The sliding body breaks into blocks that can slide relative to each other, and then slide as a whole, rather than forming an ideal sliding camber or plane.

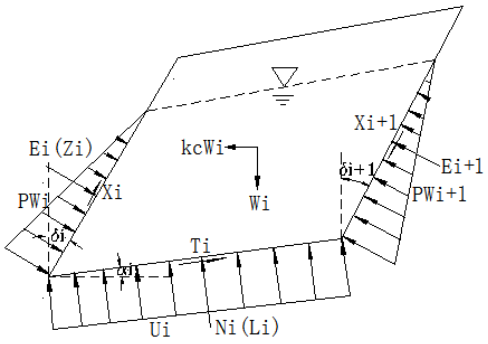

Fig. 1 - Mechanical model based on the Sarma algorithm

According to the mechanical model, when the slope reaches the ultimate equilibrium state under external loads such as earthquake, rain, snow, and vehicles, the equilibrium equation in Table 1 will be established.

Tab. 1 - Parameter list

Parameter	Equation	Number of blocks	Number of Equations
Resultant force along the X axis	$\sum F_x = 0$	N	N
Resultant force along the Y axis	$\sum F_y = 0$	N	N
Resultant moment	$\sum M = 0$	N	N
The bottom slip meets the Moor-Coulomb criterion	$T_i = f(N_i, CB_i, \varphi B_i)$	N	N
The sideslip meets the Moor-Coulomb criterion	$X_i = f(E_i, CS_i, \varphi S_i)$	N	N-1

According to the above equilibrium equation, the formula for solving the stability coefficient (F_s) and critical horizontal seismic coefficient (kc) of the slope is derived and simplified, and the following recursive relation is obtained.

$$E_{i+1} = a_i - p_i \cdot kc + e_i \cdot E_i \tag{1}$$

In the Equation 1, kc is the critical horizontal acceleration coefficient of earthquake, E_i and E_{i+1} are the normal pressure acting on both sides of the i block(kN), a_i, p_i and e_i are constant coefficients, and their values are as follows:

$$a_i = \frac{W_i \cdot \sin(\phi B_i - \alpha_i) + R_i \cdot \cos\phi B_i + S_{i+1} \cdot \sin(\phi B_i - \alpha_i - \delta_{i+1}) - S_i \cdot \sin(\phi B_i - \alpha_i - \delta_i)}{\cos(\phi S_{i+1} - \alpha_i - \delta_{i+1} + \phi B_i) \cdot \sec\phi S_{i+1}} \tag{2}$$

$$p_i = \frac{W_i \cdot \cos(\phi B_i - \alpha_i)}{\cos(\phi S_{i+1} - \alpha_i - \delta_{i+1} + \phi B_i) \cdot \sec\phi S_{i+1}} \tag{3}$$

$$e_i = \frac{\cos(\phi S_i - \alpha_i - \delta_i + \phi B_i) \cdot \sec\phi S_i}{\cos(\phi S_{i+1} - \alpha_i - \delta_{i+1} + \phi B_i) \cdot \sec\phi S_{i+1}} \tag{4}$$

Sarma algorithm cannot be directly applied to the engineering practice, as it cannot solve the problems under the complex geological and hydrological background. Its deficiencies are mainly as follows:

(a) It is only applicable to slope stability calculation under homogeneous boundary condition.
(b) The drainage conditions of the slope are not considered.
(c) The condition of slope load and reinforcement are not considered.
(d) The slope stability calculation and analysis under the combination of multiple working conditions cannot be carried out.

Therefore, it is not enough to consider homogeneous boundary conditions only, but consider homogeneous boundary conditions at the same time. In practical engineering, the water content of soil and various load conditions are relatively complex, and some slopes are reinforced, which should be the parameters of slope stability analysis. Considering various working conditions, Chinese researchers have derived the iterative formula for solving the stability coefficient with slope surface forces, and modified the coefficient as follows [11].

$$a_i = \frac{W_i \cdot \sin(\phi B_i - \alpha_i) + R_i \cdot \cos\phi B_i + S_{i+1} \cdot \sin(\phi B_i - \alpha_i - \delta_{i+1}) - S_i \cdot \sin(\phi B_i - \alpha_i - \delta_i) + F_i \cos(\phi B_i - \gamma_i - \alpha_i)}{\cos(\phi S_{i+1} - \alpha_i - \delta_{i+1} + \phi B_i) \cdot \sec\phi S_{i+1}} \tag{5}$$

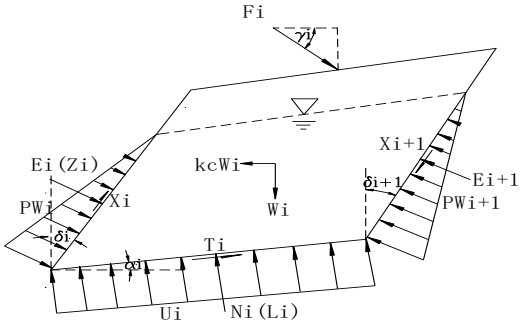

Fig. - 2 Mechanical model based on the improved Sarma algorithm

REMOTE INTELLIGENT MONITORING SYSTEM OF SLOPE

The system composes four parts: data acquisition device, data transmission system, computer analysis and management system and remote monitoring system. It can realize real-time data acquisition and integrated processing, remote control and signal transmission, and four-level pre-warning. At the same time, it can carry out difference analysis of monitoring data based on ArcGIS technology and realize GIS 3D visualization display. The working principle is shown in Figure 3.

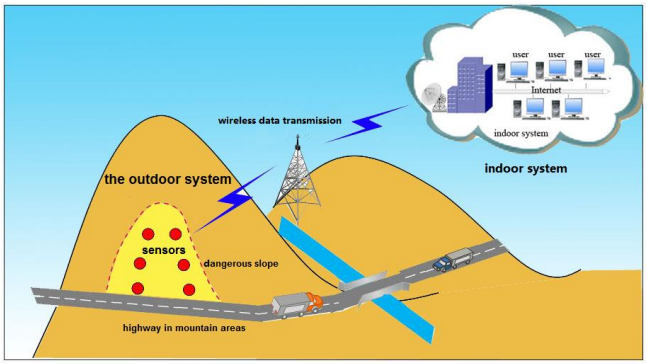

Fig. 3 - Operating principle diagram of the system

Sensor, data acquisition and transmission system

According to the project demand, the slope surface displacement, internal displacement, water pressure, rainfall is monitored. GPS, fixed inclinometer, pore water pressure gauge and SRY-2 high precision digital rain gauge was used for monitoring (Figure 4). In order to realize long-distance wireless transmission of data, a matching signal acquisition and transmission device is also set up (Figure 5). At the same time, in order to ensure the continuous operation of the system in the field, the system adopts solar power supply and is equipped with lightning protection device (Figure 6). The accurate information of the instrument is shown in Table 2 below.

Fig. 4 – Sensors

Fig. 5 - Signal transceiver device

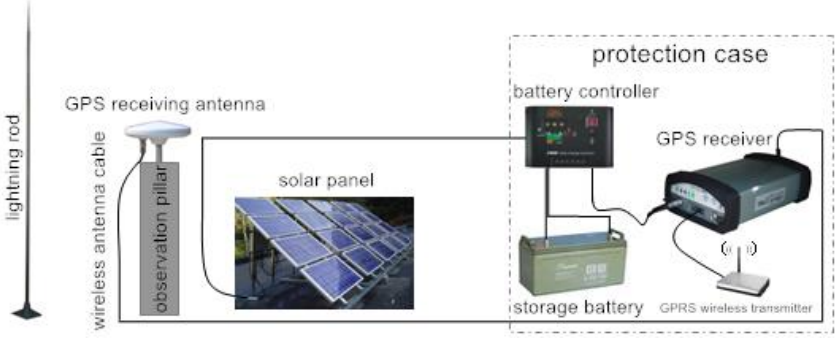

Fig. 6 - Schematic diagram of solar power supply

Tab. 2 - Engineering instrument characteristics

Instrument	Basic functionality	Accuracy of instrument	Methods Instrument Use
GPS	Monitor, query, and warn surrounding soil displacement	0.9m~2m	Traditional hand-held instruments or stand signal amplifiers
fixed inclinometer	It is used for long-term automatic measurement of horizontal displacement and dip Angle of deep foundation pit slope buildings, Bridges and ships	The measurement error of the top Angle is less than or equal to 1°, and the measurement error of the azimuth Angle is less than or equal to 2°	An instrument is drilled into the inner structure of the building to measure the inner tilt of the building structure
pore water pressure gauge	Measuring the pore water pressure inside the building can synchronously measure the temperature of the burial point	⩽0.08%FS	The drilling method is buried inside hydraulic buildings and other structures
SRY-2 high precision digital rain gauge	Used to measure temperature, humidity and temperature change within a fixed range	⩽±2%	Manual placement in advance, set up in a fixed position, regular inspection

Data receiving and analysis system

Data receiving and analysis system includes navigation chart, monitoring analysis, record display, user management, parameter setting and other modules.

It can realize the functions of monitoring point positioning, setting monitoring parameters, setting monitoring frequency, encryption management, data export, automatic mapping and GIS visualization analysis, etc. In order to realize the visual analysis function of GIS, it is necessary to make use of the GIS "Add XY Data" tool to count the 3D coordinate data of the monitoring points. Then, based on these data, stereo distribution graphs of monitoring points are automatically generated. Due to the sparse distribution of monitoring points, the existing 3D coordinates are relatively discrete, and the 3D effect of the slope cannot be realized, so its visualization effect is poor. Therefore, the method of spatial interpolation is adopted to compensate. By superposition analysis of spatial interpolation coordinate data and 3D coordinate data of monitoring points, a visual graph can be generated which is in line with the actual situation.

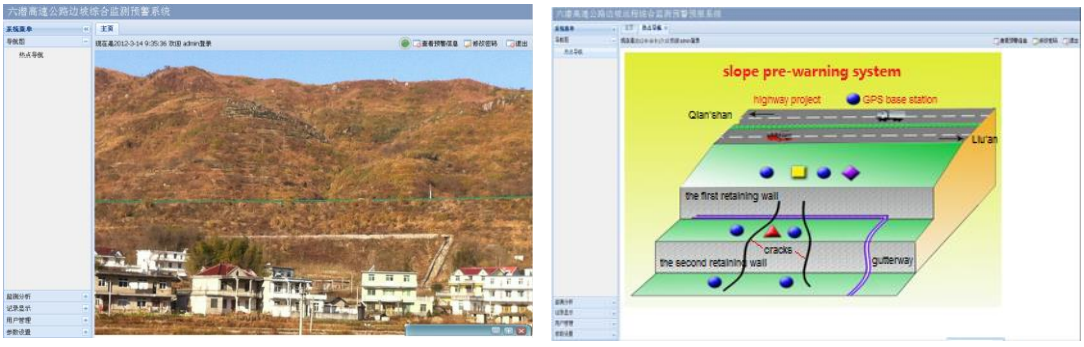

Fig. 7 – System operation interface

Fig. 8 - 3D visualization design sketch

Hierarchical pre-warning system

According to the monitoring precision and principle of slope surface displacement, GNSS instruments buried in the soil and measuring tubing in inclinometers, the four-level pre-warning mode is established. The slope is classified as red, orange, yellow and blue according to the danger degree, corresponding to states of landslide pre-warning, imminent landslide pre-warning, relatively stable pre-warning, stable pre-warning. The specific level and warning division are shown in Table 2.

Tab. 3 - Pre-warning grade and standard of displacement monitoring

Pre-warning level	States forecast	Rule 1： cumulative displacement(Z/(mm/m))	Rule 2： displacement increment(ΔH/mm)		
blue	stable	0~35	20-30 becomes yellowing	30-80 becomes orange	>80 becomes red
yellow	relatively stable	35~55			
orange	imminent landslide	55~85			
red	landslide	＞85			

PROJECT CASE

The system has been applied in the slope monitoring highway project from Liu'an to Qian'shan. Remote real-time monitoring is carried out on the right-side slope of K125+550~K125+725. The maximum height of the slope is 35m, and the water network is developed. From top to bottom, the slope is filled with artificial soil, quaternary sandy soil, sub-clay and strongly weathered granite. The layout of monitoring areas and points is shown in Figure 9 and Figure 10.

Fig. 9 – Monitoring area

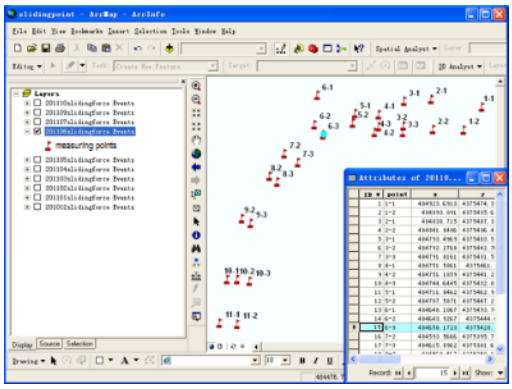

Fig. 10 - Layout of measuring points

The coverage area of the monitoring points is limited. Although the data of the surrounding areas can be obtained through spatial interpolation, with the increase of the distance, the accuracy of the data is reduced and the reference value is basically lost. Therefore, in this project, the effective influence area of comprehensive monitoring was determined and superimposed with the spatial interpolation analysis results of monitoring parameters (Figure 11). In the figure, the curve represents the contours of sliding force, and the colour represents the variation of sliding force (unit: kN).

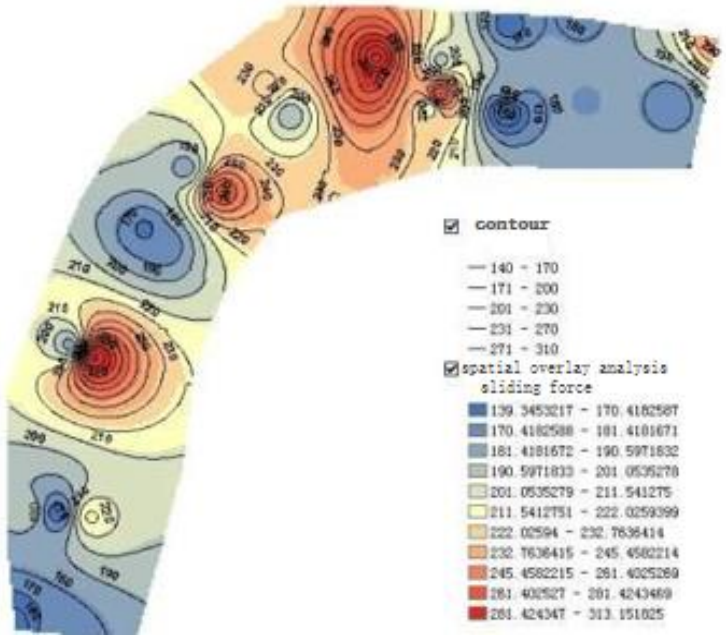

(a)

Fig. 11 - Monitoring data stack and analysis diagram

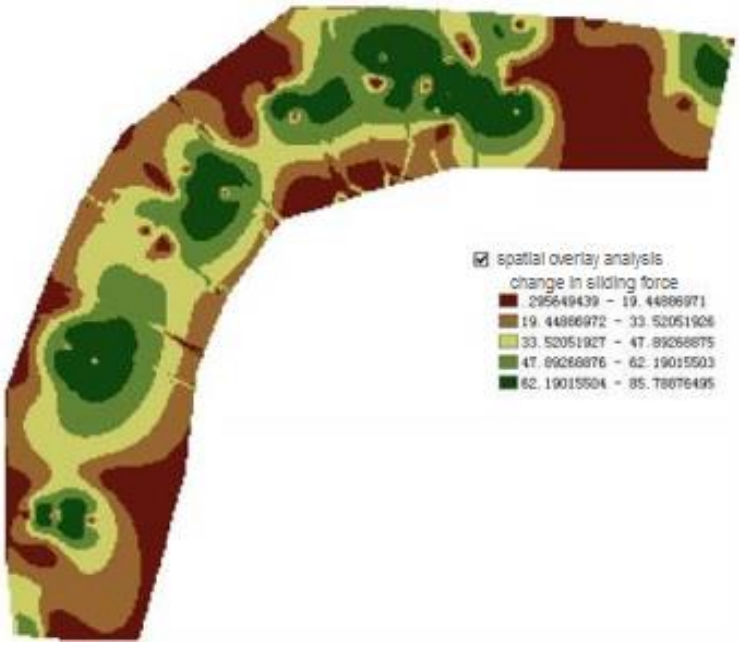

5

(b)

Fig. 11 - Monitoring data stack and analysis diagram

The final monitoring results are shown in Figure 12.

In this slope detection project from Lu'an to Qianshan, after real-time three-dimensional visual monitoring of slope stability of this project, the detection results are very intuitive, the slope deformation has been effectively controlled, and the safety performance has been greatly improved, so that the whole project is in a stable state.

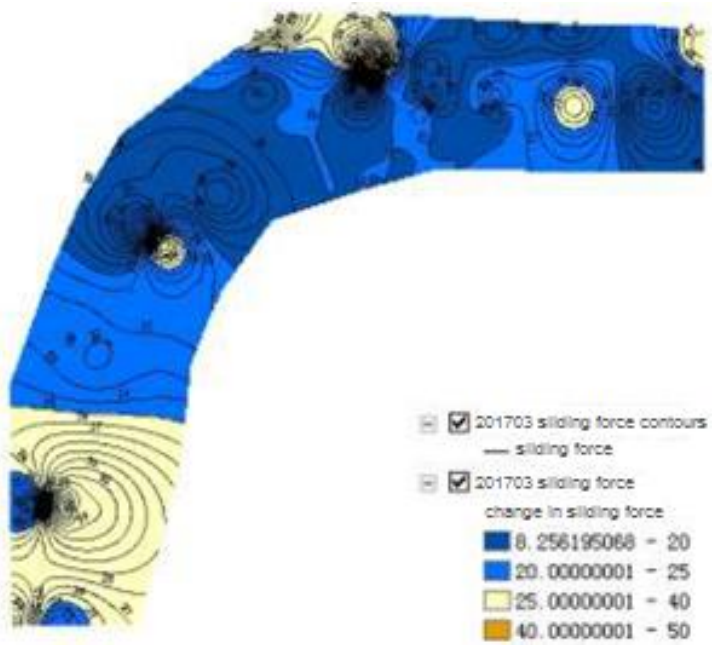

(a) 2017.3

Fig. 11 - Monitoring data stack and analysis diagram

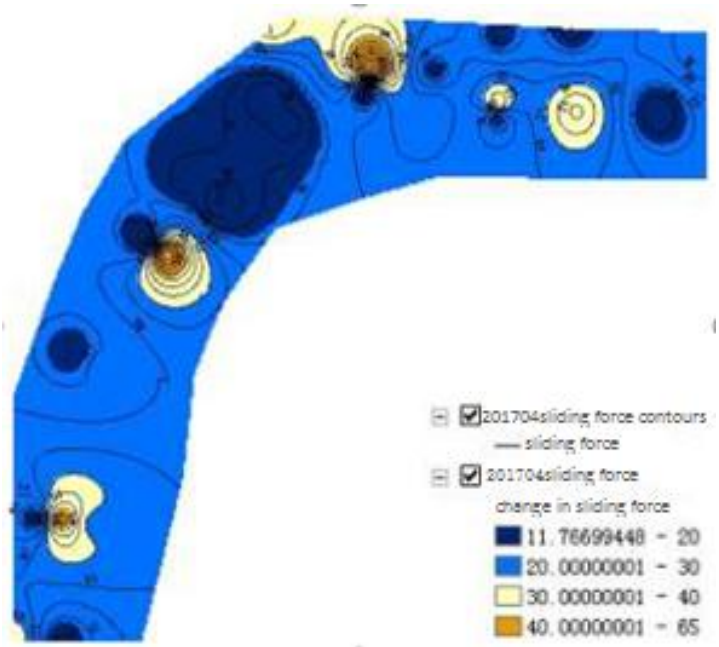

(b) 2017.4

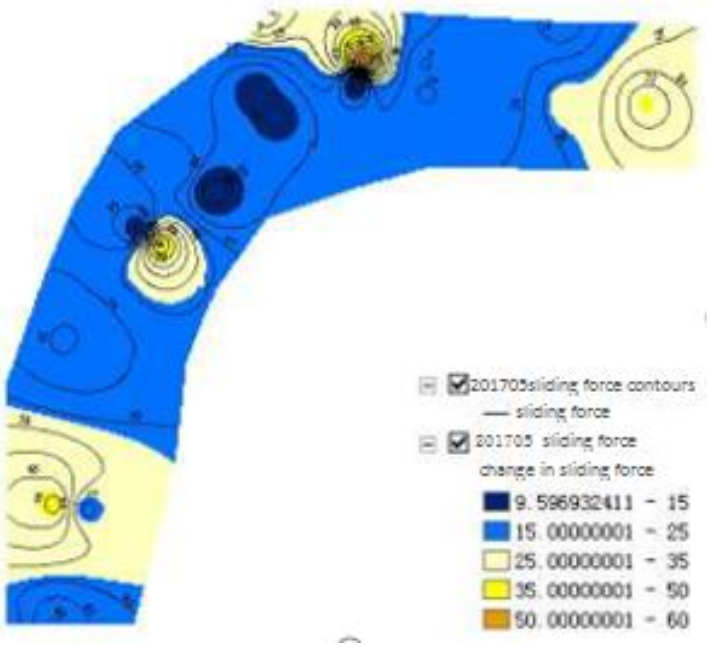

(c) 2017.5

Fig. 12 - Results of monitoring

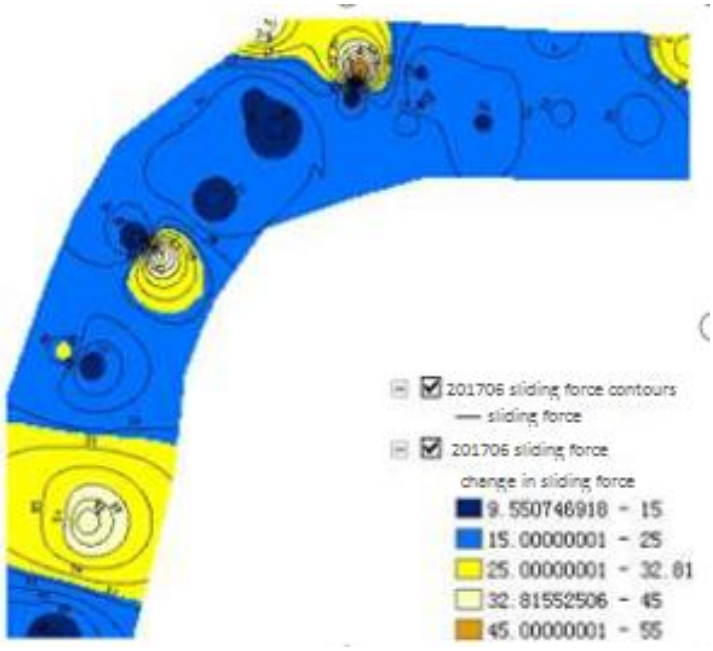

(d) 2017.6

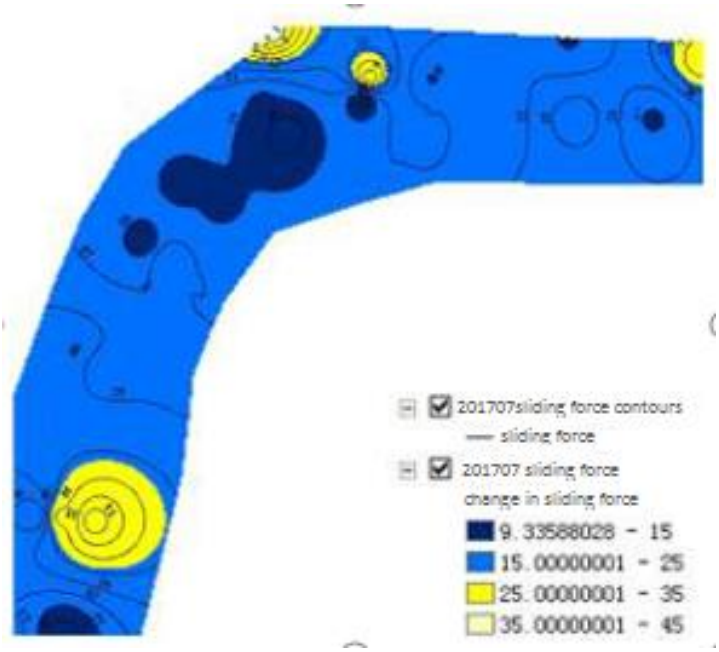

(e) 2017.7

Fig. 12 - Results of monitoring

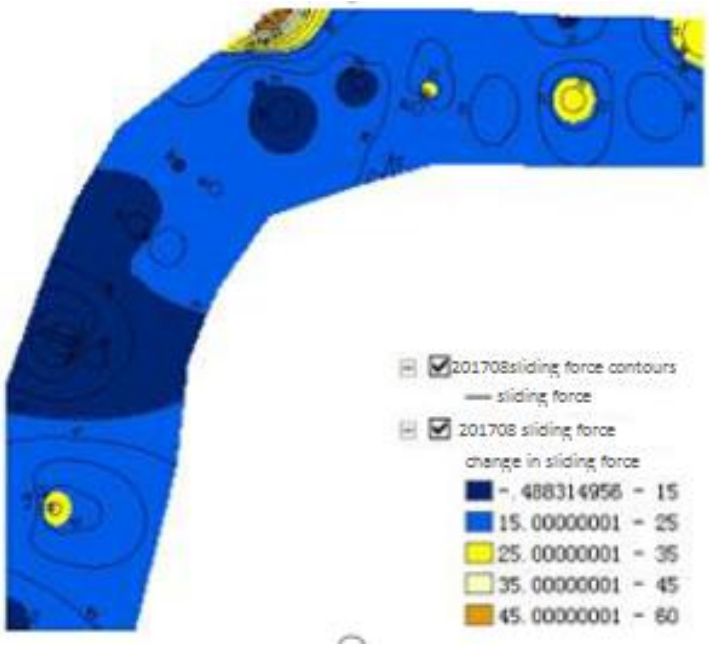

(f) 2017.8

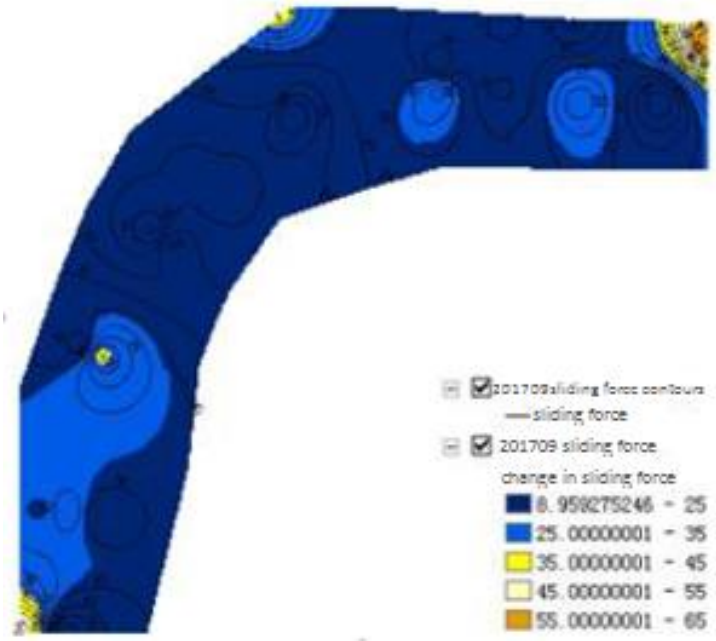

(g) 2017.9

Fig. 12 - Results of monitoring

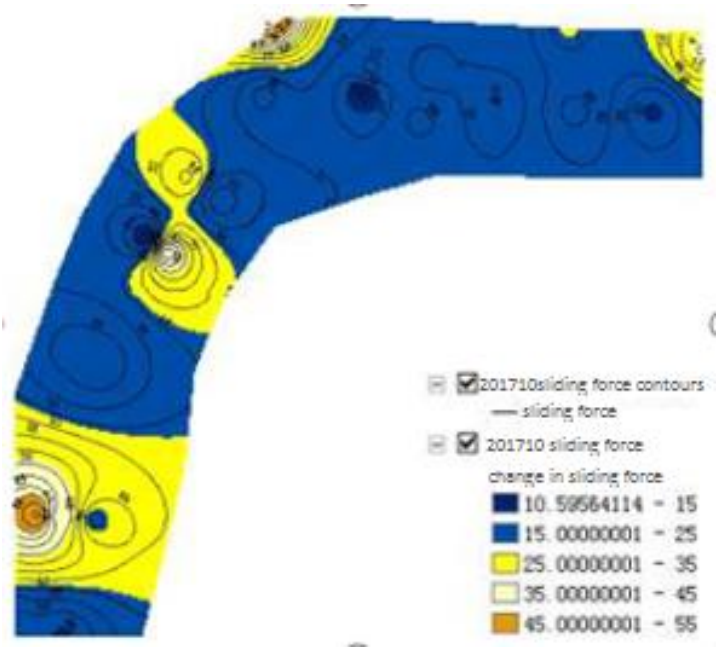

(h) 2017.10

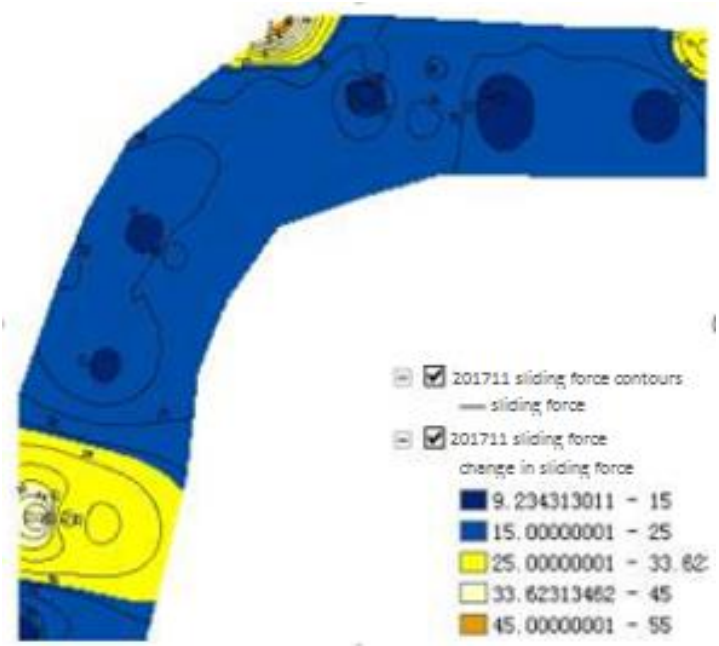

(i) 2017.11

Fig. 12 - Results of monitoring

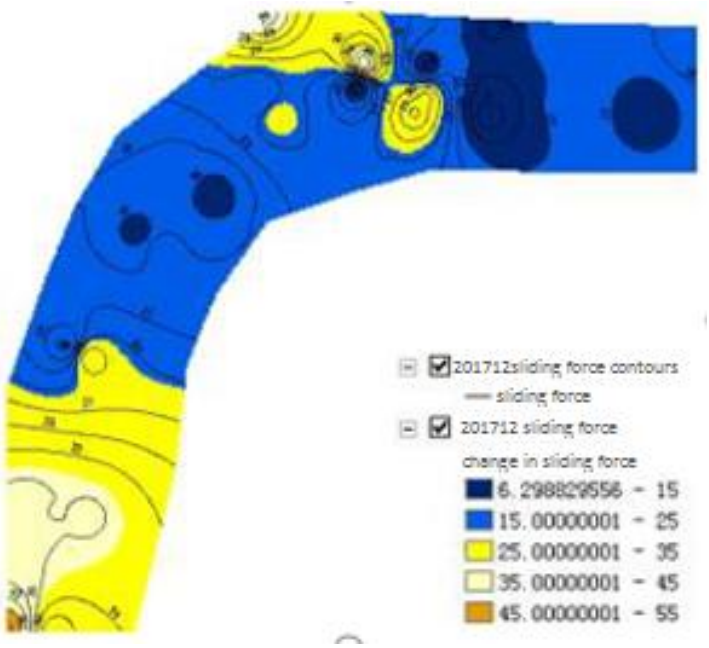

(j) 2017.12

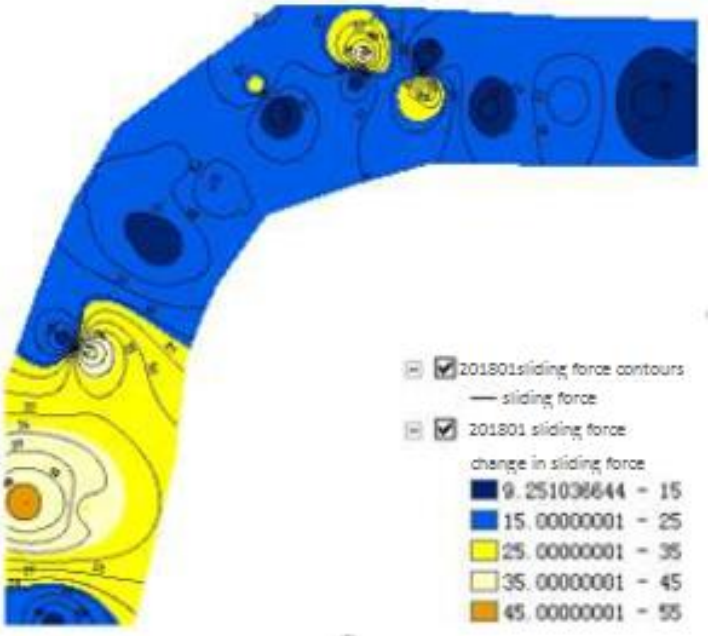

(k) 2018.1

Fig. 12 - Results of monitoring

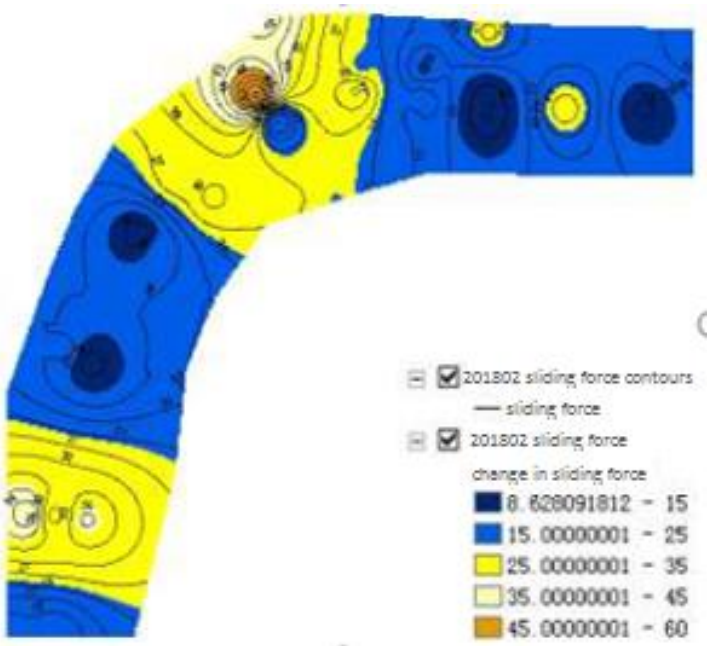

(l) 2018.2

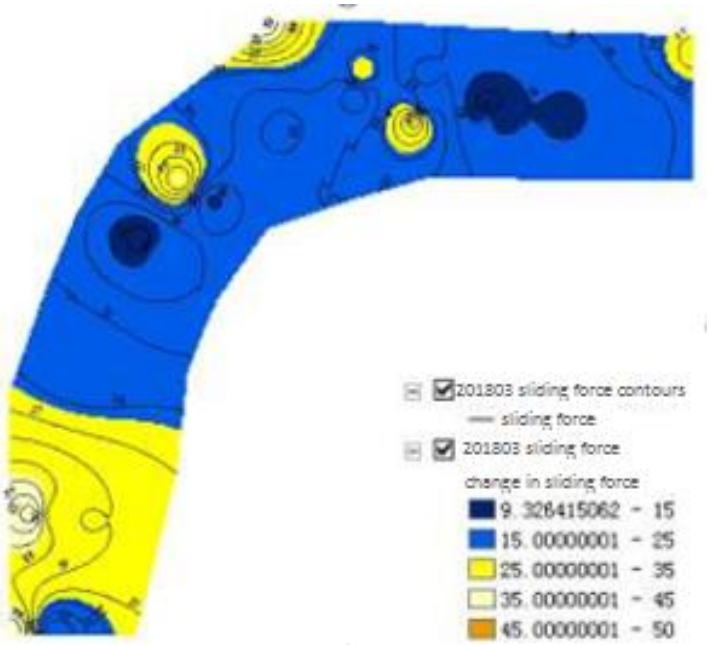

(m) 2018.3

Fig. 12 - Results of monitoring

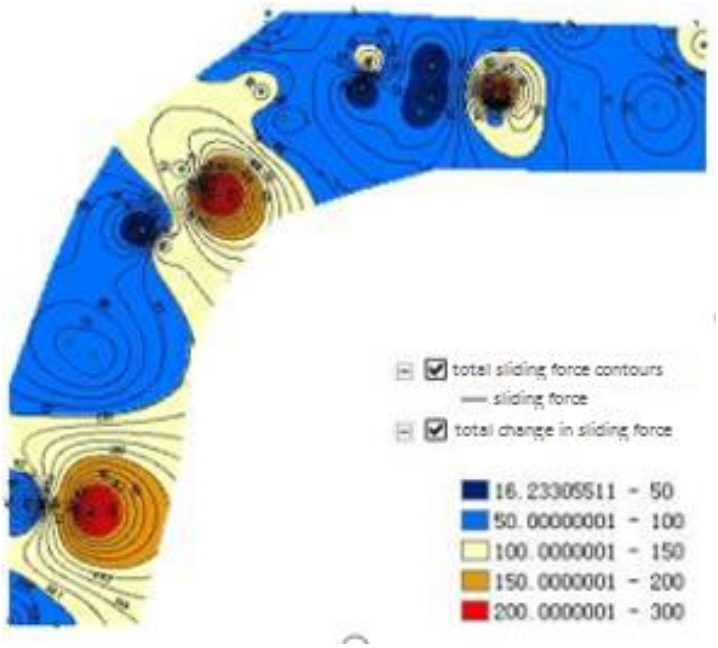

(n) cumulative displacement

Fig. 12 - Results of monitoring

Through the 3D visualization of slope stability research and analysis, the main conclusions can be drawn as follows:

(a) GIS 3D visualization analysis results confirm that the road slope remote intelligent monitoring system based on ArcGIS technology can carry out effective 3D visualization monitoring of the slope.

(b) After the implementation of monitoring, the deformation increment of the slope is not more than 5mm each month, and the slope is in a stable state.

(c) The 3D visualization of slope stability research and analysis can judge the stability of the slope by color, which is very intuitive. At the present stage, the slope of the project is basically blue, and a small part of it is yellow, which indicates that the current slope is stable and can guarantee the safe operation.

CONCLUSION

(a) The force in the rock mass of highway slope is complex, which is affected by many factors such as water content, reinforcement angle, inhomogeneous boundary conditions, etc. So it is necessary to modify the mechanics formula under ideal conditions to reflect the real stress state of slope sliding surface, so as to achieve accurate pre-warning.

(b) In this paper, the pre-warning level and standard of highway slope instability are put forward, and the evaluation method of quantitative pre-warning grade is taken displacement increment and cumulative displacement as indexes.

(c) The application and popularization of the system in the highway project from Lu'an to Qian'shan proves that the improved Sarma algorithm is suitable for engineering practice. GIS 3D visualization analysis technology can make slope monitoring results more intuitive and effective. Once landslide signs occur, the displacement and risk level of the monitoring point can be intuitively determined. Compared with the conventional methods, it is more convenient to help the managers

to make decisions in time, and provides an effective means for the pre-warning and monitoring of highway slope landslide disaster, with remarkable economic and social benefits.

ACKNOWLEDGEMENTS

Finally, I would like to thank the Highway Administration for providing the test section. At the same time, I would like to thank my company for the funds and technical support, and my wife for her understanding and encouragement. Their company makes my life colourful, their encouragement teaches me to persevere, and their help gives me warmth and affection.

REFERENCES

[1] Editorial office of Disaster Reduction In China. National Disaster Record(2005.9)[J]. China Journal of Disaster Reduction, 2005(10): 64.

[2] He MZ. Real-time Remote Monitoring and Forecasting System for Geological Disasters of Landslides and Its Engineering Application[J]. Chinese Journal of Rock Mechanics and Engineering, 2009, (6): 1082.

[3] Abdoun. T, L. Daniseh, D. Ha. Advaneed Sensing for Real-time Monitoring of Geotechnical Systems[J]. Site Characteirzation and Modeling(GSP138), 2005, (4): 164-173.

[4] Kang DL, Yu JS, Zhang HX. New Technology for Landslide Monitoring in Europe[J]. Hubei Geology & Mineral Resources, 2002, 16(4): 78-79.

[5] Ao DC, et al. Auto-monitoring System of Expressway Slope Based on Sensor and Wireless Modes[J]. Journal of Highway and Transportation Research and Development, 2015, 32(11): 41-47.

[6] Yin JH, Ding XL, Yang YW. Application of Remote Slope Monitoring and Prediction System by Globle Positioning System and Conventional Instruments[J]. Journal of Disaster Prevention and Mitigation Engineering, 2003, 23(2): 14-20.

[7] Wang Li,et al. The Application Study of GPS Multi-antenna Monitoring Techniquein the Monitoring of Road Slope Disaster[J]. Journal of Highway and Transportation Research and Development, 2005, 22(6): 163-166.

[8] Yin JH,et al.An integrated sys-tem for slope monitoring and warning in Hong Kong[C].ProcAdvances in Building Technology.Hong Kong,Inc,2002:1661-1670.

[9] Ding Chen. Research on The Coast Long-Range Monitoring System of The Gross Demonstration System for Monitoring and Forecasting The Geologic Disaster[D]. Tsinghua University, 2004. 6.

[10] Sarma SK. 1979,Stability Analysis of Embankments and Slopes[J]. Journal of the Geotechnical Engineering Division, 105(12): 1511-1524.

[11] Yang JM, Yang SX. Effective Stress Forom for Slope Stabolity Analysis Based on Sarma Method[C]. Proceedings of the 2020 Academic Exchange Conference on Industrial Architecture(The Second Volume), 2020: 476-481.

[12] Zhao Jingyao. Examining Land-Use Change Trends in Yucheng District, Ya'an City, China, Using ANN-CA Modeling. Journal of Urban Planning and Development. 2023.1.

CIVIL ENGINEERING JOURNAL

Article no. 3

THE CIVIL ENGINEERING JOURNAL 1-2023

DETERMINATION OF DESIGN PARAMETERS OF ASPHALT PAVEMENT BASED ON PG TECHNOLOGY

Haitao Zhang, Meiyi Gao, Shengsheng Ma and Huizhong Xiong,

School of Civil Engineering, Northeast Forestry University, Harbin 150040, China; xionghuizhong@126.com

ABSTRACT

The design parameters are one of the important factors to ensure the quality of asphalt pavement design. In “Highway Asphalt Pavement Design Specification” (JTGD50-2017), the stander of China, used the asphalt mixture anti-pressure resilience modulus at a single temperature of 20 ℃ as the design metrics. However, asphalt mixture, as a sticky-bullet plastic material, shows different mechanical properties at different temperatures. China is a vast territory, and there are great differences between the high and low temperature value (m and n) of each region. Therefore, it is unreasonable to design asphalt pavement only with the asphalt mixture anti-pressure resilience modulus value at 20 ℃. Studies show that the design parameters using PG technology can improve the high temperature anti-rutting and low temperature cracking performance of asphalt pavement.

KEYWORDS

Road engineering, Asphalt mixture, Design parameters, Resilience modulus, PG technology

INTRODUCTION

Some modern asphalt pavement designs (for example, in China) use the asphalt mixture's anti-pressure resilience modulus (20°C) as a criterion. The anti-pressure resilience modulus is one of the most important parameters for the mechanical properties of pavements [1-2]. A reasonable pavement thickness can be calculated from the anti-pressure resilience modulus [3]. The index of anti-pressure resilience modulus can also be used to evaluate the long-term service performance of asphalt pavements in terms of fatigue life [4], permanent deformation [5] and thermal cracking [6]. The anti-pressure rebound modulus of asphalt mixtures is therefore widely used as a parameter in the design of pavements. For example, Elliott R P et al. in the 1986 AASHTO Guide to Structural Design of Pavements stated that modulus of elasticity was one of the basic and reasonable indicators to be included in pavement design [7] Maher A et al. also used parameters such as dynamic modulus, elastic modulus and Poisson's ratio for flexible pavement design [8]; The effect of different factors on pavement performance was investigated by Su N et al. The study showed that the modulus of elasticity, load and temperature have a large effect on the variation in the performance of asphalt pavements. [9] According to Hossain Z et al., the modulus of elasticity is an important design element in the pavement design process. [10] The design parameters at a single temperature, on the other hand, are not reflective of the mechanical characteristics of the asphalt mixture at varied temperatures. This is due to the fact that both asphalt and asphalt mixtures have viscoelastic material qualities. [11-12] The material's mechanical characteristics change with temperature [13-14], resulting in totally distinct states and moduli at high and low temperatures [15-16]. The pavement performance of asphalt mixtures is clearly influenced by temperature. Therefore, in order to avoid the influence of temperature changes on asphalt pavement design, many countries and regions have started to adopt PG technology for asphalt pavement design. Based on the PG rated climate zones for road asphalt pavements, the high and low temperature design parameter

values for each region are selected for road design. For example: Salem H A et al. found that the PG method was more reasonable for the design of Libyan desert roads and classified Libyan desert roads as PG70-10, PG76-10 and PG82-10. [17] Tan Y et al. used digital image correlation (DIC) analysis to obtain design parameters capable of characterizing the low-temperature performance of asphalt mixtures in cold regions, based on the theory of PG techniques. And they found that the low temperature performance of asphalt mixes was better when designed using this method. [18] Copeland A et al. also used PG technology to design the Florida Highly Recycled Asphalt Pavement - Warm Mix Asphalt project.[19] It can therefore be seen that the use of PG technology for asphalt pavement design allows for a range of high and low temperature variations in asphalt pavement design compared to the use of indicators such as anti-pressure resilience modulus at a single temperature for asphalt pavement design. This avoids the impact of temperature changes on the design of the pavement.

This study is an exploratory study of the design method for asphalt pavements with PG technology in the USA, based on the standard design method for road asphalt pavement design with parameters such as anti-pressure rebound modulus. On the basis of the climatic zones of China and the PG classification of asphalt pavements, asphalt pavement design parameters corresponding to the high and low temperature values (m and n) for each climatic zone were established. Refinement of asphalt pavement design parameters determined by a single temperature of 20°C in China. Design parameters using PG technology can improve the high temperature rutting resistance and low temperature cracking resistance of asphalt pavements.

ASPHALT MIXING MATERIAL COMPOSITION DESIGN

Asphalt

The experiment selected four kinds (70# base asphalt, SBS modified asphalt (70#), 90# base asphalt, SBS modified asphalt (90#)) asphalt as the binding material, asphalt technical indicators as shown in Table 1.

Tab. 1 - Indexes of asphalt

Asphalt	Penetration (25℃)/ 0.1mm	Penetration index (PI)	Ductility		Softening point/℃	Viscosity (135℃)/Pa.s
			5℃	15℃		
70# base asphalt	66	-1.3	8.7	132	46.5	0.403
SBS modified asphalt (70#)	48	1.0	30.5	126.5	78.9	2.226
90# base asphalt	93	-0.77	9	165	44.5	0.328
SBS modified asphalt (90#)	68	-0.29	35	86	72.8	1.895

Aggregate

Three common aggregate gradations of AC-13, AC-16 and AC-20 were selected for the test. The detailed aggregate gradation parameters are shown in Table 2.

Tab. 2 - Gradations of aggregates

Mixture type	Percentage of mass passing through sieve hole (mm) / (%)											
	26.5	19	16	13.2	9.5	4.75	2.36	1.18	0.6	0.3	0.15	0.075
AC-13			100	97.5	75	50	35	27	20	14	8.5	6
AC-16		100	95	85	75	50	40	25	18	13	12.5	9.5
AC-20	100	95	82.5	71	62	48	37	27	20	15	10	6

Asphalt mixture design

The optimal asphalt content of different asphalt mixtures is obtained through the Mashall mix ratio design (Table 3). The static pressure method and the compaction method were used to form the test specimens (100 mm in diameter and 160 mm in height), and two ends of the two test specimens were cut by 30 mm to form a standard test specimen. Then the compressive resilience modulus of the two test pieces was tested in the temperature range of -30 ℃ - 60 ℃.

Tab. 3 - Optimum asphalt content

Type of asphalt	Asphalt mixture gradation		
	AC-13	AC-16	AC-20
70# base/ modified asphalt	5.30	4.40	4.10
90# base/ modified asphalt	5.60	4.70	4.40

RELATIONSHIP BETWEEN DYNAMIC MODULUS AND STATIC MODULUS OF ASPHALT MIXTURE

The "Testing Rules for Asphalt and Asphalt Mixtures of Highway Engineering" (JTG E20-2011) stipulates that the specimens used in the single-axis compression anti-pressure resilience molding of asphalt mixtures shall be formed by static pressure method or by using a core drill from the molding plate. The "Specifications for Design of Highway Asphalt Pavements" (JTG D50-2017) stipulates that test specimens formed by impact compaction, static compaction, vibration compaction and other methods can be used to perform dynamic compression resilience modulus tests of asphalt mixtures.

Relationship between static compressive resilience modulus of asphalt mixture and temperature

The test results are shown in Figure 1. The regression relationship and suggested values at different temperatures were obtained by fitting the curve of the relationship between the static modulus and the temperature (Table 4).

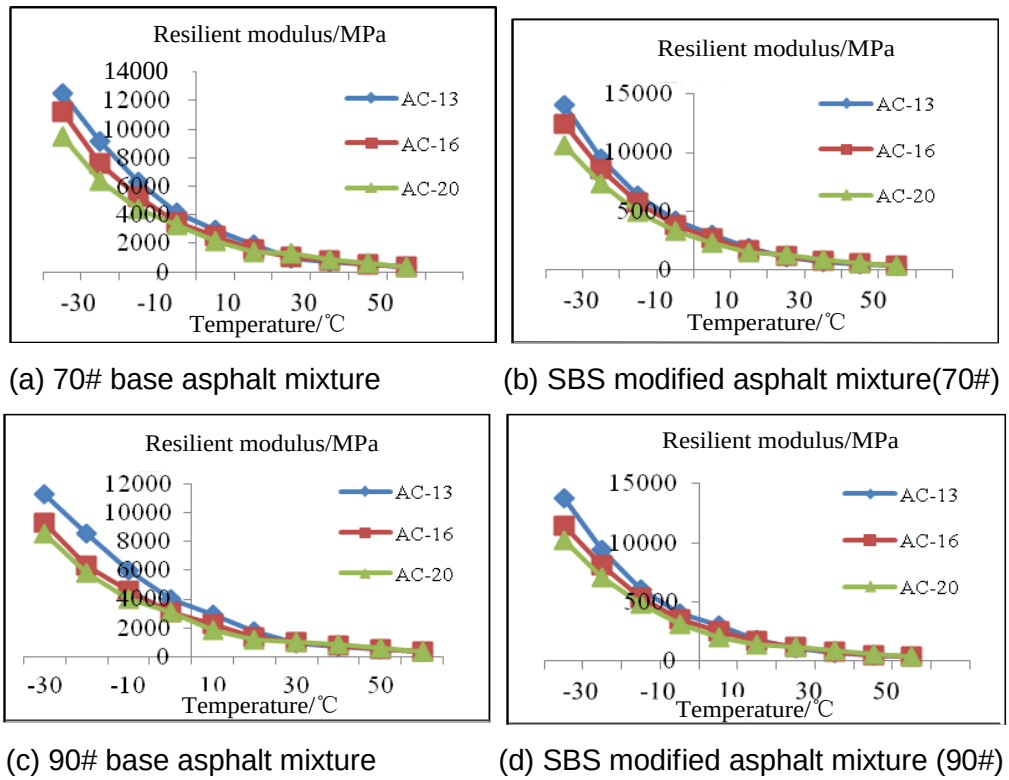

(a) 70# base asphalt mixture (b) SBS modified asphalt mixture(70#)

(c) 90# base asphalt mixture (d) SBS modified asphalt mixture (90#)

Fig. 1 - Curve of static compression modulus and temperature of asphalt mixture

Tab. 4 - Static Resilience Modulus Suggested Values

Type of mixture		Regression relation	Suggested static modulus at different temperatures (℃)/ Mpa					
			-30	-10	0	20	40	60
70# base asphalt	AC-13	y = 3999.5e-0.041x R² = 0.9948	13678.3	6039.2	3999.5	1759.8	759.9	360.1
	AC-16	y = 3550.2e-0.038x R² = 0.9987	11101	5191	3550.2	1660	777	363.1
	AC-20	y = 3215.9e-0.035x R²=0.9938	9189.9	4563.6	3215.9	1597.1	793	393.8
SBS modified asphalt (70#)	AC-13	y = 4218.7e-0.041x R² = 0.9977	14433.1	6356.8	4218.7	1858	818.3	360.4
	AC-16	y = 3890.8e-0.039x R² = 0.9998	12563	5747	3890.8	1784	818	374.8
	AC-20	y = 3506.1e-0.035x R² = 0.9965	10019.2	4975.4	3506.1	1741.1	864.6	429.3
90# base asphalt	AC-13	y = 3792.9e-0.04x R² = 0.9938	12592.9	5658.3	3792.9	1704.3	765.8	344.1
	AC-16	y = 3161e-0.036x R² = 0.9959	9308.1	4530.8	3161	1538.6	748.9	364.5

SBS modified asphalt (90#)	AC-20	y = 2897.9e-0.034x R² = 0.9899	8036.4	4071.4	2897.9	1468.1	743.8	376.8
	AC-13	y = 4104.7e-0.041x R² = 0.9976	14043.1	6185	4104.7	1807.8	796.2	350.7
	AC-16	y = 3661.7e-0.038x R² = 0.9996	11449.3	5354.4	3661.7	1712.5	800.9	374.5
	AC-20	y = 3295.7e-0.035x R² = 0.9938	9418.1	4676.8	3295.7	1636.6	812.7	403.6

Establishment of the relationship between dynamic modulus and static modulus of asphalt mixture

Studies have shown that the dynamic modulus of asphalt mixtures is approximately two to three times the static modulus. The resilience modulus value of asphalt mixture is greatly affected by temperature and loading frequency. Under different temperatures and loading frequencies it will be several times different. There is usually a large multiple relationship between the dynamic and static modulus at low temperature and high frequency, but the difference is not large at room temperature and low frequency; and a slightly larger at the general temperature and frequency compared with room temperature and low frequency. Different loading frequencies represent vehicles of different speeds on the road. The speed range specified by the “Technical Standards for Highway Engineering” of China is 30-120 Km/ h. China's current stander "Code for Design of Highway Asphalt Pavements" (JTG D50-2017) stipulates that the loading frequency of the asphalt surface layer modulus is 10Hz (translates to a driving speed of approximately 67Km/ h), which can truly reflect the most actual speed of road vehicles in China.

Through experiments, this study found that the main factors affecting the resilience modulus of asphalt mixtures are temperature and frequency, while the gradation, the amount of asphalt, and the type of asphalt have little effect. And there are different multiples gap between the dynamic modulus and the static modulus of the asphalt mixture at different temperatures and loading frequencies. Therefore, this study mainly considers the two influencing factors of temperature and frequency. Based on the "Code for Design of Highway Asphalt Pavements" (JTG D50-2017), the relationship between the dynamic and static modulus of asphalt mixtures at 10 Hz and different temperatures is established. It can be found in Figure 1 that the decrease rate of the resilience mode value is larger at -30-0 ℃. In this temperature interval, the resilience mode value of 70# asphalt mixes with three grades decreased by an average of 7266.67Mpa. The resilience mode value of SBS modified asphalt decreased by 9666.81Mpa on average. The resilience mode value of 90# matrix asphalt mix decreased by 6783.33Mpa on average, The resilience mode value of SBS modified asphalt mix (90#) decreased by 9133.46Mpa on average. But the rate is reduced at 0-30 ℃, and the change of the modulus value slows down at 30-60 ℃.Compared with 0°C, the resilience mode value of the four asphalt mixes with different grades at 30°C decreased by 2373.41 MPa, 1675.21 MPa, 2276.69 MPa, and 1800.04 MPa on average, respectively. The average variation of the resilience mode value is lower in the 30-60 °C range. The slope change curve is shown in Figure 2.

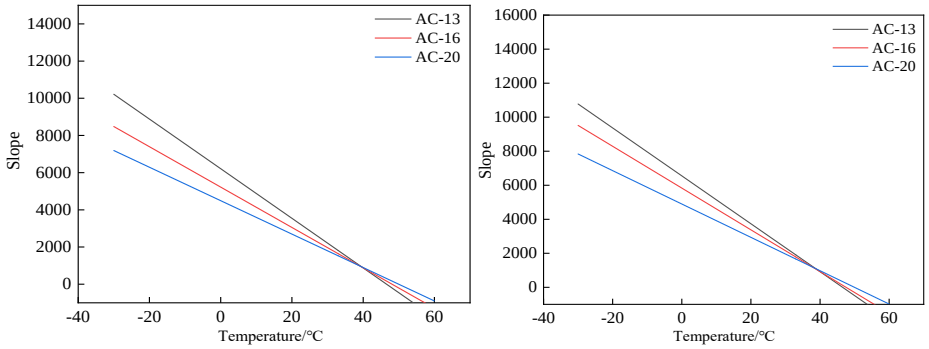

(a) 70# base asphalt mixture (b) SBS modified asphalt mixture(70#)

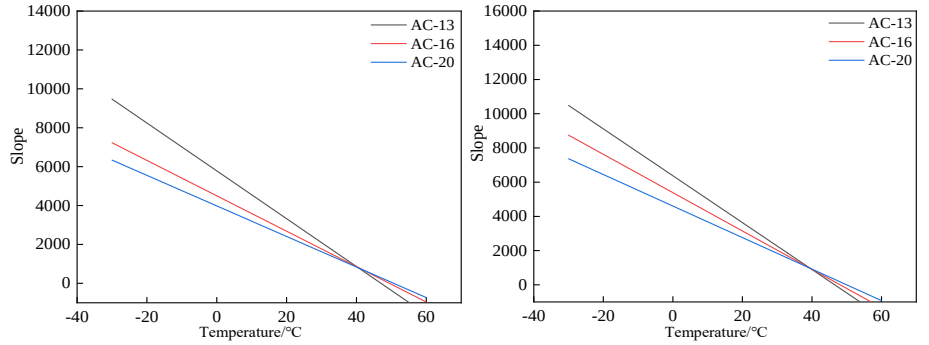

(c) 90# base asphalt mixture (d) SBS modified asphalt mixture (90#)

Fig.2 - Slope change curves at different temperatures

Therefore, this study divided the range of -30-60 ℃ into three temperature ranges of -30-0 ℃, 0-30 ℃, and 30-60 ℃. And the three temperatures of -20 ℃, 20 ℃ and 40 ℃ were taken as the representative to obtain the multiple relationships between the dynamic and static modulus. Because the impact of gradation and asphalt type on the resilience modulus value of asphalt mixtures was not obvious, the average values of the static modulus of different grades and asphalt types at -20 ℃, 20 ℃, and 40 ℃ were used as modulus value at this temperature, respectively (Table 5).

Tab. 5 - Test results of resilient modulus of asphalt mixture

Test temperature /℃	Static modulus of Asphalt mixture (MPa)				Average value (Mpa)
	70# base asphalt	Modified asphalt (70#)	90# base asphalt	Modified asphalt (90#)	
-20	8044.1	8463.5	6919.9	8183.1	7902.7
20	1607.3	1739.8	1423.2	1650.9	1605.3
40	799.5	820.3	776.4	804.4	800.2

Relevant research shows that the dynamic modulus of the asphalt mixture obtained at 10 Hz loading frequency and 20 ℃ is 16507 Mpa[20], which is 10.3 times the static modulus value of this research. The average resilience modulus of different grades obtained at 40 ℃ is 5637.3 MPa, which is 7.1 times the static modulus value of this study. The dynamic modulus of the asphalt mixture obtained at the loading frequency of 10Hz at 21.1 and 39.2 ℃ is 7164.7 and 2508.3 MPa, which are

4.5 and 3.2 times the static modulus values of this study, respectively. The dynamic moduli obtained at -20 ℃ and 20 ℃ are 31308.5 and 5622.7MPa, which are 3.97 and 3.5 times the static modulus of the same temperature in this study, respectively.

The suggested static modulus of the original code “Design Code for Highway Asphalt Pavement JTG D50-2006” at 20 ℃ is between 800-1600MPa, while the new specification “Code for Design of Highway Asphalt Pavement Design JTG D50-2017” is shown as Table 6.

Tab. 6 - Range of dynamic compression resilient modulus of asphalt mixture at 20 ℃ (MPa)

Mixture Gradation	Asphalt type			
	70# base asphalt	90# base asphalt	110# base asphalt	SBS modified asphalt
AC10、AC13	8000~12000	7500~11500	7000~10500	8500~12500
AC16 、 AC20 、 AC25	9000~13500	8500~13000	7500~12000	9000~13500

It can be seen from Tables 5 and 7 that the dynamic compression resilience modulus is 5 to 10 times the static modulus, and the suggested value for the dynamic compression resilience modulus is 5-8 times. In this study, the top surface method was be used to test the spring deformation of the specimen at all heights, so the obtained resilience modulus value will be small. In order to obtain a more accurate relationship between dynamic and static modulus, combined with domestic and foreign research results, standard recommended values, measured data of this study, etc., it is concluded that that there is 4 times, 5 times, 7 times of the relationship between asphalt mixture dynamics and static modulus in the three temperature ranges (-30-0 ℃, 0-30 ℃ and 40-60 ℃), respectively.

Conversion of static-dynamic anti-pressure resilience modulus of asphalt mixture

The static modulus of asphalt mixture is converted to dynamic modulus according to the resulting multiple relationship in different temperature intervals. The conversion results are shown in Table 7.

Tab. 7 - Dynamic compression resilient modulus of asphalt mixture (MPa)

Type	Gradation	Test temperature/ ℃									
		-30	-20	-10	0	10	20	30	40	50	60
70# base asphalt	AC-13	50038	36442	25094	20589	14945	9408	4963	4865	3678	2679
	AC-16	44823	30462	21203	17230	12675	7765	5349	5303	3827	2561
	AC-20	38142	25624	17484	16449	10890	6935	6367	5985	4348	2556
SBS modified asphalt (70#)	AC-13	56068	37909	25543	21330	15370	9607	5747	5229	3816	2768
	AC-16	49870	34320	22965	19141	13468	8780	5940	5772	3950	2687

	AC-20	42323	29332	19964	16905	11484	7560	6621	6224	4414	2801
	AC-13	45158	34200	24004	20081	14521	8752	4822	4574	3616	2650
90# base asphalt	AC-16	37200	25467	20384	15545	11327	6670	4981	4844	3723	2570
	AC-20	34412	23250	16103	15454	9304	5942	5129	4991	4230	2529
	AC-13	55152	37439	24152	20361	15298	9108	5663	5191	2697	2723
SBS modified asphalt (90#)	AC-16	45776	32548	21600	17427	12582	8450	5772	5699	3777	2647
	AC-20	40758	28211	19242	15712	9892	7205	5928	5583	4316	2693

Through the conversion, it can be found that the modulus value of asphalt mixture at 20 ℃ is in the range of 6670-9607 MPa, which is in the dynamic modulus value of the new specification recommends at the loading frequency of 10Hz and 20 ℃. This shows that the conversion relationship between the static module of asphalt mixture and the dynamic modulus is reasonable.

RELATIONSHIP BETWEEN ASPHALT MIXTURE DESIGN PARAMETERS AND TEMPERATURE

Relationship between dynamic resilience modulus and temperature of asphalt mixture

The relationship between the dynamic anti-pressure resilience modulus and the temperature regression of asphalt mixture is shown in Table 8.

Tab. 8 - Regression relationship of dynamic resilient modulus and temperature of asphalt mixtures

Type of asphalt	Gradation	Regression relation	
70# base asphalt	AC-13	y=20250.57-709.15x+7.29x2	R2=0.9916
	AC-16	y=17343.97-617.28x+6.7x2	R2=0.9825
	AC-20	y=15370-496.31x+5.28x2	R2=0.9664
SBS modified asphalt (70#)	AC-13	y=21166.38-783.92x+8.51x2	R2=0.9826
	AC-16	y=19145.83-691.18x+7.53x2	R2=0.9819
	AC-20	y=16766.12-571.83x+6.26x2	R2=0.9780
90# base asphalt	AC-13	y=19238.74-640.48x+6.29x2	R2=0.9943
	AC-16	y=15383.94-507.31x+5.24x2	R2=0.9889
	AC-20	y=13752.91-459.97x+5.03x2	R2=0.9724
SBS modified asphalt (90#)	AC-13	y=20541.46-774.12x+8.43x2	R2=0.9797
	AC-16	y=17926.13-636.18x+6.90x2	R2=0.9842
	AC-20	y=15691.42-560.29x+6.35x2	R2=0.9796

Relationship between splitting strength of asphalt mixture and temperature

The relationship between the asphalt mixture splitting strength and temperature is shown in Figure 2. According to the relationship curve fitting of Figure 3, the regression relationship formula and the suggested values at different temperatures (Table 9) are obtained.

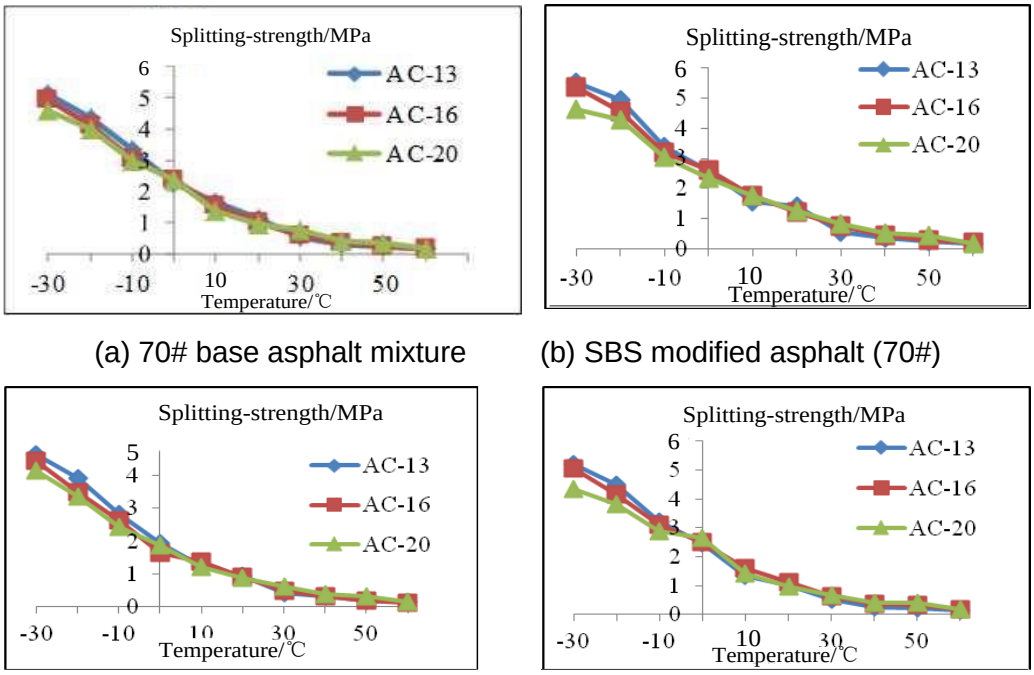

(a) 70# base asphalt mixture (b) SBS modified asphalt (70#)

(c) 90# base asphalt mixture (d) SBS modified asphalt (90#)

Fig. 3 - Curves of splitting tensile strength with temperature of asphalt mixture

Tab. 9 - Recommended values for split tensile strength

Type of mixture		Regression relation		Suggested value of split tensile strength at different temperatures (℃)/ Mpa					
				-30	-10	0	20	40	60
70# asphalt	AC-13	y =2.19-0.11x+0.001x2	R² = 0.9804	6.85	2.96	1.94	0.84	0.36	0.16
	AC-16	y= 2.17-0.10x+0.001x2	R² = 0.9815	6.64	2.92	1.94	0.85	0.38	0.17
	AC-20	y=2.10-0.09x+9.85Ex2	R² = 0.9865	5.82	2.78	1.92	0.92	0.44	0.21
70# SBS	AC-13	y =2.36-0.11x+0.00138x2	R² = 0.9805	7.36	3.18	2.09	0.9	0.39	0.17
	AC-16	y =2.40-0.103x+0.00118x2	R² = 0.9852	6.83	3.19	2.18	1.02	0.48	0.22
	AC-20	y =2.29-0.09x+9.78E-4x2	R² = 0.9889	6.05	3.01	2.12	1.05	0.52	0.26

90# asphalt	AC-13	y = 1.89-0.09x+0.00106x2 R² = 0.9818	5.78	2.55	1.69	0.74	0.33	0.14
	AC-16	y=1.82-0.083x+9.82931E-4x2 R² = 0.983	5.43	2.44	1.63	0.73	0.33	0.15
	AC-20	y=1.81-0.073x+8.14556E-4x2 R² = 0.9870	4.92	2.39	1.67	0.81	0.41	0.19
90# SBS	AC-13	y = 2.19-0.112x+0.00139x2 R² = 0.9778	7.15	2.97	1.91	0.79	0.33	0.14
	AC-16	y = 2.24-0.096x+0.0011x2 R² = 0.9855	6.36	2.98	2.04	0.95	0.45	0.21
	AC-20	y = 2.038-0.083x+9.17521E-4x2 R² = 0.9798	5.53	2.69	1.88	0.91	0.45	0.22

DETERMINATION OF ASPHALT PAVEMENT DESIGN PARAMETERS BASED ON PG TECHNOLOGY (HEILONGJIANG PROVINCE, CHINA)

Based on the asphalt pavement design specification, the dynamic rebound modulus and the relationship between crack strength and temperature of asphalt mixtures, as well as the classification of PGm-n grades of asphalt pavements, were investigated by combining the PGm-n technology while retaining the design parameters of the specification. Based on the results of the previous study, this paper takes asphalt pavement in Heilongjiang Province, China, as an example to verify the validity of the results of the previous study.

Asphalt pavement PGm-n grade climate partition

Through the PGm-n grade analysis of asphalt pavement climate zoning in Heilongjiang Province, the PGm-n grade and the corresponding representative city (Table 10) are obtained. Based on the above research data, the design parameters of asphalt pavement in Heilongjiang province based on PG technology (Table 11 and 12) are obtained.

Tab. 10 - Climate zones and PGm-n of asphalt pavement in Heilongjiang province

Climate zoning	PGm-n grade	Representative city
2-1	PG52-46	Mohe
2-1	PG58-40	Nenjiang
2-1	PG58-34	Mudanjiang
2-2	PG58-34	Harbin

Tab. 11 - Parameter of resilient modulus of asphalt mixture（Heilongjiang province）

Climate zoning	City	PGm-n	Asphalt	Gradation	Static resilience modulus /MPa			Dynamic resilience modulus /MPa		
					m ℃	20 ℃	-n ℃	m ℃	20 ℃	-n ℃
2-1	Mohe	PG52-46	90#	AC-13	474	1704.3	23882.1	3316.6	8521.5	95528.4
				AC-16	486	1538	16558.3	3403.4	7690	66233.2
				AC-20	495	1468.1	13845.9	3462.2	7340.5	55383.6
			90#	AC-13	487	1451.5	27062.1	3407.6	7257.5	108248.2

			modified	AC-16	508	1712.5	21029.5	3553.2	8562.5	84118
				AC-20	534	1636.6	16487.8	3738.7	8183	65951.2
2-2	Harbin	PG58-34	90#	AC-13	373	1704.3	14777.9	2608.9	8521.5	59111.6
				AC-16	392	1538	10749.8	2742.6	7690	42999.2
				AC-20	403	1468.1	9207.2	2823.1	7340.5	36828.8
			90# modified	AC-13	381	1451.5	16545.8	2664.9	7257.5	66183.2
				AC-16	404	1712.5	13328.8	2828.7	8562.5	53315.2
				AC-20	433	1636.6	10833.2	3029.6	8183	43332.8

Tab. 12 - Parameter of split strength of asphalt mixtures（Heilongjiang province）

Climate zoning	City	PGm-n	Asphalt	Gradation	Split tensile strength /MPa		
					m ℃	20 ℃	-n ℃
2-1	Mohe	PG52-46	90#	AC-13	0.2	0.74	11.14
				AC-16	0.2	0.73	10.29
				AC-20	0.26	0.81	8.75
			90# modified	AC-13	0.19	0.79	14.46
				AC-16	0.28	0.95	11.69
				AC-20	0.29	0.91	9.84
2-2	Harbin	PG58-34	90#	AC-13	0.16	0.74	6.82
				AC-16	0.16	0.73	6.38
				AC-20	0.21	0.81	5.68
			90# modified	AC-13	0.15	0.79	8.53
				AC-16	0.22	0.95	7.41
				AC-20	0.23	0.91	6.39

CONCLUSIONS

(1) The resilience modulus and splitting strength of the asphalt mixture decrease with increasing temperature. When the temperature is between -30-0 ℃, these indicators are maintained at a high level; when the temperature is between 0-60 ℃, the mechanical index values are small and when the temperature is between -30-30 ℃, the drop of asphalt mixture indicators is large. In the range of 30-60 ℃, the downward trend of the mechanical index of the same class and different combination material types slows down, and the change of the mechanical index of asphalt mixture is not obvious.

(2) The asphalt mixture dynamics and static modulus have differences in terms of moulding method and loading method, and the test specimen preparation method has unevenness between static pressure and hard-hitting. Asphalt blend springing modulus is greatly influenced by temperature and loading frequency, and there are different multiplier relationships between dynamic and static module at different temperatures and loading frequencies. By dividing the entire temperature range (-30-60 ℃), combined with test data, domestic and foreign research results and specification recommendations, this study obtained 4 times, 5 times and 7 times relationship

between dynamic and static modules in different temperature ranges (-30-0 ℃, 0-30 ℃ and 40-60 ℃), respectively.

(3) There is an exponential function between the mechanical specifications of the asphalt mix and the temperature. According to the relationship between the indicators and temperature and the PGm-n grade of the asphalt pavement climate zone in China, the proposed value of asphalt pavement design parameters is established. The results of the study are of some theoretical and practical value to the design of asphalt pavement.

ACKNOWLEDGEMENTS

The authors gratefully appreciate the supports from the province key laboratory of road in Northeast Forestry University and the project of Heilongjiang Traffic and Transportation Department.

REFERENCES

[1] Qian G, Shi C, Yu H, et al. Evaluation of different modulus input on the mechanical responses of asphalt pavement based on field measurements[J]. Construction and Building Materials, 2021, 312: 125299.
[2] Khasawneh M A, Al-jamal N F. Modeling resilient modulus of fine-grained materials using different statistical techniques[J]. Transportation Geotechnics, 2019, 21: 100263.
[3] Shafabakhsh G, Tanakizadeh A. Investigation of loading features effects on resilient modulus of asphalt mixtures using Adaptive Neuro-Fuzzy Inference System[J]. Construction and Building Materials, 2015, 76: 256-263.
[4] Ibrahim H, Wahhab A A, Hasnain J. Laboratory study of asphalt concrete durability in Jeddah[J]. Building and environment, 1998, 33(4): 219-230.
[5] Saberian M, Li J. Effect of freeze–thaw cycles on the resilient moduli and unconfined compressive strength of rubberized recycled concrete aggregate as pavement base/subbase[J]. Transportation Geotechnics, 2021, 27: 100477.
[6] Yousefi A, Behnood A, Nowruzi A, et al. Performance evaluation of asphalt mixtures containing warm mix asphalt (WMA) additives and reclaimed asphalt pavement (RAP)[J]. Construction and Building Materials, 2021, 268: 121200.
[7] Elliott R P, Thornton S I. Resilient modulus and AASHTO pavement design[J]. Transportation research record, 1988 (1196)
[8] Maher A, Bennert T A. Evaluation of Poisson's ratio for use in the mechanistic empirical pavement design guide (MEPDG)[R]. 2008.
[9] Su N, Xiao F, Wang J, et al. Characterizations of base and subbase layers for Mechanistic-Empirical Pavement Design[J]. Construction and Building Materials, 2017, 152: 731-745.
[10] Hossain Z, Zaman M, Doiron C, et al. Characterization of subgrade resilient modulus for pavement design[M]//Geo-Frontiers 2011: Advances in Geotechnical Engineering. 2011: 4823-4832.
[11] Zhang Y, Luo R, Lytton R L. Anisotropic viscoelastic properties of undamaged asphalt mixtures[J]. Journal of Transportation Engineering, 2012, 138(1): 75-89.
[12] Specht L P, Lucas F, Di Benedetto H, et al. Application of the theory of viscoelasticity to evaluate the resilient modulus test in asphalt mixes[J]. Construction and Building Materials, 2017, 149: 648-658.
[13] Guo M, Liang M, Jiao Y, et al. A review of phase change materials in asphalt binder and asphalt mixture[J]. Construction and Building Materials, 2020, 258: 119565.
[14] Si W, Li N, Ma B, et al. Temperature response to tensile characteristics of the hot asphalt mixtures[J]. KSCE Journal of Civil Engineering, 2016, 20(4): 1336-1346.
[15] Moreno-Navarro F, Sol-Sánchez M, Rubio-Gámez M C, et al. The use of additives for the improvement of the mechanical behavior of high modulus asphalt mixes[J]. Construction and Building Materials, 2014, 70: 65-70.
[16] Zhang J, Fan Z, Wang H, et al. Prediction of dynamic modulus of asphalt mixture using micromechanical method with radial distribution functions[J]. Materials and Structures, 2019, 52(2): 1-12.
[17] Salem H A, Uzelac D, Matic B. Temperature zoning of Libya desert for asphalt mix design[C]//Applied Mechanics and Materials. Trans Tech Publications Ltd, 2014, 638: 1414-1426.
[18] Tan Y, Sun Z, Gong X, et al. Design parameter of low-temperature performance for asphalt mixtures in cold regions[J]. Construction and Building Materials, 2017, 155: 1179-1187.

[19] Copeland A, D'Angelo J, Dongre R, et al. Field evaluation of high reclaimed asphalt pavement–warm-mix asphalt project in Florida: Case study[J]. Transportation Research Record, 2010, 2179(1): 93-101.
[20] Wu S, Ye Q, Li N. Investigation of rheological and fatigue properties of asphalt mixtures containing polyester fibers[J]. Construction and Building Materials, 2008, 22(10): 2111-2115.

CIVIL ENGINEERING JOURNAL

Article no. 4

THE CIVIL ENGINEERING JOURNAL 1-2023

AN INVESTIGATION OF DAMPING MODIFICATION FACTORS CORRESPONDING TO DIFFERENT DAMPING RATIOS FOR SDOF SYSTEMS

Emre Çağlar Çelik[1] and Onur Merter[2]

1. Politecnico di Milano, School of Civil, Environmental and Land Management Engineering, Milano, Italy; emrecaglar.celik@mail.polimi.it

*2. İzmir University of Economics, Faculty of Engineering, Department of Civil Engineering, Balçova, İzmir, Turkey; *onur.merter@ieu.edu.tr*

ABSTRACT

The damping ratio is an important parameter in dynamic analyses and plays a key role in the design of building structures. Elastic response spectra are widely used in this design to describe the earthquake action in specific site classes. 5% damped response spectra are generally used for most of the conventional structures. However, other types of structures may not have a damping ratio of 5% and can have much lower or much larger damping ratios. The damping ratio is recommended at about 5% for concrete structures whereas it is estimated at 2% for steel structures. Tall slender buildings may have much lower damping ratios and low-rise buildings may be designed using much larger damping ratios than 5%. For these types of buildings, elastic response spectra are modified to account for different levels of damping ratios. This study proposes the damping modification factors (DMFs) which are computed using 5% damped response spectra as the benchmark. A strong ground motion set has been selected for the stiff site class and the displacement, pseudo-velocity, and pseudo-acceleration response spectra have been computed for single-degree-of-freedom (SDOF) systems. DMFs have been obtained in terms of these spectra and 3%, 10%, 20%, and 30% damping ratios have been considered. Variations of DMFs with different damping ratios have been obtained graphically. It can be seen from the results that DMFs are sensitive to the vibration period of the SDOF system.

KEYWORDS

Damping modification factor, Damping ratio, Site class, Elastic response spectra, Strong ground motion, Single-degree-of-freedom system

INTRODUCTION

Damping parameters play a significant role in dynamic analyses and the structural displacements decrease due to the increase in the damping. A 5% damping ratio is generally used for concrete structures and this ratio can vary depending upon many factors such as structure types, energy dissipation devices in buildings, changes in building heights and etc. [1-5]. High-rise buildings may have lower damping ratios whereas low-rise buildings have generally larger values. The damping ratio values decrease as the height of the building increases [4-6] and the estimation of the seismic response of tall buildings requires the damping ratio to be known [7]. In the seismic design of buildings in the United States, the damping ratio value is commonly recommended as lower than 2.5% for buildings higher than 150 m [7]. In addition to this, seismic energy dissipation devices may be installed in buildings to increase the damping ratio values and reduce structural damage [8].

Structures with these seismic energy devices generally have damping ratios above 10% for the first mode and much larger damping ratios for higher modes [4].

Response spectra are important tools in the seismic design of structures and engineers generally use 5%-damped pseudo-acceleration response spectra for typical structures. These spectra define the maximum responses of SDOF systems for specific ground motions. In widespread engineering applications, the most common method to define the seismic design loads that will affect an engineering structure is via the use of pseudo-acceleration spectral ordinates [5], and for this reason, the design acceleration spectra are described in many codes and regulations. In national and international seismic design codes, 5%-damped earthquake design spectra are usually generated for a specific territory using data on past earthquake ground motions.

For structural systems having damping ratios different than 5%, damping modification factors (DMFs) have been defined to estimate the seismic demands. These factors have been developed to make the conversion between a 5%-damped system and the other system having various damping ratios [5, 9]. The study to define DMF was first conducted by Newmark and Hall [10] and this pioneering study pointed out that these factors depend upon the natural vibration period of the system [5]. After Newmark and Hall's research, their relationship was adopted in ATC-40 [11] and FEMA 273 [12], [9]. Then, many seismic design codes such as UBC (1997) [13], Eurocode 8 (2004) [14], ASCE 7-05 (2006) [15], and NTCS-17 (2017) [16] proposed the DMF as a function of damping ratio. Priestley et al. [17] proposed a revision for the DMF relation in Eurocode 8 (2004) [14] for soil sites where forward directivity velocity pulse characteristics may be expected [9].

In this study, a total of 20 earthquake ground motion accelerograms are selected from the NGA-West2 strong ground motion database of the Pacific Earthquake Engineering Research Center (PEER) [18]. The site condition of the compiled accelerograms is defined in terms of the average shear wave velocity to the 30-meter depth of subsoil (in terms of V_{S30} Velocity). Site class ZD of the Turkish Building Earthquake Code (stiff soil with 180 m/s$<V_{S30}\leq$360 m/s) is considered in the selection of accelerograms [19]. The fault rupture mechanism of the considered accelerograms is strike-slip and moment magnitudes (M_w) are in the range of 6 to 7.9. Far-fault records are selected and the closest distances from the sites to the fault rupture planes (the rupture distances) are considered more than 15 km (R_{rup}>15 km).

The displacement, pseudo-velocity, and pseudo-acceleration elastic response spectra of selected earthquakes are computed for 3%, 5%, 10%, 20%, and 30% damping ratios respectively. In the calculation process, SeismoSpect software is used [20]. DMFs are computed by considering 5%-damped response spectra as the benchmark and DMF relations are obtained depending upon the natural vibration period of the SDOF system. 3%, 10%, 20%, and 30%-damped DMF graphs are created by considering the displacement, pseudo-velocity, and pseudo-acceleration response spectra, and the mean DMFs are indicated in the same diagrams. Variations of DMFs with different damping ratios are also obtained graphically within the study. These diagrams are constituted for constant natural vibration periods of T_n=0.5 s, 1.0 s, 1.5 s, 2.0 s, 2.5 s, 3.0 s, 3.5 s, and 4.0 s respectively. It can be seen from the results that DMFs are sensitive to the natural vibration periods of SDOF systems. Additionally, for a specific natural vibration period value, it can also be seen from the graphs that the mean DMFs generally tend to decrease with the increase in the damping ratio. This result is consistent with the basic property of the response spectra and it could be defined as follows: "Response spectra ordinates decrease for the increasing values of damping ratio".

In this study, DMFs are computed by only using the selected earthquake ground motion accelerograms recorded at stiff soil sites. More specifically, using a larger number of earthquake record data one can conclude more exact results about the DMF variation with the natural vibration period of the constant-damped SDOF system. Nevertheless, within the study, the DMF variation is investigated on a small scale and one of the important results can be given as the sensitivity of DMFs to changes in the vibration periods. Various general conclusions can also be drawn from this small-scale study. For example; if requested, one can directly compute the displacement, pseudo-velocity, and pseudo-acceleration elastic response spectra of SDOF systems having different damping ratios, from the DMF relations.

DAMPING MODIFICATION FACTOR

The damping modification factor in terms of spectral displacement (DMF_d) can be generally defined as [4, 5]:

$$DMF_d = \frac{S_d(T,\xi)}{S_d(T,\xi{:}5\%)} \quad (1)$$

where $S_d(T,\xi)$ is the spectral displacement of a linear elastic SDOF system having the damping ratio of ξ and $S_d(T,\xi{:}5\%)$ is the spectral displacement of the 5%-damped linear elastic SDOF system. T represents the natural vibration period of the system. The damping modification factor can also be obtained by using the spectral velocity $PS_V(T,\xi{:}5\%)$ and the spectral acceleration $PS_a(T,\xi{:}5\%)$. In this conversion, the natural frequency ω_n can be used, and multiplying $S_d(T,\xi)$ by ω_n one can obtain $PS_V(T,\xi)$ (Equ. (2)). In a similar way, $PS_a(T,\xi)$ can be obtained by multiplying $S_d(T,\xi)$ by ω_n^2 (Equ. (3)).

$$DMF_V = \frac{PS_V(T,\xi)}{PS_V(T,\xi{:}5\%)} \quad (2)$$

$$DMF_a = \frac{PS_a(T,\xi)}{PS_a(T,\xi{:}5\%)} \quad (3)$$

In these equations, $PS_V(T,\xi{:}5\%)$ and $PS_a(T,\xi{:}5\%)$ represent the spectral velocity and spectral acceleration of the 5%-damped linear elastic SDOF system (pseudo-velocity and pseudo-acceleration). Damping modification factors (DMF_d, DMF_V, and DMF_a) in Equations (1-3) are defined to estimate the seismic demands of structural systems having damping ratios different than 5%. DMFs are developed to make the conversion between a 5%-damped system and the other system having various damping ratios such as ξ [5, 9].

Damping modification factors in different seismic design codes

The study to define DMF was first conducted by Newmark and Hall [10] and this pioneering study pointed out that these factors depend upon the natural vibration period [5]. This study inspired scientists in this field and afterward, the adoption of DMFs to many seismic design codes was made [9]. The DMF in Eurocode 8 can be stated in terms of the viscous damping ratio ξ as follows [9, 14]:

$$DMF = \sqrt{\frac{10}{5+\xi}} \geq 0.55 \quad (4)$$

Priestley et. al suggested a revision for the DMF in Eurocode 8, especially for sites where forward directivity velocity pulse characteristics might be expected [9, 17, 21-25].

$$DMF = \left(\frac{7}{2+\xi}\right)^{0.25} \quad (5)$$

In the Chinese Standard (The Standard Code for Seismic Design of Buildings: GB 50011-2010), the seismic design response spectra are adjusted for different damping ratios by using the DMF in equation (6) [26]:

$$DMF = 1 + \frac{0.05-\xi}{0.08+1.6\xi} \geq 0.55 \quad (6)$$

In the Japanese Seismic Design Code, the damping correction (modification) factor is defined in terms of the viscous damping ratio ξ as follows [27]:

$$DMF = \frac{1.5}{(1+10\xi)} \geq 0.4 \quad (7)$$

These examples can be increased for DMFs and one can obtain different DMF relations in terms of the viscous damping ratio ξ from many different seismic design codes [9]. In Figure1, these

code-based DMF relations (in Equations 4-7) are presented based on different viscous damping ratios.

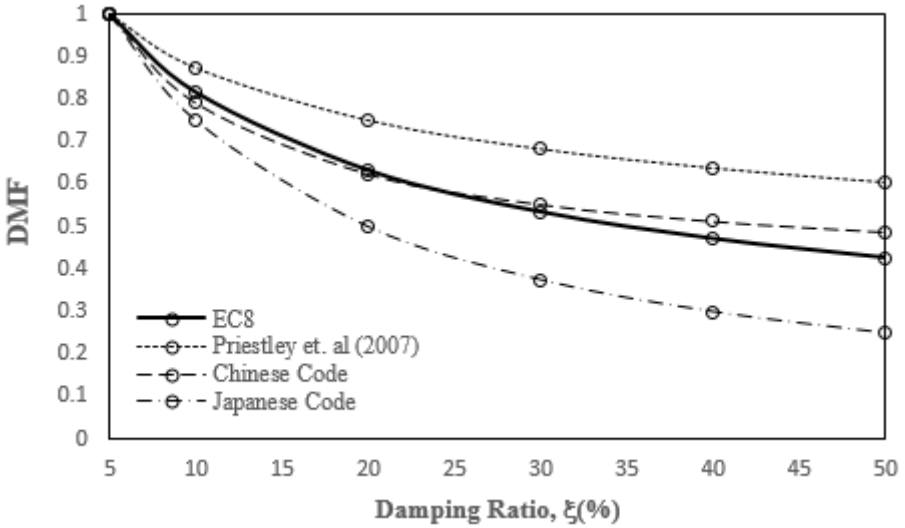

Fig. 1 – Damping modification factors (DMFs) according to Equations 4-7.

SELECTED EARTHQUAKE GROUND MOTIONS

A total of 20 real earthquake records are selected from the NGA-West2 strong ground motion database of the Pacific Earthquake Engineering Research Center (PEER) [18]. Site class ZD (stiff soil with 180 m/s < V_{S30}≤360 m/s) is considered according to the Turkish Building Earthquake Code [19]. The fault rupture mechanism of the considered ground motion records is strike-slip. Moment magnitudes (M_w) vary in the range of 6 to 7.9 and only far-fault records have been considered. Selected ground motion records are listed in Tables 1 and 2, respectively. R_{JB} is the Joyner-Boore distance, R_{rup} is the closest distance to the rupture plane, PGA is the peak ground acceleration, PGV is the peak ground velocity, PGD is the peak ground displacement, $D_{a5\text{-}95}$ is the significant duration and I_a is the Arias intensity. The distribution of PGA of the selected records within the study is demonstrated in Figure 2 with respect to R_{rup}.

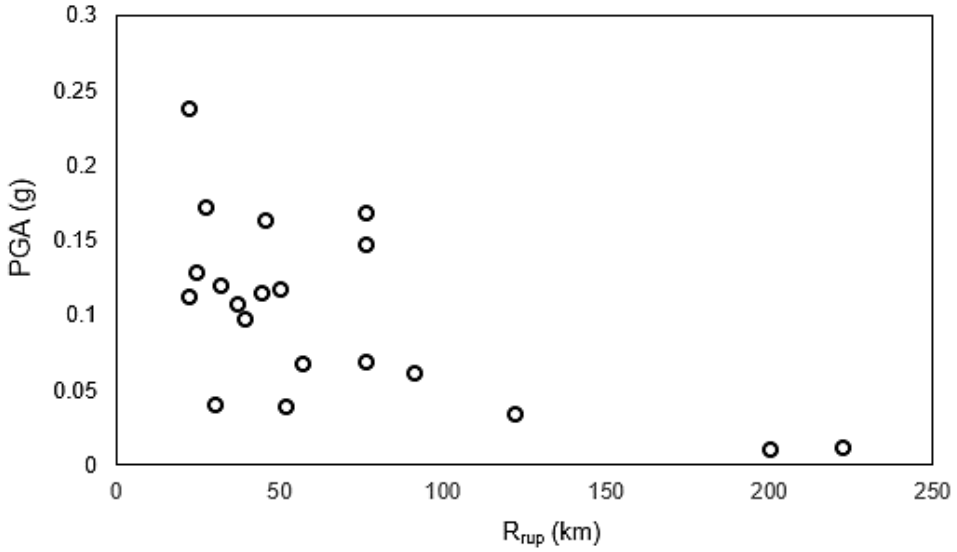

Fig. 2 – Distribution of PGA of the selected records with respect to R_{rup}.

Tab. 1 - Information on the selected ground motion records (Earthquakes 1-10) [18]

Record ID	Station Code	V_{S30} (m/s)	Site Class	R_{JB} (km)	R_{rup} (km)	PGA (g)	PGV (cm/sec)	PGD (cm)	D_{a5-95} (sec)	I_a (m/s)
EQ 1	Ferndale City Hall	219.31	ZD	91.15	91.22	0.062	4.417	1.201	22.2	0
EQ 2	Ferndale City Hall	219.31	ZD	44.52	44.68	0.116	6.090	0.643	15.5	0.1
EQ 3	El Centro Array #9	213.44	ZD	56.88	56.88	0.068	6.438	4.213	37.2	0.1
EQ 4	Ferndale City Hall	219.31	ZD	26.72	27.02	0.172	38.242	14.593	19.4	0.5
EQ 5	El Centro Array #9	213.44	ZD	121.00	121.7	0.035	3.996	0.920	40.9	0.1
EQ 6	El Centro Array #9	213.44	ZD	45.12	45.66	0.163	24.928	10.180	49.3	0.2
EQ 7	LA - Hollywood Stor FF	316.46	ZD	222.42	222.42	0.012	3.188	1.313	26.3	0
EQ 8	LB - Terminal Island	217.92	ZD	199.84	199.84	0.011	2.710	1.770	37.9	0
EQ 9	Calipatria Fire Station	205.78	ZD	23.17	24.60	0.130	12.834	8.553	25.9	0.1
EQ 10	Coachella Canal #4	336.49	ZD	49.10	50.10	0.118	11.139	3.397	11.1	0.2

Elastic response spectra of the selected earthquakes

Displacement, pseudo-velocity, and pseudo-acceleration response spectra of the selected earthquake ground motions are obtained within the study by using SeismoSpect software [20]. Viscous damping ratios are selected 3%, 5%, 10%, 20%, and 30%, respectively. As is seen from the mean spectra in Figure 3, spectral values generally decrease as the damping ratios increase. Using the natural frequency ω_n, the pseudo-velocity PS_V can be obtained in terms of the spectral displacement S_d as [28]:

$$PS_V = S_d \omega_n \tag{8}$$

In the same way, the pseudo-acceleration PS_a can be determined by using the natural frequency ω_n and the spectral displacement S_d as:

$$PS_a = S_d \omega_n^2 \tag{9}$$

As is known from structural dynamics, the dynamic equilibrium equation of a linear-elastic SDOF system can be written by [28]:

$$m\ddot{u} + c\dot{u} + ku = -m\ddot{u}_g \tag{10}$$

where m is the mass, u is the relative displacement, c is the damping coefficient, k is the stiffness and $\ddot{u}_g$ is the acceleration of the ground motion. One can determine the peak displacement from this equation (u_{max}: S_d) and the relation between the peak displacement and the natural vibration period T can be obtained (the displacement spectra). Using Equations (8) and (9), the pseudo-velocity PS_V and the pseudo-acceleration PS_a can be determined as in Figure 3.

Tab. 2 - Information on the selected ground motion records (Earthquakes 11-20) [18]

Record ID	Station Code	V_{S30} (m/s)	Site Class	R_{JB} (km)	R_{rup} (km)	PGA (g)	PGV (cm/sec)	PGD (cm)	D_{a5-95} (sec)	I_a (m/s)
EQ 11	Delta	242.05	ZD	22.03	22.03	0.239	26.882	13.624	51.4	3.3
EQ 12	El Centro Array #13	249.92	ZD	21.98	21.98	0.113	15.370	8.246	21.6	0.3
EQ 13	Niland Fire Station	212.00	ZD	35.64	36.92	0.108	11.014	5.098	26.4	0.2
EQ 14	Plaster City	316.64	ZD	30.33	30.33	0.041	3.144	1.204	10.8	0.1
EQ 15	Victoria	242.05	ZD	31.92	31.92	0.121	7.435	2.166	34.3	0.3
EQ 16	SAHOP Casa Flores	259.59	ZD	39.10	39.30	0.098	7.353	1.542	11.0	0.1
EQ 17	Rio Dell Overpass - FF	311.75	ZD	76.06	76.26	0.069	8.037	3.603	12.4	0.2
EQ 18	Rio Dell Overpass. E Ground	311.75	ZD	76.06	76.26	0.169	11.005	3.250	12.3	0.4
EQ 19	Rio Dell Overpass. W Ground	311.75	ZD	76.06	76.26	0.147	10.965	3.114	10.8	0.4
EQ 20	APEEL 1E - Hayward	219.8	ZD	51.68	51.69	0.039	2.755	0.656	35.2	0

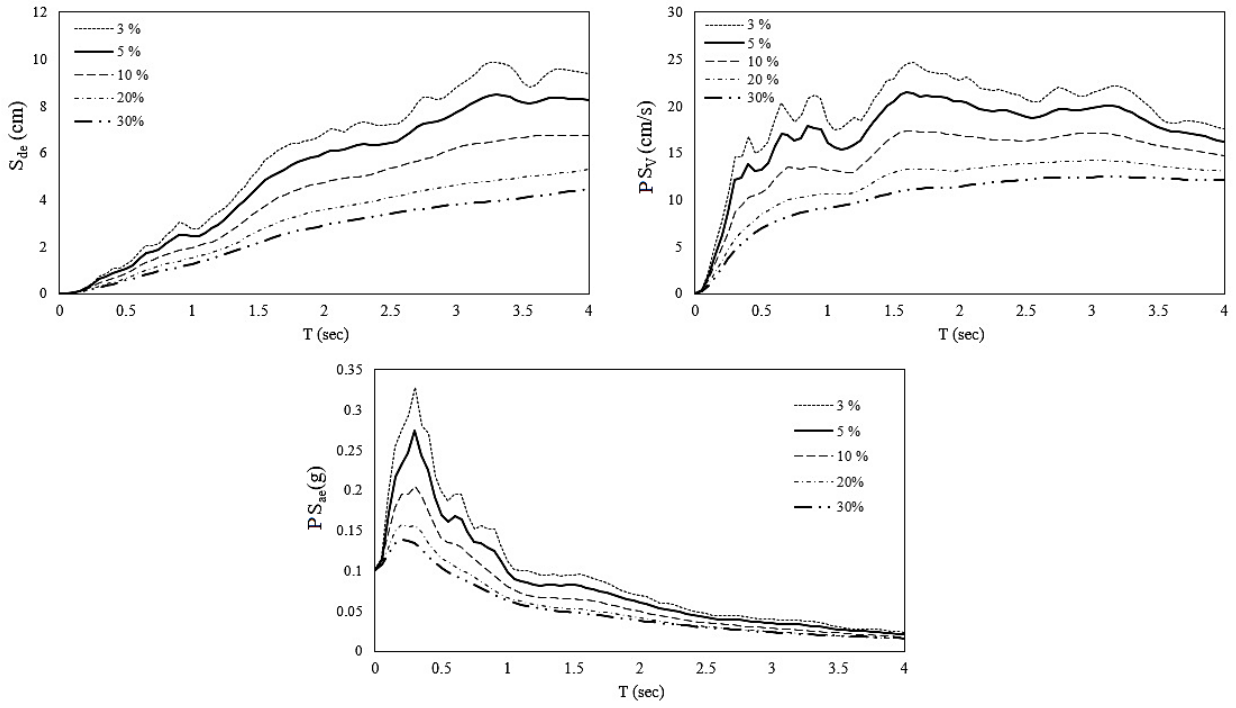

Fig. 3 – The mean elastic response spectra of the selected ground motions [in Tables 1 and 2] for 3%, 5%, 10%, 20%, and 30% viscous damping ratios.

VARIATION OF DAMPING MODIFICATION FACTORS FOR SELECTED EARTHQUAKE GROUND MOTIONS

In this study, DMFs have been computed for the selected earthquake ground motions. 5%-damped elastic response spectra have been selected as the benchmark and DMFs have been computed depending on the natural vibration period of the elastic SDOF system. 3%, 10%, 20%, and 30%-damped DMFs have been computed by considering the displacement (S_d), pseudo-velocity (PS_V), and pseudo-acceleration (PS_a) response spectra, and the mean DMFs have been indicated in the same diagrams (Figures 4-6). The values of mean DMFs have been presented in Table 3.

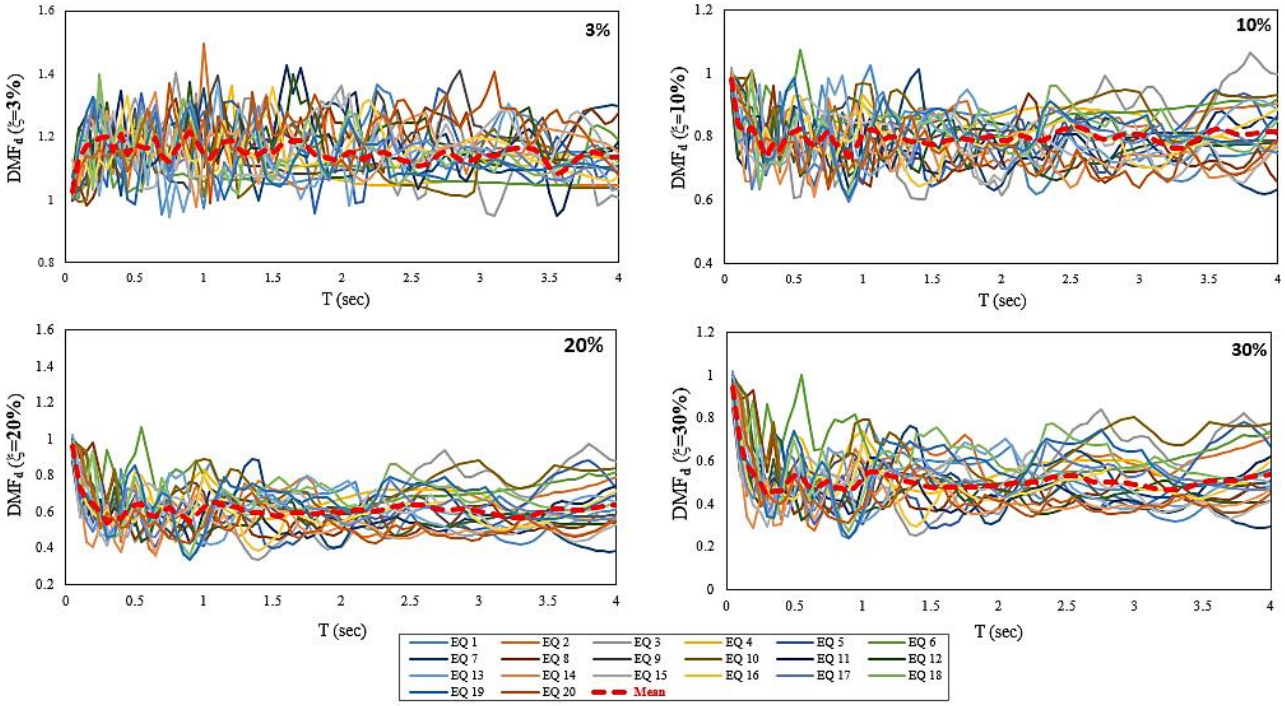

Fig. 4 – The variation of DMF_d (in terms of spectral displacement S_d) for the selected earthquake ground motions [for ξ: 3%, 10%, 20%, and 30%].

Tab. 3 - Mean DMFs with respect to S_d, PS_V, and PS_a (for different periods and ξ)

	ξ: 3%			ξ: 10%			ξ: 20%			ξ: 30%		
T	DMF S_d	DMF PS_V	DMF PS_a	DMF S_d	DMF PS_V	DMF PS_a	DMF S_d	DMF PS_V	DMF PS_a	DMF S_d	DMF PS_V	DMF PS_a
0.2 sec	1.215	1.179	1.177	0.829	0.775	0.838	0.643	0.556	0.671	0.546	0.444	0.595
0.5 sec	1.159	1.177	1.173	0.818	0.816	0.829	0.639	0.644	0.684	0.533	0.530	0.613
1.0 sec	1.146	1.143	1.138	0.807	0.820	0.822	0.625	0.658	0.682	0.521	0.567	0.635
1.5 sec	1.116	1.148	1.143	0.775	0.819	0.791	0.582	0.629	0.638	0.477	0.525	0.582
2.0 sec	1.108	1.137	1.132	0.789	0.822	0.808	0.595	0.641	0.675	0.483	0.555	0.625
3.0 sec	1.080	1.142	1.137	0.806	0.865	0.823	0.602	0.716	0.698	0.493	0.626	0.677
4.0 sec	1.084	1.136	1.130	0.817	0.906	0.844	0.639	0.806	0.749	0.540	0.746	0.776

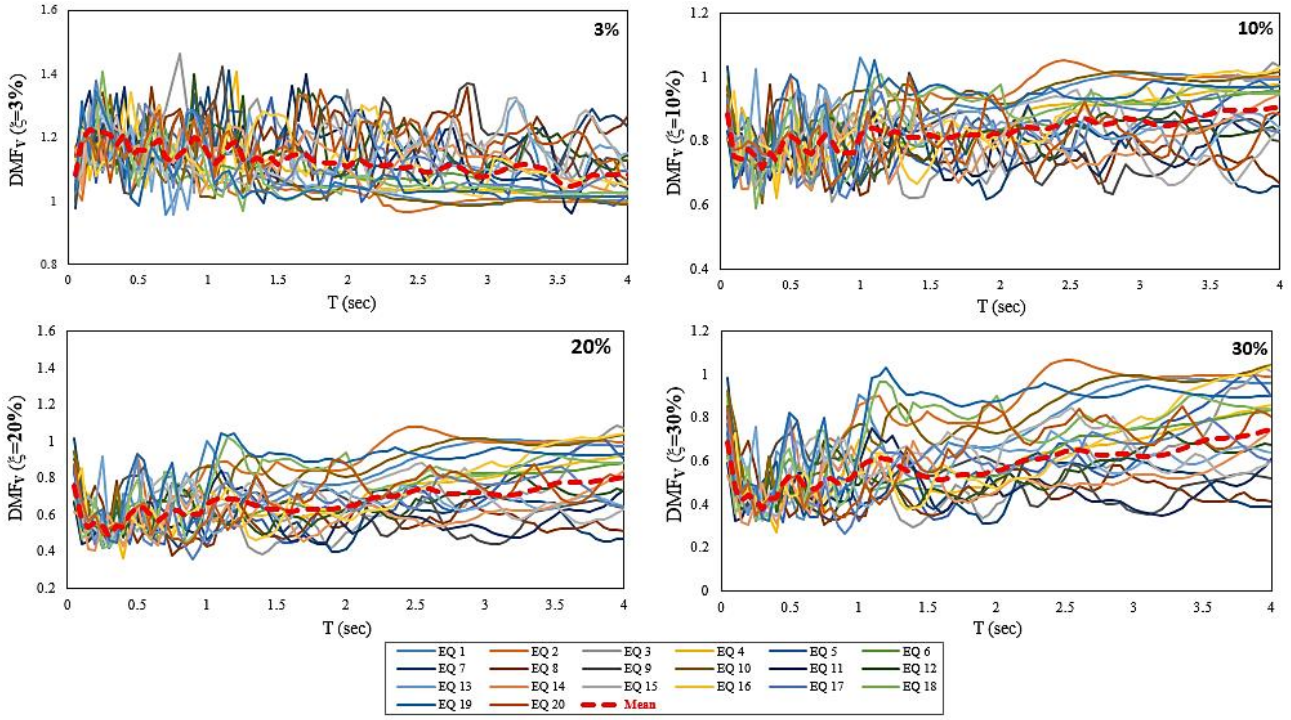

Fig. 5 – The variation of DMF_V (in terms of pseudo-velocity PS_V) for the selected earthquake ground motions [for ξ: 3%, 10%, 20%, and 30%].

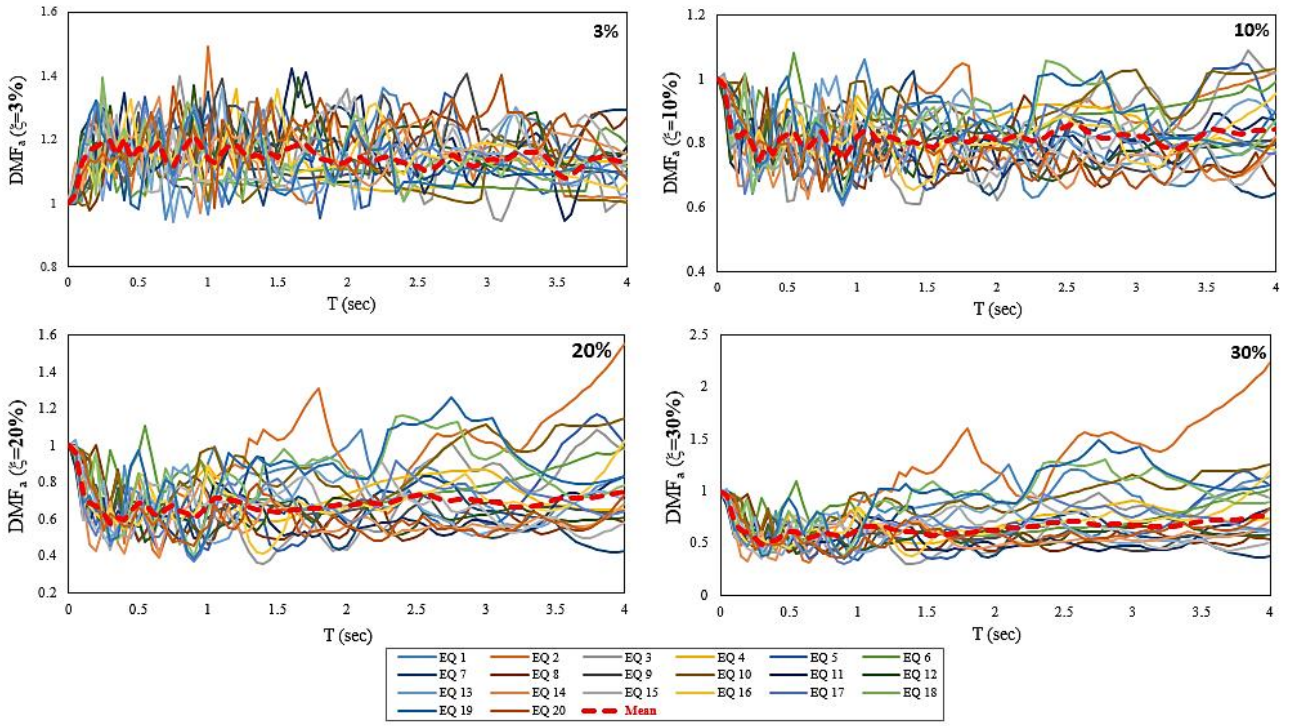

Fig. 6 – The variation of DMF_a (in terms of pseudo-acceleration PS_a) for the selected earthquake ground motions [for ξ: 3%, 10%, 20%, and 30%].

Mean DMF variations with respect to natural vibration periods

Mean DMF variations for the selected earthquake ground motions have been given in Figure 7. It can be clearly seen from the graphs that DMFs tend to decrease with the increase in viscous damping ratio. Mean DMF variations have been presented in terms of the ratios of displacement (S_d), pseudo-velocity (PS_V), and pseudo-acceleration (PS_a) response spectra. The damping ratio effect on DMF values has been observed (Figure 7).

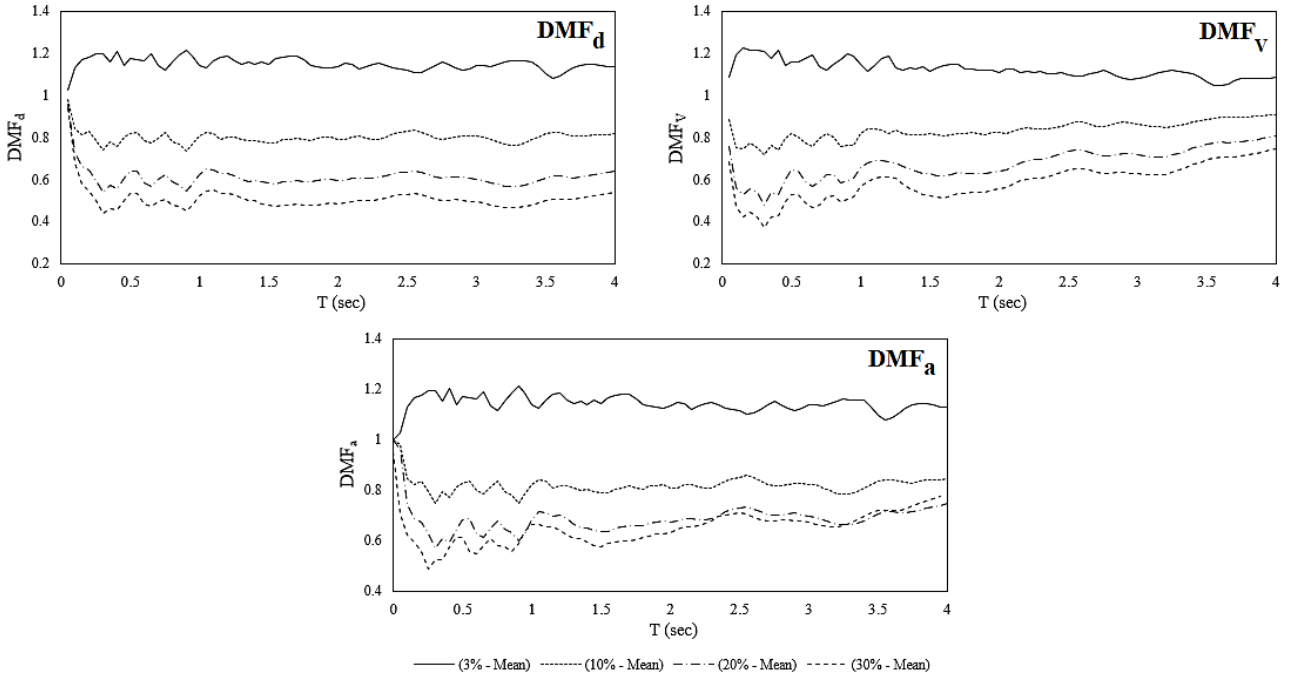

Fig. 7 – The variation of mean DMF_d, DMF_V, and DMF_a with respect to the natural vibration periods and viscous damping ratios of 3%, 10%, 20%, and 30%.

Mean DMF variations with respect to viscous damping ratios

In this study, Mean DMF variations for the selected earthquake ground motions have been presented in terms of viscous damping ratios, too. Once again, it is seen from the graphs that the mean DMFs tend to decrease with the increase in viscous damping ratios. In Figure 8, mean DMFs have been indicated for different viscous damping ratios of 3%, 10%, 20%, and 30%. In this figure, mean DMFs have been presented for all natural vibration periods of the elastic spectra. It can be seen from the figure that the mean DMF interval is scattered as the viscous damping ratio increases up to 30%. For the damping ratio of 3%, mean DMFs have been obtained very close to each other at different natural vibration periods.

DMF_d, DMF_V, and DMF_a variations with respect to the viscous damping ratios have been presented in Figure 9, for different natural vibration periods. In this figure mean DMFs have been considered for natural vibration periods of T_n=0.5 s, 1.0 s, 1.5 s, 2.0 s, 2.5 s, 3.0 s, 3.5 s, and 4.0 s, respectively. Generally, for all periods, DMF values computed in terms of the ratios of spectral displacement, pseudo-velocity, and pseudo-acceleration response spectra (DMF_d, DMF_V, and DMF_a) tend to decrease for increasing values of viscous damping ratios (Figure 9). 5%-damped elastic response spectra have been selected as the benchmark within these computations (as given in Equations 1, 2, and 3).

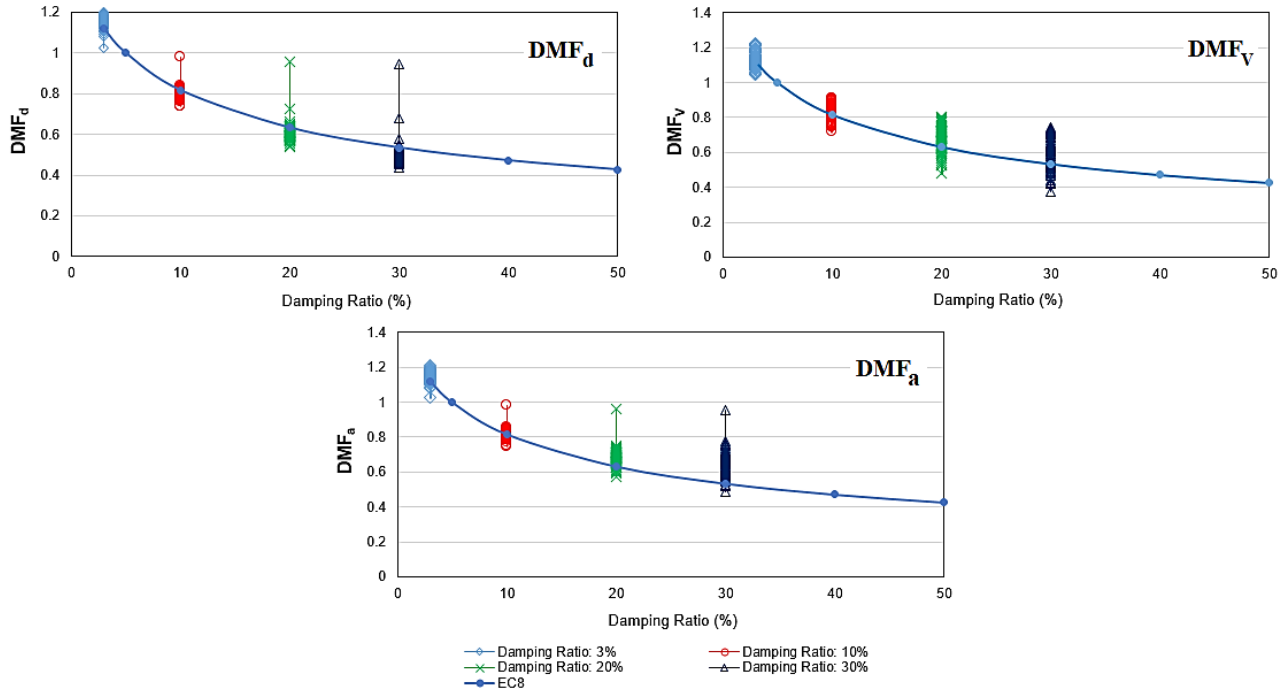

Fig. 8 – The variation of mean DMF_d, DMF_V, and DMF_a with respect to the viscous damping ratios, and DMF variation according to Equation 4 (Equation in Eurocode 8).

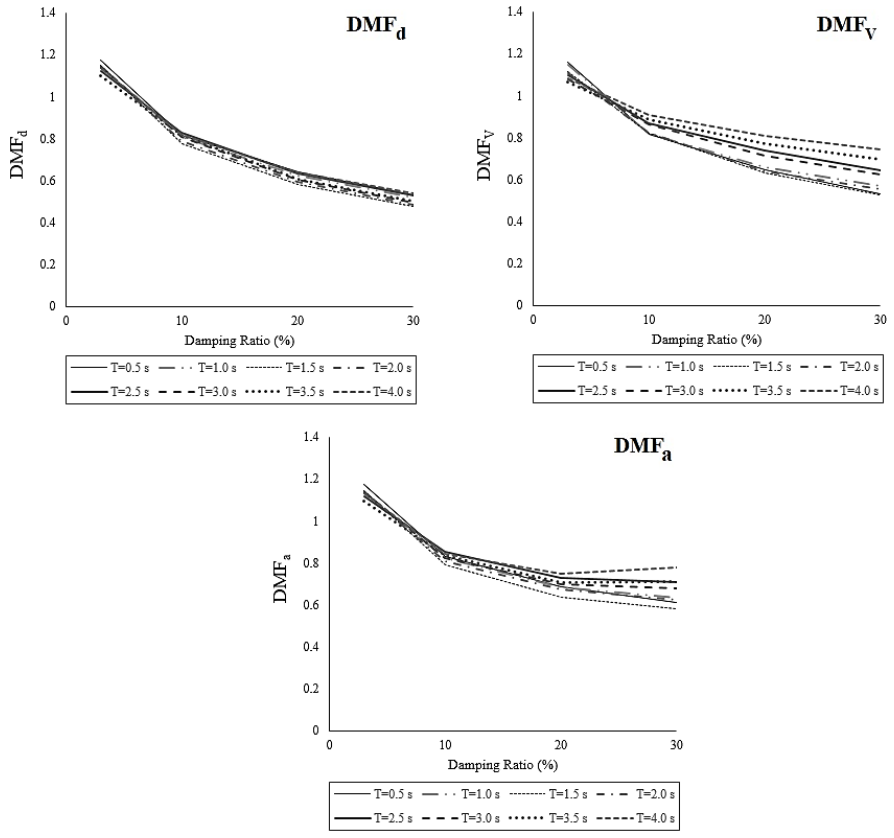

Fig. 9 – DMF_d, DMF_V, and DMF_a variations with respect to the viscous damping ratios.

DOI 10.14311/CEJ.2023.01.0004

CONCLUSION

The primary objective of this study is to investigate the damping modification factors, DMFs, for the selected earthquake ground motion accelerograms recorded at stiff soil sites with shear wave velocities less than 360 m/s. Computed DMFs modify 5%-damped spectral ordinates to estimate the seismic demands of structures whose damping ratio is different from 5%. DMFs have been obtained considering the displacement, pseudo-velocity, and pseudo-acceleration response spectra, and 3%, 10%, 20%, and 30% damping ratios have been considered. DMFs have been computed depending upon the natural vibration period of the elastic SDOF system, and variations of DMFs for different damping ratios have also been obtained graphically. It is seen from the graphs that DMFs are sensitive to the natural vibration periods of SDOF systems, and generally tend to decrease with the increase in the viscous damping ratio. The following conclusions can be drawn from the results of this study:

- DMFs have been obtained greater than 1.0 for 3% damping ratio whereas they have been obtained lower than 1.0 for all damping ratios greater than 5% (for damping ratios of 10%, 20%, and 30%). This is a natural result since DMFs are based on spectral values and since the displacement, pseudo-velocity, and pseudo-acceleration response spectra ordinates decrease with the increase in viscous damping ratios. As known, the DMF is the dimensionless ratio, and generally, 5%-damped spectral values are considered the benchmark. Therefore, when DMF is computed for structures like 3%-damped systems whose damping ratio is lower than 5% since the lower 5%-damped spectral value is in the denominator, the DMF is obtained greater than 1.0.
- For a constant natural vibration period of the SDOF system, it has been observed that the mean DMFs have decreased as the damping ratio has increased. Generally, between 3%- and 10%-damped systems, the difference in the mean DMFs has been obtained greater than that of the others.
- For longer natural vibration periods (especially for period values greater than 1.0 sec), the mean DMFs of the selected earthquake ground motions have been observed as tending to be nearly constant. For systems that have shorter natural vibration periods (especially for periods shorter than 0.3 sec), the mean DMFs have been observed as fluctuating.
- Mean DMF variations for the selected earthquake ground motions with respect to the viscous damping ratios have been obtained as compatible with the code-based DMF relations.

DMFs have been computed by only using the selected earthquake ground motion accelerograms recorded at stiff soil sites (on a small scale), within this study. More specifically, using a larger number of earthquake record data one can conclude more exact results about the DMF variation with the natural vibration period of the constant-damped SDOF systems.

REFERENCES

[1] Chowdhury I, Dasgupta, SP, 2003. Computation of Rayleigh Damping Co-efficient for Large Systems. Electronic Journal of Geotechnical Engineering, vol.43: 6855-6868.

[2] Mario P, 2004. Structural Dynamics: Theory and Computation, 2nd Edn. CBS Publishers and Distributors, New Delhi.

[3] Chopra AK, 2006. Dynamics of Structures, 3rd Edn. Wiley, London.

[4] Conde-Conde J, Benavent-Climent A, 2019. Construction of Elastic Spectra for High Damping. Engineering Structures, vol.191: 343-357.

[5] Davalos H, Miranda E, Bantis J, Cruz C, 2022. Response Spectral Damping Modification Factors for Structures Built on Soft Soils. Soil Dynamics and Earthquake Engineering, vol.154, https://doi.org/10.1016/j.soildyn.2022.107153.

[6] Ha T, Shin S-H, Kim H, 2020. Damping and Natural Period Evaluation of Tall RC Buildings Using Full-Scale Data in Korea. Applied Sciences, vol.10(5): 1568, https://doi.org/10.3390/app10051568.
[7] Cruz C, Miranda E, 2017. Evaluation of Damping Ratios for the Seismic Analysis of Tall Buildings. Journal of Structural Engineering, vol.143(1): 04016144, DOI:10.1061/(ASCE)ST.1943-541X.0001628.
[8] Hernandez F, Astroza R, Beltran JF, Belmar L, 2020. A Damper-Spring Device for Seismic Energy Dissipation in Buildings. 17th World Conference on Earthquake Engineering, 17WCEE, Paper No: C001492, Sendai, Japan.
[9] Sheikh MN, Tsang H-H, Yaghmaei-Sabegh S, Anbazhagan P, 2013. Evaluation of Damping Modification Factors for Seismic Response Spectra. Australian Earthquake Engineering Society 2013 Conference, November 15-17, Hobart, Tasmania.
[10] Newmark NM, Hall WJ, 1973. Procedures and Criteria for Earthquake Resistant Design. Building Practices for Disaster Mitigation, Building Science Series, vol. 46, National Bureu of Standards: Washington, DC. P. 209-23.
[11] ATC-40, 1996. Seismic Evaluation and Retrofit of Concrete Buildings. Applied Technology Council, Redwood City, CA.
[12] FEMA-273, 1997. NEHRP Guidelines for the Seismic Rehabilitation of Buildings. Federal Emergency Management Agency, Washington, DC, USA.
[13] UBC, 1997. Uniform Building Code. International Conference of Building Officials, Whittier, CA.
[14] Eurocode 8 (EC8), 2004. Design of Structures for Earthquake Resistance, Part 1: General Rules, Seismic Actions and Rules for Buildings. EN 2004-1-1, CEN, Brussels.
[15] ASCE 7-05, 2006. Minimum Design Loads for Buildings and Other Structures. American Society of Civil Engineers, 1801 Alexander Bell Drive, Reston, VA 20191, USA.
[16] Mexico City Building Code, 2017. Complementary Technical Standards for Earthquake Design in Regulation of Constructions of the Federal District. NTCS-17, Official Gazette of the City of Mexico, Mexico.
[17] Priestley MJN, Calvi GM, Kowalsky MJ, 2007. Displacement-Based Seismic Design of Structures. IUSS Press: Pavia, Italy.
[18] PEER, 2022. Pacific Earthquake Engineering Research Center Strong Ground Motion Database. http://ngawest2.berkeley.edu/.
[19] TBEC, 2018. Turkey Building Earthquake Code. Ministry of Public Works and Settlement, Ankara, Turkey.
[20] SeismoSpect, 2022. Seismosoft, Earthquake Engineering Software Solutions, Pavia, Italy, https://seismosoft.com/.
[21] Fernandez-Davila, VI, Mendo A., 2020. Damping Modification Factors for the Design of Seismic Isolation Systems in Peru, Earthquake Spectra, 1-28, DOI: 10.1177/8755293020926189.
[22] Cicek K, Erkus B, 2019. Damping Reduction Factors for Maximum Rotated Spectra for Analysis of Base-Isolated Structures. 5th International Conference on Earthquake Engineering and Seismology (5ICEES), 8-11 October, Ankara, Turkey.
[23] Cardone D, Dolce M, Rivelli M, 2009. Evaluation of Reduction Factors for High-Damping Design Response Spectra. Bulletin of Earthquake Engineering, vol.7, 273-291.
[24] Daneshvar P, Bouaanani N, Goda K, Atkinson GM, 2017. Damping Modification Factors for Deep Inslab and Interface Subduction Earthquakes. 16th World Conference on Earthquake, Paper No. 2827, January 9-13, Santiago, Chile.
[25] Daneshvar P, Bouaanani N, Goda K, Atkinson, GM, 2016. Damping Reduction Factors for Crustal, Inslab, and Interface Earthquakes Characterizing Seismic Hazard in Southwestern British Columbia, Canada. Earthquake Spectra, vol.32(1), 45-74, https://doi.org/10.1193/061414EQS086M.
[26] GB 50011, 2010. Code for Seismic Design of Buildings. China Architecture & Building Press, Beijing, China.
[27] BCJ, 1997. Structural Provisions for Building Structures. 1997 Edn-Tokyo: Building Center of Japan [in Japanese].
[28] Chopra AK, 1995. Dynamics of Structures, Theory and Applications to Earthquake Engineering, Prentice Hall, Upper Saddle River, N.J.

CIVIL ENGINEERING JOURNAL

Article no. 5

THE CIVIL ENGINEERING JOURNAL 1-2023

FRICTION TEST AND PARAMETER ANALYSIS OF PRESTRESSED CONCRETE CONTINUOUS BEAM BRIDGE

Qingxin Yu[1,2], Quansheng Sun[1] and Junyun Liu[1]

1. Northeast Forestry University, Department of Civil Engineering, Hexing road, Harbin, PR China; hrbsqs@126.com, w15776632879@163.com

2. Lianyungang Economic and Technological Development Zone Government Investment Engineering Service Center, Huaguoshan Avenue, Lianyungang, PR China; 2581814259@qq.com.

ABSTRACT

The prestressed ducts of prestressed concrete continuous girder bridges are usually three-dimensionally distributed and long in length. The control of prestress loss during construction is very important. In order to ensure the effect of prestress tensioning, the test and analysis of friction parameters of prestressed ducts are particularly important. Based on the tension process of a prestressed concrete continuous beam bridge, the initial tension stress, loading time and channel friction parameters of the prestressed concrete continuous beam bridge are tested by field tests. Combined with the measured friction parameters, the finite element software Midas / Civil is used to analyse the influence of friction parameters on the mechanical properties of prestressed concrete continuous beam bridge. The results show that when the prestressed steel with bending angle not more than 40° and length not more than 70 m is stretched, the initial tension stress is suggested to be set as 20 % of the tension control force and the loading time is 5 min. The measured tunnel friction parameters are larger than the standard value, and the tension control force should be adjusted during the formal tension construction ; The deflection of the key section of the main beam increases with the increase of the friction parameters, and the roof stress decreases with the increase of the friction parameters. The change of channel deviation coefficient has a greater impact on the deflection and roof stress than the change of friction coefficient.

KEYWORDS

Continuous beam bridge, Initial tensile stress, Loading time, Friction parameters, Deflection, Stress

INTRODUCTION

Prestressed concrete continuous beam bridge has been widely used due to its unique advantages, and has become the preferred bridge type for large-span bridges. With the continuous increase of the span of prestressed concrete continuous beam bridge, the length of the required prestressed reinforcement increases, but there are also some diseases caused by excessive prestress loss, such as mid-span deflection and box girder cracking [1]. According to the current design specification for highway bridges in China, among the six

factors of prestress loss in prestressed concrete bridges, the friction loss of prestressed ducts accounts for a relatively large proportion compared with the prestress loss caused by other factors, especially for long prestressed beams with large bending angles. [2]. The method of calculating prestress loss by pre-tensioning method has been proved to be feasible by a large number of tests. However, there are many factors affecting prestress loss in post-tensioning method. There are still some deviations between theoretical and experimental results of calculating prestress loss by post-tensioning method in Chinese code. Due to the complex stress condition of long prestressed reinforcement in concrete structure, it may also be affected by construction technology, prestressed material performance, environmental factors and other factors, and the prestress loss will be greater than that of ordinary prestressed reinforcement. [3-4]. Therefore, it is very necessary to study the friction loss test of the relative long prestressed reinforcement, so as to ensure that the prestress in the bridge structure meets the design requirements and prevent the safety problems of the bridge structure caused by the lack of effective prestress in the bridge structure.

Many scholars have carried out relevant research on the loss of prestress of bridge, Zhang Kaiyin et al [5] have carried out relevant experimental research on the friction loss of bending channel. It is concluded that with the increase of tension control force and bending angle, the friction loss of bending channel will also increase rapidly. LvPan [6] conducted sensitivity analysis on the main factors affecting the prestress loss through the finite element software Midas / Civil, and obtained the main sensitive factors affecting the prestress loss of bridges. Zhang Jingwei et al [7] pointed out that the friction loss of bending prestressed steel is greater than that of linear steel through the test of prestressed friction loss of high-speed railway long-span continuous beam bridge. With the increase of steel length, the friction loss value also increases, and the friction loss cannot be ignored. Zhang Qi et al[8] through the friction test of a three-span continuous box girder bridge as the research background, it is concluded that the pipeline friction loss accounts for a large proportion of prestress loss. In the process of tension, the prestress loss can be reduced by symmetrical synchronous tension at both ends, super tension and lubricant coating on prestressed reinforcement. Robitaille et al. [9] deduced the theoretical calculation formula for the prestress loss of the curved pipeline during the prestress tension process, and pointed out that when the bending angle of the prestressed steel bar exceeds 2.5°, the prestress loss in the prestressed structure will exceed 5%. Zollman et al. [10] studied the prestress loss of prestressed steel bars at the bending, and obtained the relationship between the bending angle and the prestress loss. Sapountzakis et al. [11-14] deduced and predicted the loss calculation formula of prestressed steel bar bending starting point and bending point in prestressed concrete bridge structure. However, there are relatively few systematic experimental studies on long-span continuous girder bridge length prestressing beams. This paper takes the tension process of a prestressed concrete continuous girder bridge as the research background, and tests the initial tension stress, load holding time and friction parameters through field tests, which provides a reference for the design and construction of similar bridges, and combines the measured values of friction parameters. , using finite element software to analyse the influence of friction parameters on the mechanical properties of prestressed concrete continuous girder bridges.

BACKGROUND

The new prestressed concrete continuous girder bridge studied in this paper is located in Hainan Province, China, with a total length of about 201.2 m. The upper structure of the bridge is 35m+40m+45m+40m+35m=195m, and the cast-in-place continuous box girder of Class A prestressed concrete is used. The bridge pier adopts the vase-type bridge pier to connect the pile foundation, the bridge abutment adopts the rib-type bridge abutment to connect the platform pile foundation, and the bridge pile foundation adopts the friction pile foundation. The cast-in-place continuous box girder adopts C50 concrete with an elastic modulus of 3.45×104MPa. The prestressed material is a low-relaxation high-strength steel strand with a tensile strength standard value of 1860 Mpa, a nominal diameter of d=15.2mm, an elastic modulus of Ep=1.95×105 Mpa, and a relaxation coefficient of 0.3. The prestressed pipe is formed by plastic bellows. The elevation layout, cross-section and prestressed steel bundle layout of the bridge are shown in Figures 1-3.

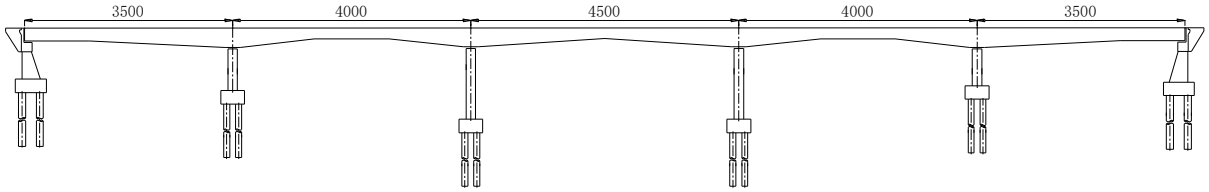

Fig.1 - Bridge Elevation Layout (Unit: cm)

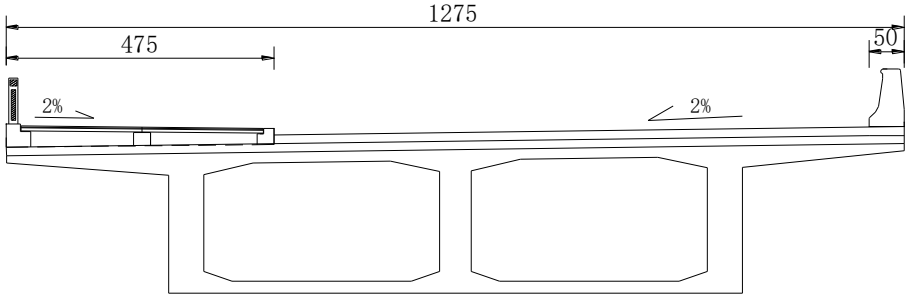

Fig.2 - Bridge cross section (Unit: cm)

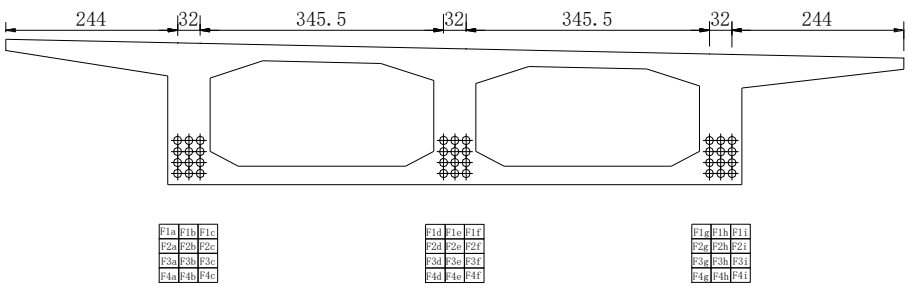

Fig.3 - Layout drawing of prestressed steel beams (Unit: cm)

Tab. 1 - Parameters of prestressed test bundles F1b, F3e, F4h in the first pouring section

Position of steel beam	Steel beam number	Length of steel beam /m	Channel bend angle /°	Specification
Side web	F1b	69.54	39.9°	9Φs15.2
Middle plate	F3e	69.07	33.4°	12Φs15.2
Side web	F4h	69.24	37.9°	12Φs15.2

TECHNICAL ROUTE

In this paper, according to the actual situation of the site, the prestressed test beam is selected for field test, and then the finite element software is used to establish the finite element model of the real bridge and the sensitivity analysis of the friction parameters of the prestressed pipeline is carried out in combination with the field test data. The influence of the value of the friction parameters of the prestressed pipeline on the mechanical properties of the bridge is studied and analyzed, so as to provide some reference for the construction and design.

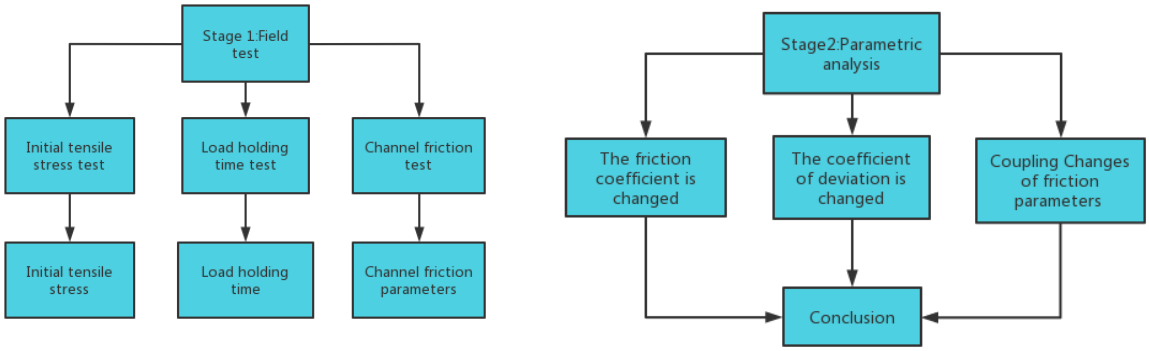

Fig.4 - Technology roadmap

FIELD TEST

In order to successfully complete the friction test, the initial tensile stress test and the load holding time test are usually carried out first. The initial tensile stress test can determine the initial tensile control stress, so as to offset the nonlinear influencing factors of the prestressed steel bundle in the tensioning process and reduce the prestress loss in the tensioning stage. The load holding time can be accurately determined by the load holding time test, and the stress loss can be reduced by controlling the load holding time during the prestressed tension construction process [15].

The field test instruments mainly include: pressure sensor, comprehensive tester, prestressed intelligent tensioning equipment, etc.

Fig. 5 - Field diagram of the pressure sensor

Fig. 6 - Field test diagram of comprehensive tester

Fig. 7 - Field Diagram of Intelligent Tensioning Equipment

Fig. 8 - Field test diagram

Initial tensile stress test

The initial tension is the first tension process in the tension stage of prestressed concrete bridges. The main purpose of the initial tension stage is to eliminate the inelastic deformation of prestressed reinforcement, which can also be understood as the process of gradual straightening of prestressed reinforcement. China ' s Technical Specification for Construction of Highway Bridges and Culverts ' (JTG / T3650-2020) points out that the tension control stress should be adjusted to the initial tension stress in the construction of prestressed bridges. The technical specification for construction of highway bridges and culverts requires that the initial tension stress should be 10 % ~ 25 % of the tension control stress. [16]. However, for the prestressed steel bars with long length or large bending angle, the prestressed transmission speed applied at the tensile end is slow and the prestress loss is large. It is necessary to measure the initial tensile stress through the field initial tensile stress test [17].

In order to determine the initial tensile stress of the bridge, this test selects the first pouring section of longitudinal web prestressed steel beam F1b, F3e to test the initial tensile stress. The test method is to apply prestress load to the tensile end from 0, and load according to 5 %, 10 %, 15 %, 20 %, 25 %, 30 %, 40 % load. For each stage of load after loading, test reading records tension and elongation data; when the elongation of the

prestressed steel beam at the tensile end tends to be stable under various loads and the tension ratio between the tensile end and the fixed end tends to be constant, the load grade can be defined as the initial tensile stress. The test results are shown in Tables 2, 3 and Figures 9, 10.

Tab. 2 - F1b Initial tensile stress test data table

Steel beam number	Load level	Driving end /kN	Passive end /kN	Passive end than active end /%
F1b	5%	84.9	15.3	18.2
	10%	169.9	76.5	45.3
	15%	254.8	153.4	60.2
	20%	339.7	234.4	69.4
	25%	424.7	293.0	69.3
	30%	509.6	351.6	69.3
	35%	593.3	411.8	69.4
	40%	679.4	468.8	69.5

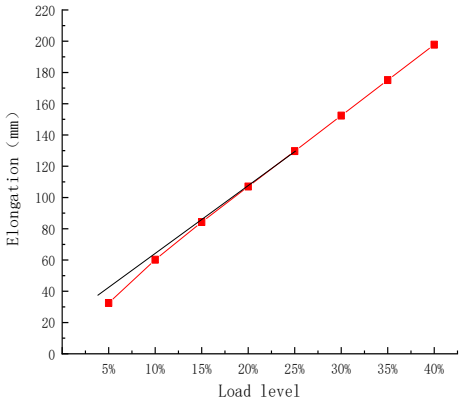

Fig. 9 - F1b Tension and elongation relationship curve

Tab. 3 - F3e initial tensile stress test data table

Steel beam number	Load level	Driving end /kN	Passive end /kN	Passive end than active end/%
F3e	5%	108.6	24.9	23.2
	10%	217.2	110.8	51.3
	15%	325.7	211.7	65.4
	20%	434.3	309.4	71.2
	25%	542.9	385.5	71.4
	30%	651.5	464.5	71.3
	35%	758.1	541.3	71.4
	40%	868.6	619.2	71.3

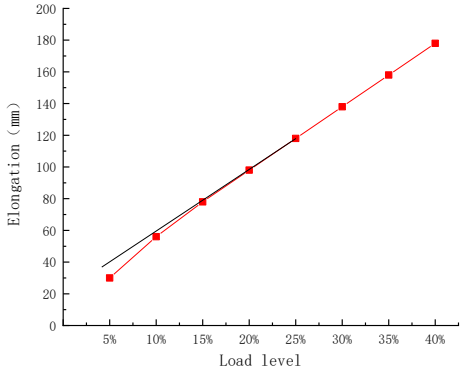

Fig. 10 - F3e tension and elongation relationship curve

From Table 2, 3 and Figures 9, 10, it can be seen that due to the large internal bending angle of prestressed pipe of prestressed concrete continuous beam bridge and the long steel, the stress is uneven, and the elongation of prestressed steel shows an irregular growth trend when the loading grade is small.

When the loading level gradually increases, the prestressed reinforcement eliminates the deformation caused by nonlinear factors; when the loading level is 20 % of the design load, the tensile ratio of the fixed end to the tension end tends to be stable, and the elongation of the prestressed reinforcement and the tensile force are linearly distributed. Therefore, in the tension process of this bridge, the initial stress is 20 % of the tension control stress.

Load holding time test

Because the prestressed reinforcement of the bridge is long and the bending channel is relatively complex, it takes a long time to pass the prestressed load on the tensile end to the fixed end. If the size of the load holding time can be accurately grasped in the prestressed tension construction process, the prestress loss of the reinforcement can be

reduced. In this experiment, the loading time of longitudinal web prestressed reinforcement F1b and F3e in the first pouring section was tested. The test method is to apply pre-stress load on the tension end. When the load is up to 40 %, the load is stopped, and the corresponding load is kept unchanged for 10 min. The pressure sensors at the tension end and the fixed end are recorded with time [18]. In order to facilitate the analysis, the test data of load holding time are plotted in this paper for analysis as shown in Figures 10 and 11.

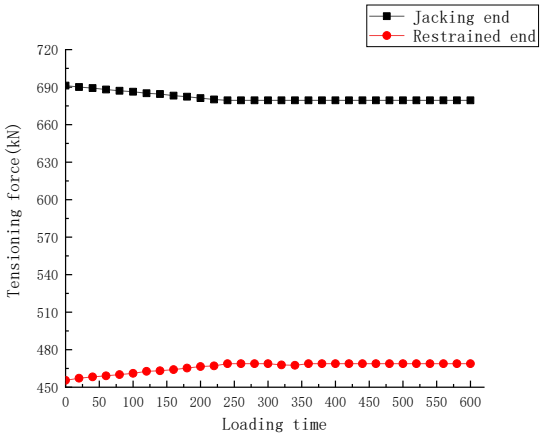

Fig.11 - Relationship curve between load holding time and tension of F1b steel

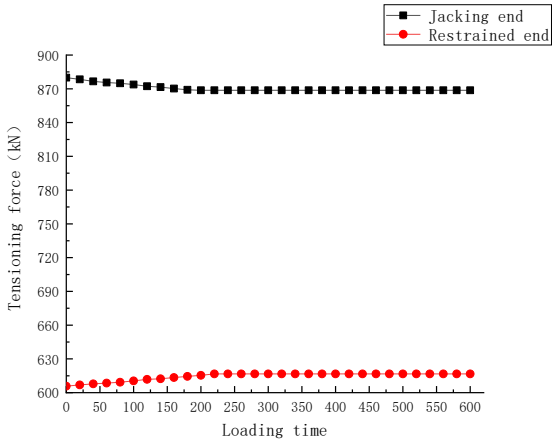

Fig.12 - Relationship curve between load holding time and tension of F3e steel

It can be seen from Figures 11 and 12 that with the increase of loading time, the tensile force of the tension end of the prestressed test steel wires gradually decreases, and the tensile force of the fixed end gradually increases, and the load of the tension end gradually transfers to the fixed end. When the prestressed load is applied at the tension end, the tension speed from the tension end to the fixed end is faster, and the tension of the fixed end increases rapidly. With the increase of loading time, the transfer rate of prestress gradually slows down and finally tends to be stable. It can be seen from the curve diagram of the relationship between the load holding time and the tensile force that the change of the

slope of the image can represent the change of the tensile force at both ends. At the beginning, the slope of the curve is larger and the tensile force at both ends is also larger. Then the slope of the curve gradually decreases and finally tends to zero, and the change speed of tension at both ends also gradually decreases and finally remains unchanged. When the load grade of F1b steel wires is 40 %, the tensile force at both ends reaches a stable time of 240 s. When the load grade of F3e steel wires is 40 %, the tensile force at both ends reaches a stable time of 220 s. Considering the actual construction situation, the loading time is finally set to 5 min.

Channel friction test

Calculation Theory of Duct Friction Loss

According to China's Code for Design of Highway Reinforced Concrete and Prestressed Concrete Bridges and Culverts' (JTG3362 – 2018), among the several factors that cause the prestress loss of bridge structure, the channel friction loss has a great influence on the prestress loss of prestressed concrete continuous beam bridge. The formula of channel friction loss of prestressed concrete continuous beam bridge under post-tensioning tension can be calculated according to the following equation [2]:

It is assumed that the reading of the tension end penetrating pressure sensor is , the reading of the fixed-end pressure sensor is N_2,the calculated length of the prestressed channel is x , the bending angle of the channel is θ :

Formula for calculating friction loss $\sigma_{s1} = \sigma_k[1-e^{-(\mu\theta+kx)}]$, The following formula can be obtained:

$$N_2 = N_1[e^{-(\mu\theta+kx)}] \tag{1}$$

Taking logarithm of equation (1), the following formula can be obtained:

$$\ln(N_1 / N_2) = \mu\theta + kx \tag{2}$$

make $C = \ln(N_1 / N_2)$, then equation (2) is:

$$C = \mu\theta + kx \tag{3}$$

Due to the influence of construction factors, there are errors in the test, Let the test error be ΔF_i then there are:

$$\mu\theta_i + kx_i - C_i = \Delta F_i \tag{4}$$

Using the least squares method, the sum of squares of all prestressed steel bar test errors is:

$$\sum(\Delta F)^2 = \sum(\mu\theta_i + kx_i - C_i)^2 \tag{5}$$

To minimize the test error, so

$$\frac{\partial \sum (\Delta F)^2}{\partial \mu} = 0 \tag{6}$$

$$\frac{\partial \sum (\Delta F)^2}{\partial k} = 0 \tag{7}$$

From equations (5), (6) and (7), the following equations can be obtained:

$$\mu \sum \theta_i^2 + k \sum x_i \theta_i - \sum C_i \theta_i = 0 \tag{8}$$

$$\mu \sum x_i \theta_i + k \sum x_i^2 - \sum C_i x_i = 0 \tag{9}$$

The measured values of friction parameters can be obtained by solving the simultaneous equations (8) and (9) of test data.

Duct friction loss test scheme

In this tunnel friction test, combined with the actual construction situation on site, the longitudinal web prestressed steel bundles F3e and F4h of the first pouring section were selected for tunnel friction test. The detailed parameters of the test bundles are shown in Table 1. In the prestressed tunnel friction test, the through-centre pressure sensor should be installed at both ends of the test bundle, and then the tensioned end and the fixed end should be defined respectively to apply prestressing load to the tensioned end [19].

The results of friction loss test of pore channels

According to the test, the tensile force and elongation of the prestressed test beam F3e and F4h at the tensile end and fixed end of the prestressed steel beam under various loads are measured. The test results are shown in Table 4.

Tab. 4 - Test data of prestressed beam friction test

Steel beam number	Load level	Tensile force of tension end /kN	Fixed end tension/kN	Measured elongation /cm	C_i	
F3e	20%	434.4	309.4	8.5	0.3391	0.3391
	40%	868.7	619.2	16.9	0.3385	
	60%	1303.1	928.2	26.1	0.3393	
	80%	1737.4	1237.0	33.9	0.3397	
	100%	2166.1	1543.6	42.8	0.3388	
F4h	20%	452.9	316.4	8.3	0.3588	0.3591
	40%	905.9	632.7	17.1	0.3589	
	60%	1358.9	948.7	25.9	0.3593	
	80%	1811.8	1264.7	34.1	0.3595	
	100%	2266.2	1582.7	42.7	0.3590	

Substitute the measured data of the prestressed steel bundle friction test into the calculation formulas (8) and (9) to calculate the measured values of the prestressed tunnel friction parameters and are shown in Table 5.

Tab. 5 - Pairs of prestressed drag parameters

Item	Coefficient of friction μ	Deviation factor k
Theoretical design value	0.18	0.0015
Measured value	0.25	0.0028

The friction coefficient of the channel measured by the on-site friction test is 0.25, which is greater than the theoretical design value of 0.18, and the channel deviation coefficient of 0.0028 is also greater than the theoretical design value of 0.0015. There is a certain deviation between the measured value and the theoretical design value. The measured friction parameters can play a guiding role in the design and construction of the bridge type. The tension control force should be adjusted during the formal tension construction. For prestressed tunnels with large bending angles, the friction parameters should be determined through field tests.

ANALYSIS OF CHANNEL FRICTION PARAMETERS

The channel friction parameter has a great influence on the prestress loss of the prestressed concrete continuous girder bridge. In the bridge design, the value of the friction parameter should be comprehensively considered in combination with the actual situation. If the value is too large, the bridge prestress loss estimation is too large, the actual stress applied to the beam is too large, and the bridge structure is too safe, which will damage the prestressed structure or construction material; If the value is too small, the estimated value of the prestress loss of the bridge is too small. The prestress applied to the beam is too small, and the prestress cannot play its performance. During the operation of the bridge, the mid-span deflection and box girder cracking will occur [20].

The finite element simulation model of the whole bridge is established by MIDAS / Civil. The factors such as dead load, prestress tension, sectional construction, temperature effect and construction load are considered in the calculation. The finite element model adopts beam element. According to the control points of bridge construction section and key section, the whole bridge section is divided into 301 nodes and 300 elements. The finite element model of the whole bridge is shown in Figure 13.

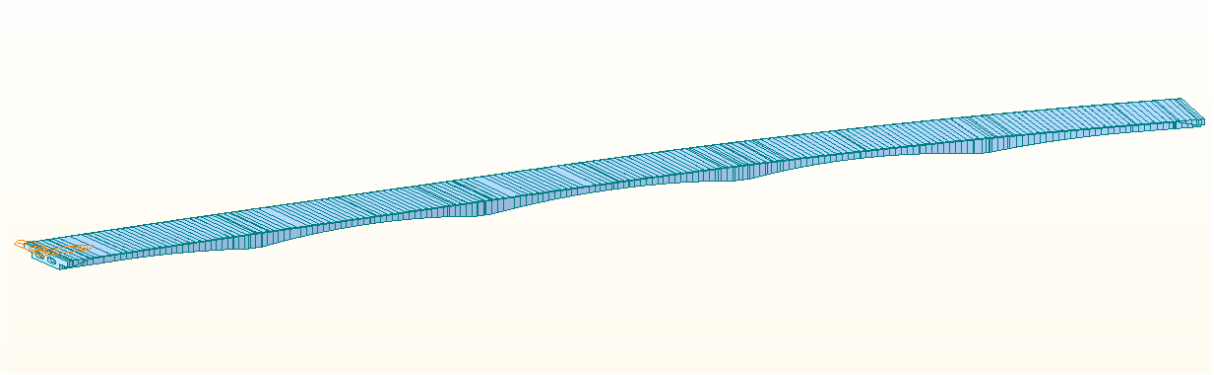

Fig. 13 - Finite element model diagram of the whole bridge

The bridge adopts the molding method of plastic bellows. China's "Code for Design of Highway Reinforced Concrete and Prestressed Concrete Bridges and Culverts" (JTG3362-2018) stipulates that the value of friction coefficient is in the range of 0.15 to 0.20, and the value of deviation coefficient is 0.0015. In this paper, 0.18 is taken, and 0.0015 is taken as the normative design value. The finite element software is used to simulate the influence of different friction coefficients and deviation coefficients on the deflection and stress of the bridge. According to the calculation results, the value of friction parameter has the greatest influence on the deflection and roof stress of the section at L / 2 of the middle span of the bridge. In this paper, the section at L / 2 of the middle span is selected for research and analysis.

Analysis of the effect on the bridge when the friction coefficient is changed alone

The contribution of the value of the prestressed tunnel friction coefficient to the tunnel friction loss cannot be underestimated, and it has a great influence on the overall alignment and stress changes of the bridge structure. Therefore, it is of great significance for the study of prestressed concrete continuous girder bridges to explore the influence of the prestressed tunnel friction coefficient on the deflection and stress of the key sections of the bridge [21]. According to the tunnel friction test results, it can be known that the maximum measured value of the friction coefficient is 0.25, and the tunnel friction coefficients are taken as 0.20, 0.23, 0.26, and 0.29 for this parameter sensitivity analysis. The comparison and analysis results of the influence of the value of the channel friction coefficient on the deflection of the critical section and the roof stress of the prestressed concrete continuous girder bridge and the value of the standard value are as follows:

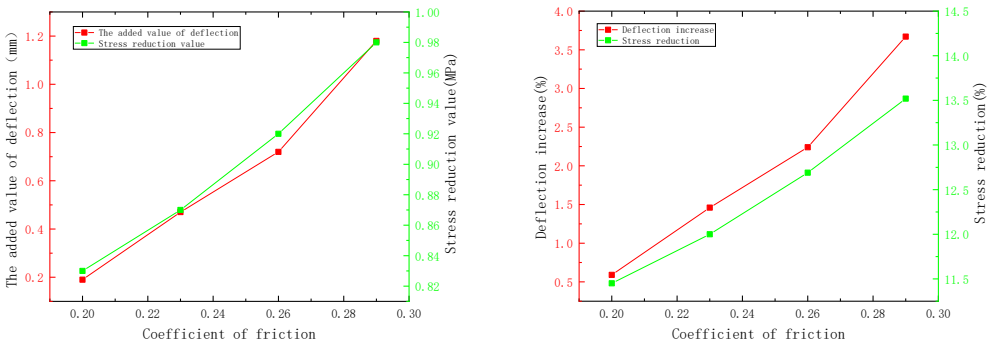

Fig. 14 - Influence of friction coefficient alone on deflection and stress of main beam

It can be seen from Figure 14 that when the friction coefficient of the tunnel is 0.29, the maximum deflection value is 1.18mm, an increase of 3.67% compared with the specification value; the maximum stress change value of the roof is 0.98MPa, a decrease of 13.52% compared with the specification value. When the friction coefficient value of the pipeline increases by 0.02, the deflection increases by 0.78%~1.43% compared with the specification value, and the roof stress value decreases by 0.55%~0.83% compared with the specification value. When the pipe friction coefficient changes alone, the influence on the roof stress of the key section of the prestressed concrete continuous beam bridge is greater than that on the deflection.

Coefficient of deviation Analysis of the effect of individual changes on bridges

The value of the pipe deviation coefficient also has a great influence on the prestress loss of the bridge structure, which in turn affects the deflection and stress of the prestressed concrete continuous girder bridge [22]. According to the results of the tunnel friction test, it can be seen that the maximum measured value of the deviation coefficient of the pipeline is 0.0029. In this parameter sensitivity analysis, the values of the deviation coefficient of the pipeline are 0.0020, 0.0025, 0.0030 and 0.0035 respectively. The influence of numerical variation of deviation coefficient on deflection and roof stress of key section of prestressed concrete continuous beam bridge is compared with the standard value. The results are as follows:

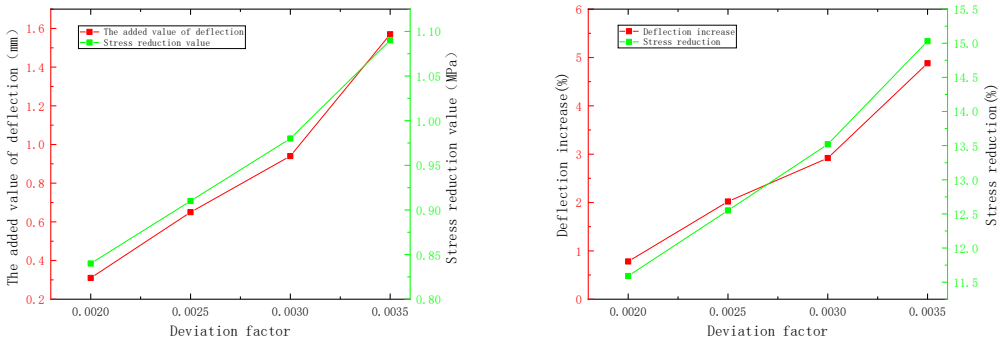

Fig. 15 - Influence diagram of deviation coefficient alone changes on deflection and stress of main beam

It can be seen from Figure 15 that when the deviation coefficient of the pipeline is 0.0035, the maximum deflection value is 1.57mm, which is an increase of 4.88% compared with the specification value; the maximum stress change value of the roof is 1.09MPa, which is 15.03% lower than the specification value. When the deviation coefficient value of the pipeline increases by 0.0005, the deflection increases by 0.9%~1.96% compared with the standard value, and the roof stress decreases by 0.96%~1.51% compared with the standard value. To sum up, it can be seen that the independent change of the pipe deviation coefficient has a greater influence on the deflection and stress of the prestressed concrete continuous girder bridge than the independent change of the pipe friction coefficient.

Analysis of the Influence of Coupling Changes of Friction Coefficient and Deviation Coefficient on Bridges

According to the friction test, the maximum value of the friction parameter is (0.25, 0.0028). In order to study the influence of the coupling change of the friction coefficient and the deviation coefficient on the deflection of the key section of the main beam and the stress of the roof, the friction parameters are respectively (0.20, 0.0020), (0.23, 0.0025), (0.26, 0.0030), (0.29, 0.0035) and the standard values for comparative analysis. The comparative analysis results of the influence of the coupling change of friction coefficient and deviation coefficient on the key section deflection and roof stress of prestressed concrete continuous beam bridge and the standard value are as follows:

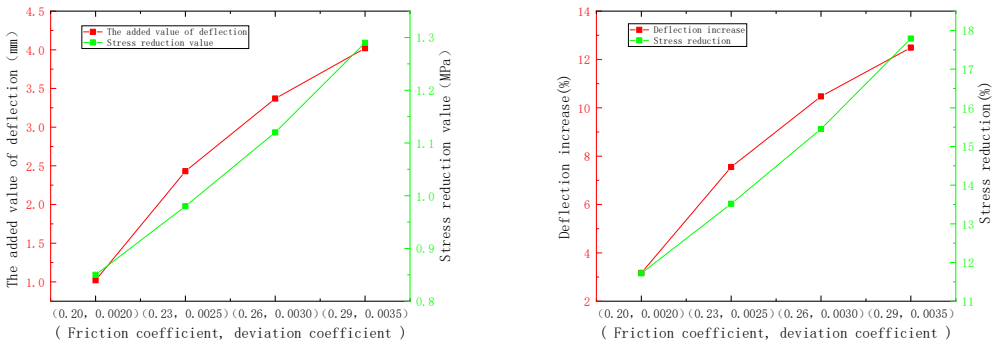

Fig. 16 - Coupling changes of friction coefficient and deviation coefficient on deflection and stress of main beam Influence diagram

It can be seen from Figure 16 that when the value of the channel friction parameter is (0.29, 0.0035), the maximum deflection value is 4.02mm, which is an increase of 12.49% compared with the specification value; 17.79% less than that. When the channel friction parameter increases by (0.03, 0.0005), the deflection increases by 2.02%~4.38% compared with the standard value, and the stress decreases by 1.8%~2.34% compared with the standard value. The influence of the channel friction parameter on the deflection and stress of the main beam when the coupling changes is greater than that when it changes alone.

CONCLUSION

(1) For prestressed steel bundles with a bending angle of not more than 40° and a length of not more than 70 meters, it is recommended that the initial tensile stress be set to 20% of the tension control force, and the load holding time is 5 minutes;

(2) The measured value of friction parameters is greater than the theoretical design value, and there is a certain deviation between the measured value and the theoretical design value. The measured friction parameters can play a guiding role in the design and construction process of this type of bridge. In the formal tension construction, the parameters such as tension control force and holding time should be adjusted.

(3) For the continuous beam bridge with large bending angle and long prestressed tendons, in order to reduce the prestress loss during the tensioning process, the initial tension stress, load holding time and channel friction parameter values should be tested before the formal tensioning construction of prestressed steel tendons.

(4) The value of channel friction parameter has great influence on the deflection and roof stress of the key section of prestressed concrete continuous beam bridge. The deflection of main girder increases with the increase of friction parameters, and the roof stress decreases with the increase of friction parameters. The influence of channel deviation coefficient on the deflection of main beam and roof stress is greater than that of friction coefficient. The influence of the coupling change of the channel friction parameters on the deflection and stress of the main beam is greater than that of the single change.

REFERENCES

[1] Guo Xiaokai,2019. Research on Prestressed Friction Loss of PC Bridge Passage . Hefei University of Technology.
[2] Code for Design of Highway Reinforced Concrete and Prestressed Concrete Bridges and Culverts .People's Communications Press.
[3] Cheng Shoushan, Li Xingqing, Yu Gangqin, et al,2006. Research on Prestress Loss Prediction and Test Method of Prestressed Continuous Girder Bridge. Journal of Highway and Transportation Research Development, vol. 23(4): 71-73.
[4] Zhang Kaiyin, Cao Xuan, Hu Guohai,2019. Research on Contact Stress of Prestressed Concrete Bridge . Journal of Dalian University of Technology, vol. (6) :617-623.
[5] Zhang Kaiyin, Guo Zhiwei, Gu Jinshen,2010.Test and analysis of friction and prestress loss of PC curved duct. Journal of China and Foreign Highway, vol, 30 (4): 145-148.
[6] Lu Pan,2014. Finite Element Analysis and Experimental Study of Prestress Loss.Wuhan University of Technology.
[7] Zhang JINGwei, Wang Feng,2017. Experimental Study on frictional Resistance of prestressed Tunnel of High-speed Railway Shuangyang Bridge. Journal of China Three Gorges University,vol, 39(3): 49-52.
[8] Zhang Qi, Liu Shizhong,2014. Analysis and Research on Friction Loss in Prestressed Continuous Girder Bridges. Journal of Lanzhou Institute of Technology, vol, 21(5): 22-26.
[9] Russo F.M. Wipf T.J. and-Klaiber F.W,2000. Diagnostic load tests of a prestressed con-crete bridge damaged by overheight vehicle impact. Transportation Research Record, vol, 2: 103-110.
[10] Zollman C .Barbaux S.H,1985. Rehabilitation of the boivre viaduet-a multispan prestressed boxgirder bridge. Engineering Structures ,vol. 30:22-47.
[11] E.J.Sapountzakis,J.T.Katsikadelis,2001.Analysisof prestressed concreteslab-and-beamstructures. Computational Mechanics,vol. 27(6):492-503.
[12] Kim, Jeong-Tae, Ryu,2003. Vibration-based method to detect prestress-loss in beam-type bridges. Proceedings of SPIE-The International Society for Optical Engineering, vol. 5(7):559-568.
[13]Kim,Jeong-Tae, Ryu,2007. Monitoring cracks and prestress-loss inPSCgirderbridgesusing vibration-based damagedetection techniques.ProceedingsofSPIE-TheInternationalSociety for Optical Engineering, vol. 6(5):32-35.
[14] Jaturong Sa-nguanmanasak, Taweep Chaisomphob,Eiki Yamaguchi,2006. Stress concentration due to shear lag in continuous box girders. Engineering Structures, vol, 29(7):308-313.
[15] Deng juanhong,2012. Experimental study on friction resistance of posttensioned prestressed concrete box girder . Highway engineering, vol,37(4): 210-214, 220.
[16] JTG/T3650-2020 Technical code for construction of highwaybridges and culverts. People's Communications Press.
[17] Duan Maojun, Wei Yang, etc,2016. Experimental study on tension of 100m super long prestressed tendon . Highway engineering, vol, 41 (3): 31-34, 39
[18] Chen Chengwen, Yu Chengliang, Wang Yongxing,2013.Testand Research on Effective Prestress of Super-long Prestressed Beams. Highway,vol. (1): 144-148.
[19] Liu Zhenzhi,2016.Experimental study on friction resistance of prestressed long duct.Journal of China and Foreign Highway, vol . 36 (3): 207-211
[20] Zhang Wenxue, Xie Quanyi,2015. Sensitivity Analysis of Test Error of Prestressed Tunnel Friction Loss Coefficient for High-speed Railway Bridges. China Railway Science, vol, 36(6): 31-36.
[21] Gong Lei,2016. Prestress loss and sensitivity analysis of long-span prestressed concrete continuous beam bridge .Shijiazhuang Railway University.
[22] Zhao xuman, Zhang Shihui,2011. Study on the influence of prestress loss on the deflection of long-span concrete continuous beam . Railway standard design,vol,06: 80-82.

CIVIL ENGINEERING JOURNAL

Article no. 6

THE CIVIL ENGINEERING JOURNAL Y-20ZZ

CASE STUDY ON THE LARGE DIAMETER PIPE JACKING FOR UTILITY TUNNEL IN MODERATELY WEATHERED SILTSTONE

Yongfeng Li, Guoqiang Liu, Jian Liu, Jing Huang, Fang Tian, Fan Liu

China Construction Third Engineering Bureau Installation Engineering Co.,Ltd, Wuhan, China; ruishan_tan@126.com

ABSTRACT

Pipe jacking has been widely used in utility tunnel constructions as an environment-friendly method in China. This study is focused on the critical technologies used in the pipe jacking for the utility tunnel in Huanggang Mingzhu road. The inner and outer diameters of this utility tunnel are 4m and 4.8m respectively, which is the largest circular pipe jacking project in China at present. This utility tunnel is designed under the urban main road with heavy traffic, so the control accuracy of pipe jacking construction is required to be high. According to the characteristics of the project and actual construction technical measures, the key construction technologies including pipe jacking equipment selection, launching of small spacing, slurry circulating, drag reduction technology, and the control of surface settlement are discussed in this paper. Meanwhile, the jacking force and surface settlement during pipe jacking construction are monitored. The results show that the selected pipe jacking machine has good adaptability to the geological conditions of the project. The actual jacking force is much smaller than the theoretical value, and the two intermediate jacking stations are not activated. In addition, the road surface deformation is -8 – 5mm during the whole process of pipe jacking construction, which has no impact on surface traffic.

KEYWORDS

Large diameter pipe jacking, Utility tunnel, Launching of small spacing, Slurry system, Settlement control

INTRODUCTION

The rapid development of urbanization worldwide and the sharp increase of urban population have brought great pressure on urban environment, surface space and infrastructure The development and utilization of urban underground space is an important way, in which some of problems such as over-concentration of population, environmental pollution, and resource shortage should be solved, moreover, to improve the quality of people's livelihood [1-2]. Pipe jacking is a trenchless method for pipe installation by pushing a prefabricated pipe from the originating shaft to the receiving shaft by a jacking cylinder. Compared to the traditional open cut method, the pipe jacking method has the advantages of fast construction speed, small impact on ground traffic and buildings. So, the pipe jacking is a widely used technology for a wide range within water supply and drainage, electricity, gas, communication, underground passage and other pipeline and tunnel construction projects [3-4].

With the development of pipe jacking technology and the increase of the requirement of the underground space regarding underground engineering, it is inevitable that a larger scale of pipe jacking section is eagerly needed, meanwhile, its construction difficulty also increases greatly. Much debated issues about to be solved concerning the pipe jacking technology focused on calculation and control of jacking force, surface settlement control and technical measures of complex strata. At present, the research on pipe jacking mainly focuses on the pipe and soil interaction, the calculation of frictional resistance and jacking force. Researchers have carried out a lot of research on the above

two points through indoor tests, field tests, numerical simulation and theoretical analysis [5-9]. In addition, some researchers analysed the mechanical properties of the pipe during jacking [10-12]. However, there is little research and summary on the key technologies of pipe jacking construction, especially in complex situations. In fact, these are very valuable for the application and development of pipe jacking.

Based on the pipe jacking for utility tunnel in Huanggang Mingzhu road, this paper summarizes and analyses the difficulties and key technical measures faced in the pipe jacking construction process in the moderately weathered siltstone stratum in the urban area, which provides an excellent reference for the similar projects in the future.

PROJECT PROFILE

The total length of the utility tunnel project is 1302m, starting from Dongmen road, ending at a control centre located on the Mingzhu Road, including a 682m pipe jacking section and a 620m excavation section. The construction area is mainly located below Mingzhu Road, which is in a heavy traffic for seating as a main road (Figure 1). The pipe jacking section is currently the largest diameter circular pipe jacking in China, with its inner and outer diameter of 4m and 4.8m respectively. The prefabricated pipeline was made of C55 concrete with a compressive strength of about 55MPa. Circumferential and longitudinal reinforcements were HRBF500 hot rolled ribbed steel bars fine with a diameter of 12mm and a yield strength greater than 500MPa. The pipe jacking section consists of a launching shaft and two receiving shafts. After completion, the utility tunnel will accommodate four kinds of pipelines, including water supply, communication, 10kV power and 110kV power.

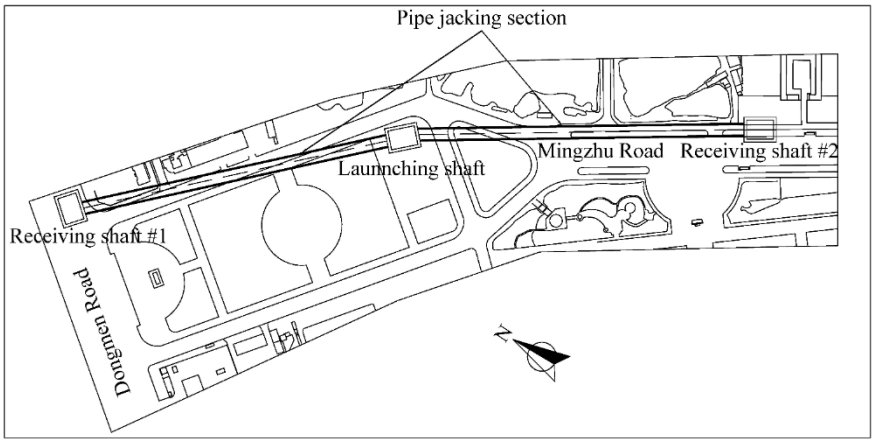

Fig. 1 – The plan and location of pipe jacking

Geological Survey and a Construction Plan have been conducted before construction, the geological profile of pipe jacking construction is shown in Figure 2, the strata from top to bottom are mixed fill, silt clay, strongly weathered siltstone and moderately weathered siltstone. The soil properties are summarized in Table 1. The pipes mainly cross the moderately weathered siltstone. The formation is sand structure, argillaceous cementation, sand content is about 35%, fractures are well developed, rock mass is relatively broken, the maximum uniaxial compressive strength is about 14MPa. Except for the area near the launching shaft, the pipe jacking is located above the groundwater level.

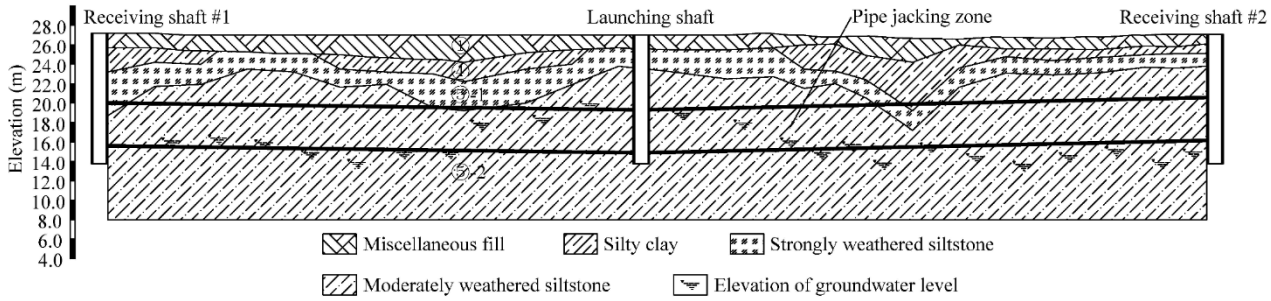

Fig. 2 – Geological profile of pipe jacking

Tab. 1 - Summary of soil properties

layer	soil	Density (g/cm3)	Cohesion (kPa)	Internal friction angle (°)	Compression modulus (MPa)	Saturated uniaxial compressive strength (MPa)
1	Miscellaneous fill	1.75	20	10	-	-
4	Silty clay	1.96	35	16	11	-
5-1	Strongly weathered siltstone	1.95	60	32	45	-
5-2	Moderately weathered siltstone	2.00	150	42	-	9.05

Difficulty analysis

(1) Pipe jacking mainly passes through moderately weathered siltstone stratum, and some areas are located in strongly weathered siltstone and silty clay stratum. Therefore, the pipe jacking machine needs to drill both in soft layer and rock stratum, and have a good slag discharge capacity.
(2) Fractured rock mass makes slurry easy to leak, leading to increased frictional resistance around the pipe. In addition, cuttings deposition due to high leakage of slurry should inevitably influence the jacking efficiency and eventually lead to some serious problems such as pipe stuck.
(3) The construction area is located under the city road and the construction process needs to strictly ensure the road safety.
(4) The distance between the second pipe jacking reaction wall and the portal hole is small, which makes it difficult to launch.

KEY TECHNOLOGIES

Equipment selection

CTPJ4860E-440 slurry balance pipe jacking machine customized by China Railway Engineering Equipment Group Co., Ltd. was adopted for the geological conditions of the project. As shown in Figure 3, the pipe jacking machine adopted spoke and small panel cutter head, and the cutter head was mainly composed of front panel, outer ring beam, bracket and flange the front panel, outer ring beam and bracket were welded with wear-resistant layer to increase the service life of the cutter head. Beside the cutter head was equipped with centre hobs (4), general hobs (15), edge hobs (8), scrapers (32) and edge scrapers (8). The function of tool replacement was realized while ensuring the cutterhead opening rate (32%). To meet the requirement of secondary rock breaking in

small silo space, the displacement shear secondary crushing device was designed by combining the theory of volumetric change crushing, grinding crushing and shear crushing.

Fig. 3 – Pipe jacking machine

Circulating slurry management

The mechanism and requirement of the circulating slurry

(1) Mechanism

The circulating slurry, also known as “mud water”, contributing two features in a pipe jacking process: (1) balancing soil and water pressure on excavation surface; (2) transporting the rock debris. The mud water was pressed into and filled with mud tank through grouting pipe, and mud water penetrated into the soil of excavation surface under pressure, thus forming a layer of impermeable filter cake on excavation surface. On the one hand, the existence of the filter cake can prevent the mud water from continuing to penetrate the soil; on the other hand, the pressure of the mud water acted on the excavation surface through the filter cake, which balanced the water and soil pressure on the excavation surface. At the same time, the cutter head was constantly rotating, and the rock debris cut down was mixed with mud water, which was sent to the mud water separation system through the mud discharge pipe. Through the treatment of mud water separation system, the residue was separated and discharged, and the filtered mud water was returned to the mud water tank for recycling after being stirred by precipitation.

(2) Performance requirement

Before jacking construction, circulating mud should be set according to geological conditions. In clay and silt, on the one hand, with its low permeability coefficient, and the relatively stable soil, which can only rely on water pressure to stabilize the excavation surface. On the other hand, the soil itself generate slurry, so the relative density of mud water is not strict requirements, and even clean water can protect the wall. In sandy soil with low permeability coefficient (K ≤10-3cm/s), mud crust can be formed in a relatively short time, and mud water pressure can effectively control the stability of excavation surface. In the sand soil with moderate permeability coefficient, for 10-3cm/s< K <10-1cm/s, excavation surface instability is easy to occur. During construction in such soil layer, it is necessary to change the performance of mud water to fix it a certain viscosity and density. Stabilizer composed of clay, bentonite and CMC (Carboxymethyl Cellulose) should be added to mud water. In the sand and gravel layer with K >10-1cm/s, due to the small clay content in the soil, the clay content

is constantly reduced in the process of recycling mud water. Therefore, it is necessary to constantly add clay and other stabilizing agents to maintain a high concentration and density of mud water.

Layout for the circulating slurry system

The circulating slurry system in this project was mainly composed of the mud pump, grouting pipe, slurry discharge pipe, mud-water separator, slurry pool and filter press, as shown in Figure 4. The slurry pool was divided into 3 zones, slag pond, primary sedimentation tank and secondary sedimentation tank. The muck cut down from the cutter head was mixed with the circulating slurry, and then transported to the mud-water separator through the slurry discharge pipe. The mud-water separator separated the muck and slurry. After sedimentation and mixing, the treated slurry was transported to the cutter head through the grouting pipe for recycling. In actual construction, the circulating slurry treated by the mud water separator still had high density and viscosity, which reduced the jacking efficiency, so the filter press was added (Figure 5). Filter press is a kind of solid-liquid separation equipment which makes use of special filter medium by applying certain pressure to make liquid dialysis out. The circulating slurry in the primary sedimentation tank was sent to the filter press, which filtered out all the solid particles in the slurry, and the clean water was discharged to the secondary sedimentation tank, and the muck directly fell into the slag pool. Seamless pipe was used in slurry pipeline in this project, which effectively reduced the wear of muck to pipe.

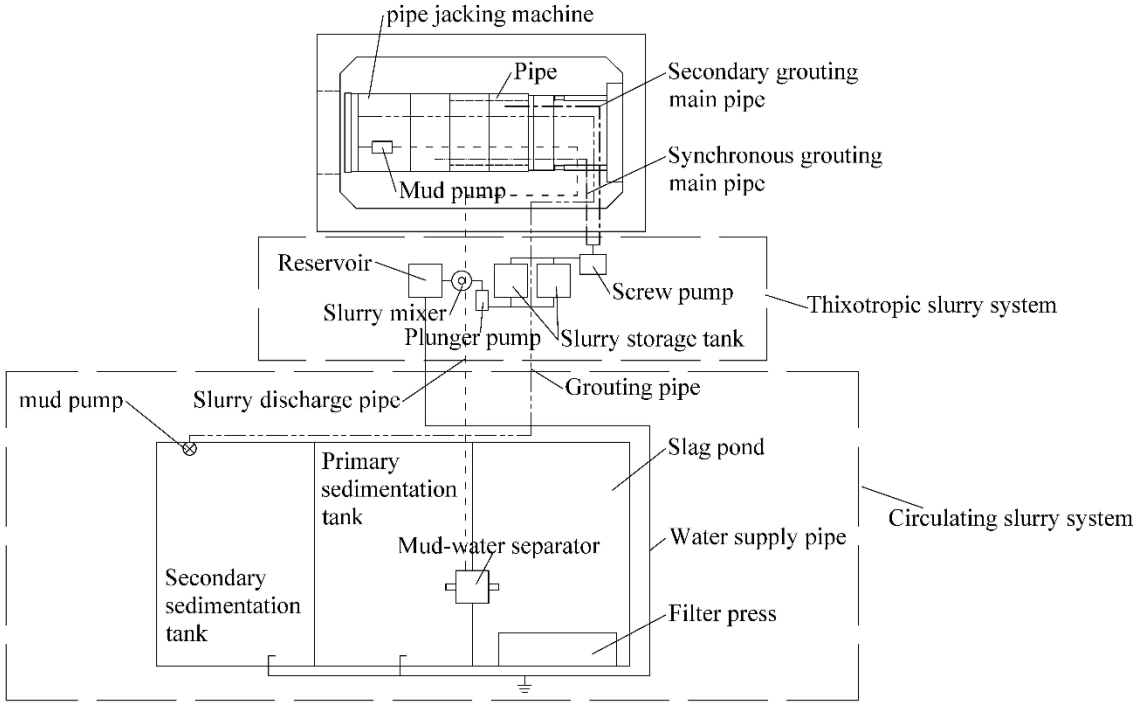

Fig. 4 – Layout of slurry system

Fig. 5 – Slurry separator and press filter

Specific gravity control for circulating slurry

According to field measurement, the maximum specific gravity of the circulating slurry was 1.3~1.4g/cm3, which was far beyond the actual requirements (The requirement specific gravity of slurry in the slurry discharge pipe was 1.2~1.3g/cm3, for the grouting pipe was 1.05~1.1g/cm3), and the muck transportation efficiency was greatly reduced. To control the specific gravity of circulating slurry, the filter press was installed. Due to the limited processing capacity of the filter press, the mud proportion will still rise after a period of time, so the mud needs to be transported out. Through the above measures, the specific gravity of circulating slurry was effectively controlled.

Thixotropic slurry management

Thixotropic slurry system

The thixotropic slurry system of this project was mainly composed of the slurry mixer, slurry storage tank, reservoir, grouting pump and grouting pipe, as shown in Figure 6. The water, bentonite and additives were initially stirred in the slurry mixer (stirring time should be more than 30 minutes), and then pumped to the slurry storage tank for secondary stirring in the mud pump (plunger pump). After full stirring, the thixotropic slurry was pressed to the grouting main pipes through the grouting pump (screw pump). The use of screw pump can make the grouting process without pulsation, at the same time, strong self-priming capacity, stable and uniform grouting pressure was observed. To ensure the continuity of slurry mixing and grouting, two slurry storage tanks with a volume of 7m3 were set up on site.

Fig. 6 – Layout of thixotropic slurry system

To ensure that the outer wall of the pipe can form a good filter cake during jacking construction, two thixotropic slurry main pipes were set up. One was specially used for synchronous

grouting of the tail of pipe jacking machine and adjacent pipes, and the other was used for secondary grouting of other pipes. A grouting section shall be set every interval of one pipe, and each grouting section had 4 grouting holes. The grouting holes were evenly arranged along the socket end of the pipe section, and the grouting holes were connected with the main pipe through branch pipes. The main pipe was made of DN50 steel pipe, the branch pipe was made of DN25 rubber pipe, and a ball valve was set at the connection between each branch pipe and the main pipe. A high-pressure cleaning water pipe was installed in the tube for cleaning the cutter head. Grouting pipe is shown in Figure 7.

Fig. 7 – Layout of grouting pipe

Performance of the thixotropic slurry and application effect

Following aspects should be taken into consideration for the arrangement of the thixotropic slurry process. (1) High viscosity and low filtration loss, so that the slurry can be maintained for a long time; (2) Good thixotropy allows the mud to become gelatinous quickly after injection and support the formation. During pipe jacking process, the slurry and the pipes moved relatively, the slurry shear force decreases, which reduced the frictional resistance; (3) Maintain good stability, so that the slurry will not lose stability due to groundwater intrusion and prolonged construction.

For the properties of the main crossing area, little impact concerning the ground-water, and to improve the efficiency of muck, the thixotropic slurry used on site should havee high viscosity and low water loss. The thixotropic slurry was mainly composed of compound bentonite (sodium bentonite mixed with additives) and water, with the ratio of 1:10 for bentonite and water. In the early stage of construction from the launching shaft to the receiving shaft #1, a certain amount of chemical mud powder was added to the thixotropic slurry. The chemical mud powder mainly played the role of flocculation and viscosity increase. Because the composite bentonite used already contained relevant additives, the additional chemical mud powder made the flocculation degree of the thixotropic slurry increase and the performance become worse. After stopping the chemical mud powder, the performance of thixotropic mud was improved. The properties of thixotropic slurry are shown in Table 2.

Tab. 2 - Performance for the thixotropic slurry

Number	Density (g/cm3)	Marsh funnel viscosity (s)	Filter loss (0.5h)	Bleeding rate (24h)	Remark
1	1.06	70	76	15%	With chemical mud powder
2	1.065	112	20	0	Without chemical mud powder
3	1.06	90	22	0	

Figure 8 shows the calculation results of the frictional resistance per unit area based on the measured jacking force. In the initial jacking stage, the unit frictional resistance was very large. On the one hand, the lubrication was not carried out at this time, on the other hand, the face resistance

was large when the pipe jacking machine passed through the reinforcement area. In the calculation of the unit frictional resistance, the face resistance was calculated according to the pressure of the mud tank, which was less than the actual value. After grouting, with the increase of jacking distance, the lubrication performance of the slurry was better developed, and the unit frictional resistance was rapidly reduced and tended to be stable. In the first section, the unit frictional resistance was stable at about 3 kPa, and in the second section, the unit frictional resistance was about 2.5kPa. In Technical Specification for Pipe Jacking of Water Supply and Drainage Engineering (CECS246:2008) [13], there is no explanation for moderately weathered siltstone. If the jacking force is calculated according to fine silt and medium-coarse sand, the unit frictional resistance is more than 8kPa, far higher than the actual value.

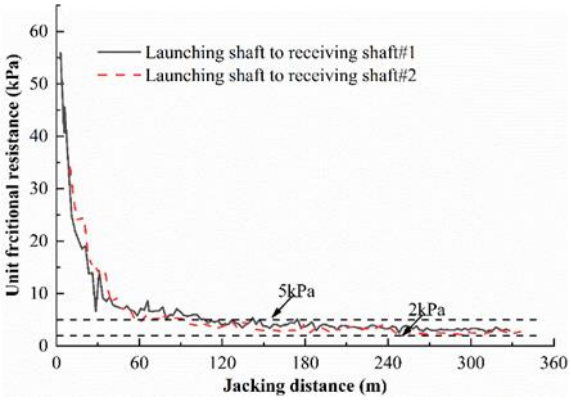

Fig. 8 – Unit area friction resistance curve

Small spacing launching technology

Due to the angle between the axis of the first jacking pipe section and the axis of the second jacking pipe section was about 12°, and the axis of the previous section was perpendicular to the wall of the launching shaft. So, the reaction wall of the second jacking pipe section was close to the hole door (the spacing is about 7.5m) to meet the deflection angle, and the operating space was narrow, as shown in Figure 9. The reaction wall was made up of rear cushion iron, H-shaped steel support and concrete. The reaction wall was made of C35 concrete with a compressive strength of about 35MPa.Two 5m-long 400×400×13×21HW steel sections were embedded in the concrete of the bottom plate and welded with the rear cushion iron. moreover, In addition, 8 pieces of 400×400×13×21HW steel were used as diagonal braces, which were welded to the backrest and fixed to the foundation by bolts. It is worth noting that 400 x 400 x 13 x 21 HW indicates a section with a height and width of 400 mm, a web thickness of 13 mm and a flange thickness of 21 mm. To enhance the stability of the rear backrest, concrete blocks were poured in the rear part, and steel diagonal supports were buried in it. The rear backrest design is shown in Figure 10.

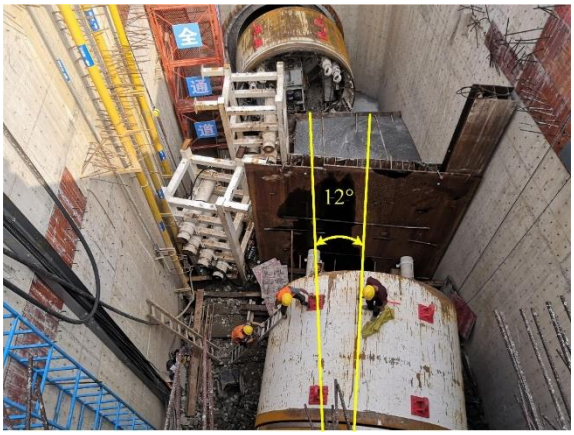

Fig. 9 – Launching of small spacing

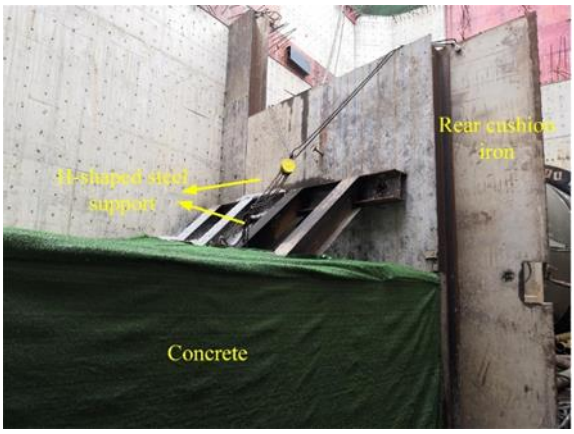

Fig. 10 – Reaction wall

Due to the narrow origination space, it is impossible to carry out jacking after assembling the pipe jacking machine. Firstly, the front shield of the pipe jacking machine was hoisted into the initial guide rail, and its top was pushed to the hole door (not into the reinforcement area) through the two main oil jacking cylinders. Then, the tail shield was hoisted into the tail shield, and the front shield and tail shield were connected and fixed, and the circulating slurry pipelines were connected. After the pipe jacking machine was jacked for a certain distance, it started to jack the pipes. Before jacking the third pipe, install all the jacking cylinders and start normal jacking. The implementation steps are shown in Figure 11.

(a) Front shield jacking *(b) Front shield and tail shield splicing*

(c) Pipe jacking *(d) Installation of main jacking cylinder frame*

Fig. 11 – Launching step of pipe jacking

Control of the surface settlement

Control measures

(1) Jacking speed control

In the pipe jacking process, if the excavation surface is severely squeezed, the soil will be greatly deformed, and the surface in front of the drilling face may heave. During the jacking process, it is necessary to combine the axis deviation, grouting speed, jacking force and other factors to adjust the jacking speed in real time to ensure the stability of the jacking construction. In this project, the jacking speed was controlled at 10~20mm/min during the launching, and 20~30mm/min during the normal jacking.

(2) Pressure control in the mud tank

When the pressure of the mud tank is too large, the soil in front will be uplifted and deformed, otherwise the settlement deformation will occur. During the construction, the pressure of the mud tank can be measured by the pressure sensor in the pipe jacking machine. In this project, the pressure of mud tank was controlled at 0.01~0.015 MPa.

(3) Grouting control

A principle for grouting should be follow as "press first and then push, follow the push with pressure, and fill the slurry in time" to ensure the timely formation of a complete mud sleeve. In synchronous grouting, screw pump with stable pressure was selected for grouting to ensure the pressure of thixotropic slurry was stable and accurate when pressing into the stratum, and to prevent thixotropic mud from penetrating the stratum. The slurry pressure sensor was installed in the grouting hole at the tail of the pipe jacking machine to ensure the accurate control of the grouting pressure (the grouting pressure is controlled at about 0.3MPa). Secondary grouting mainly plays a role in ensuring the integrity of thixotropic slurry sleeve and supplementing the formation loss. The amount of grouting can be determined according to the pipe jacking thrust, formation parameters, mud performance, surface settlement and other parameters, generally 0.2~0.3 times of synchronous grouting amount. In this project, 2~3 times of secondary grouting were carried out every day, and each time of grouting was about 5 minutes.

(4) Jacking attitude control

In the process of pipe jacking, it is necessary to adjust and control the jacking orientation. If the deviation of the pipe jacking axis is too large, overcutting or undercutting will occur, which will cause the loss of the stratum around the pipe or the change of soil pressure.

(5) Displace grouting

After pipe jacking is completed, displacement grouting is needed to prevent settlement caused by water loss of thixotropic slurry. In the process of grouting, cement grout was observed to flow out of the grouting hole at the top, that is, displace grouting was completed. In the process of grouting, special attention should be paid to prevent the replacement grout from damaging the existing surrounding buildings by monitoring the channels and the formation cracks.

Monitoring and analysis of ground deformation

The layout of surface settlement measuring points is shown in Figure12. Since it cannot be drilled through the road surface, the settlement measuring points are arranged with steel nails. The first pipe jacking section was arranged with 21 settlement monitoring sections, a total of 85 settlement monitoring points, and the distance between each section is 10m (extended when the terrain is limited). Among them, monitoring sections No.6 and No.18 were strengthened monitoring sections, and each section had 17 settlement monitoring points. The second pipe jacking section was arranged in the second section of the pipe jacking, with a total of 72 subsidence monitoring

points, of which the No. 3 section was a strengthened monitoring section, including 15 measuring points.

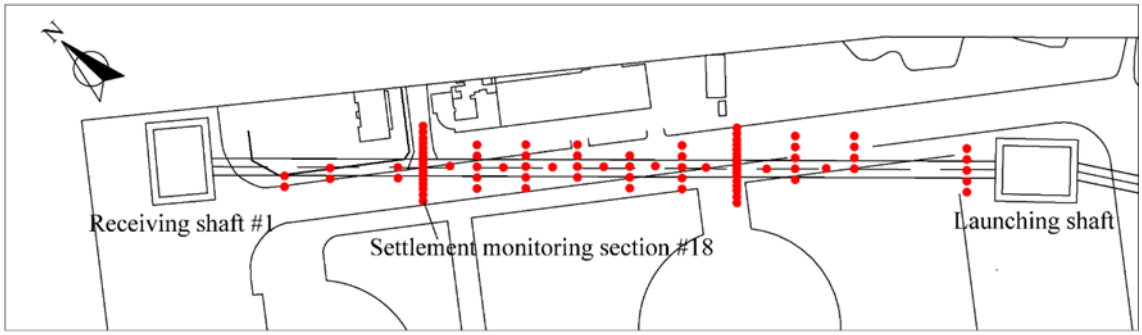

(a) The first pipe jacking section

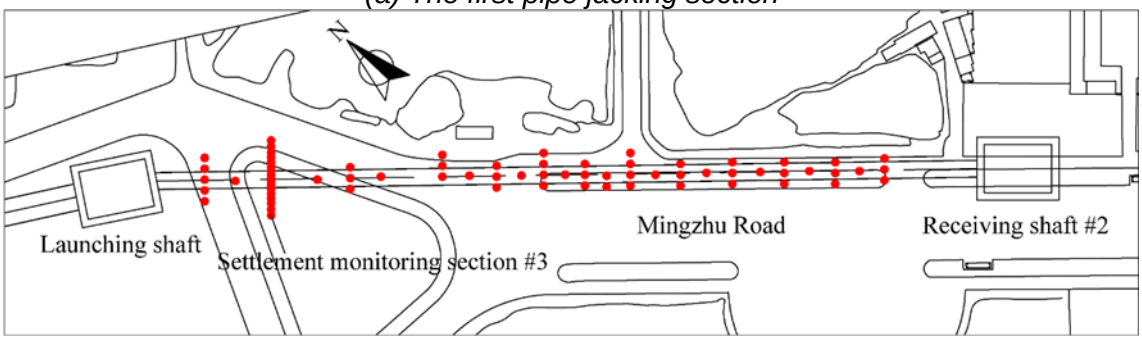

(b) The second pipe jacking section.

Fig. 12 – Layout of the monitoring points

The ground deformation of the monitoring section 18 of the first pipe jacking section is shown in Figure 13. In the figure, -27m – +19m represented the distance from the pipe jacking machine to the monitoring section, -27m represented that the pipe jacking machine still has 27m to the monitoring section, and +19m represented that the pipe jacking machine passes through the section for 19m. Since the settlement measuring point did not penetrate the road surface, the measured settlement change was different from the actual stratum settlement, and it did not appear in the form of a settlement tank. During the process of the pipe jacking machine passing through the section, the overall settlement of the section changes to uplifted first (or settlement decrease), and then settled (or settlement increase). The left side of the monitoring section was mainly the roadway, which had large settlement due to the influence of vehicle load, while the right side was the sidewalk, and the ground deformation showed the decrease of uplift. The reason may be that the measuring nails sprang back after measuring the initial value of the settlement point.

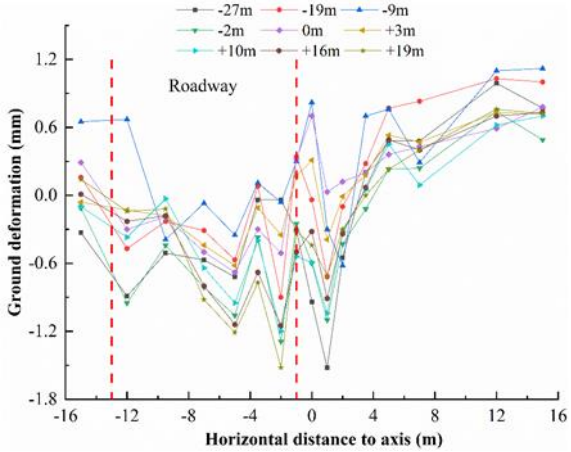

Fig. 13 – Ground deformation of monitoring section 18

Figure 14 illustrates the ground deformation of the monitoring section 3 of the second pipe jacking section. The 12 measuring points of this monitoring section were located in the soil, and 3 were located on the sidewalk. When the pipe jacking machine was close to the monitoring section, the monitoring section had a certain uplift. After the pipe jacking machine passed through the monitoring section, the settlement first increased rapidly and then tended to be stable. In the soil layer, the settlement of the area near the pipe jacking axis was large, while the deformation of the measuring point on the sidewalk was basically the same.

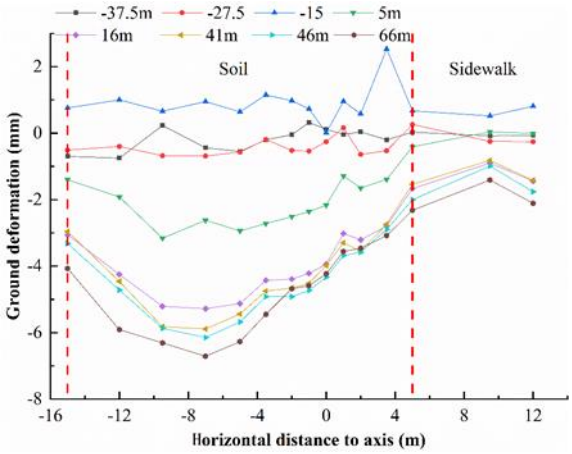

Fig. 14 – Ground deformation of monitoring section 3

According to the monitoring results, in the whole process of pipe jacking construction, the ground deformation was -8 ~ 5mm, and the settlement control of pipe jacking construction has achieved good results.

CONCLUSION AND DISCUSSION

In this investigation, the aim was to analyse several possible difficulties in an unfavourable stratum pipe jacking project, and propose some practicable solutions to those existing issues (equipment selection, small interval launching, management of recycling slurry, resistance reduction by grouting) on perspective of a practical pipe jacking engineering application conducted in Huang Gang, to be specifically:

(1) The slurry balanced pipe jacking machine and cutter head used in this project had good adaptability to the fractured moderately weathered siltstone stratum, and it had high construction efficiency in weathered rock stratum and rock-soil composite layer.
(2) The specific gravity of circulating slurry had great influence on jacking efficiency. When the specific gravity was too high, the rock debris cut by the cutter head cannot be discharged smoothly, resulting in a reduction in the jacking speed or even failure to jacking. On the contrary, if the specific gravity was too low, the rock debris cannot be carried. In this project, the specific gravity of circulating slurry was better controlled by adding filter press and timely transporting mud, but it also had a certain impact on the construction efficiency.
(3) The performance of thixotropic slurry has a direct impact on its drag reduction effect. When the thixotropic slurry has a high-water loss and water separation rate, a good filter cake cannot be formed around the pipe. After stopping grouting, the slurry will leak out quickly, increasing the frictional resistance. Therefore, the performance of thixotropic slurry should be monitored on site and adjusted in time when the slurry performance decreased.
(4) The small spacing pipe jacking launching technology adopted in this project effectively solved the problem of narrow launching space, enabling the pipe jacking machine to launch smoothly, and has no impact on subsequent construction.

(5) By controlling the jacking rate, slurry chamber pressure, grouting pressure, grouting amount, the volume of excavated earth and other construction parameters, the road surface deformation is controlled within -8~5mm, and the surface traffic is not affected.

ACKNOWLEDGEMENTS

This work is supported by China Construction Third Engineering Bureau Installation Engineering Co., Ltd.

REFERENCES

[1] Broere, W., 2016. Urban underground space: Solving the problems of today's cities. Tunnelling and Underground Space Technology, vol. 55: 245-248.
[2] Hunt, D.V.L., Makana, L.O., Jefferson, I., Rogers, C.D.F., 2016. Liveable cities and urban underground space. Tunnelling and Underground Space Technology, vol. 55: 8-20.
[3] Ma, B.S., Najafi, M., 2008. Development and applications of trenchless technology in China. Tunnelling and Underground Space Technology, vol. 23, no. 4: 476-480.
[4] Bergeson, W., 2014. Review of long drive microtunneling technology for use on large scale projects. Tunnelling and Underground Space Technology, vol. 39: 66-72.
[5] Staheli, K., 2006. Jacking force prediction: An interface friction approach based on pipe surface roughness. Ph.D. thesis, Georgia Institute of Technology, Atlanta, US.
[6] Reilly, C.C., Orr, T.L., 2017. Physical modelling of the effect of lubricants in pipe jacking. Tunnelling and Underground Space Technology, vol. 63: 44-53.
[7] Pellet-Beaucour, A. L., Kastner, R., 2002. Experimental and analytical study of friction forces during microtunneling operations. Tunnelling and Underground Space Technology, vol. 17: 83-97.
[8] Yen, J., Shou, K., 2015. Numerical simulation for the estimation the jacking force of pipe jacking. Tunnelling and Underground Space Technology,vol. 49: 218-229.
[9] Zhang, P., Behbahani, S.S., Ma, B.S., Iseley, T., Tan, L.X., 2018. A jacking force study of curved steel pipe roof in Gongbei tunnel: calculation review and monitoring data analysis. Tunnelling and Underground Space Technology, vol. 72: 305-322.
[10] Norris, P., 1992. The behavior of jacked concrete pipes during site installation. Ph.D. thesis, University of Oxford, Oxford, UK.
[11] Cui, Q.L., Xu, Y.S., Shen, S.L, Yin, Z.Y., Horpibulsuk, S., 2015. Field performance of concrete pipes during jacking in cemented sandy silt. Tunnelling and Underground Space Technology, vol. 49: 336–344.
[12] Li, C., Zhong, Z.L., Bie, C.Y., Liu, X.R., 2018. Field performance of large section concrete pipes cracking during jacking in Chongqing – A case study. Tunnelling and Underground Space Technology. vol. 82: 568-583.
[13] CECS, 2008. Technical specification for pipe jacking of water supply and sew-erage engineering. China Planning Press, Beijing.

CIVIL ENGINEERING JOURNAL

Article no. 7

THE CIVIL ENGINEERING JOURNAL 1-2023

EXPERIMENTAL INVESTIGATION OF EFFECT OF PERVIOUS CONCRETE ON RIGID PAVEMENT IN PAKISTAN

Madiha Shamim, Hira Shakeel and Shafaq Naseer

Sir Syed University of Engineering & Technology, Faculty of Civil Engineering Department, ST-16 Main University Road, block 5 Gulshan-e-Iqbal, Karachi, Pakistan; mshamim@ssuet.edu.pk, hshakeel@ssuet.edu.pk, snaseer@ssuet.edu.pk

ABSTRACT

Pakistan is facing adverse environmental issues peculiarly in major cities. The condition gets worst during monsoon period when the whole city faces the urban flooding due to stagnation of storm water on all major streets and areas. The main reason is the lack of infrastructure to mitigate the crisis which is faced by the country during whole rainfall season. The introduction of Pervious Concrete in major pavement infrastructure can easily limit the problems of sump of rain water. As a part of road infrastructure, the upper layer of pavement can be pervious, making runoff water to move to sub-base. This paper offers the exploratory research to ascertain the compressive strengths and infiltration rate of different samples of Porous Concrete following the American Concrete Institute guidelines. The experiments were done with varying the properties of Pervious Concrete. The effects which were considered are curing time, mix proportion, percentage quantity of fine aggregate, ratio of water to cement and varying coarse aggregate size. The mix design ratio considered were 1:4, 1:5 and 1:6. For further experiment of infiltration rate, the custom slab was formed with dimensions 2'x1'x4" and was tested for all the desired ratios. For the purpose of cost comparison, a fixed size on land is kept as standard. The cost is compared for construction on the land, using three different materials: Pervious concrete, Traditional concrete and Asphalt premix. It was showed that the Traditional concrete is cheaper than the Pervious and Asphalt layer but Pervious concrete is also economical than Asphalt layer.

KEYWORDS

Infrastructure, Pervious concrete, Compressive strength, Infiltration rate, Mix design, Asphalt premix, Traditional concrete

INTRODUCTION

One of the main engineering systems for the transportation and drainage of urban sewage and rainwater is the drainage system of every given city. The primary system for defending the city against flood damage and water logging, which can result in unanticipated loss and hardship. In the US, the use of Portland cement pervious concrete is rising in parking lots and sidewalks due to the fact that it provides benefits in reducing rainwater runoff and improve water quality [1]. "Porous Concrete is made of cement, water, coarse aggregate, and little to no fine aggregate is known as "pervious concrete." Because of its special benefits like a road drainage system, a reduction in tyre and pavement noise, skid resistance, recharging of underground water, reducing storm water runoff, and limiting the pollutants to enter the groundwater, pervious concrete pavement has been used extensively throughout the world. All of these benefits are made possible by its open pore structure, which is primarily the connected porosity and larger size of pores [2, 3]. It depends on the design that the concrete pavement that drains and its sub base material may have ample storage capacity for water so that a swale is not needed. During rainy days the pavement is free from splash on

surface and slipping, hence improving the safety. [4, 5]. The durability and permeability characteristics of permeable concrete is of prime importance. Due to unique features, pervious concrete may require special testing procedures also like compaction and consolidation. It is investigated compressive strength of pervious concrete with the relationship of different properties like water cement ration, aggregate cement ratio, aggregate size, quantity of admixture and compaction. The correlation was obtained to determine the porosity of pervious concrete so as to design the PC mixtures [6-9]. PC generally own high permeability and low compressive strength which can be enhanced by the addition of several cementitious materials and/or admixtures. The ordinary Portland cement acts as main binder and cementitious materials like fly ash, blast furnace slag and silica fume and water reducing admixtures can be used with Portland cement. Study [10] showed that the compressive strength can be improved 9-15% with use of super-plasticizer as to reduce w/c ratio. 6:1, 8:1, and 10:1 aggregate to cement ratios were employed in batches with aggregate sizes of 18.75mm and 9.375mm. The 6:1 ratio gave high compressive strength whereas 10:1 gave high permeability as a result [10-13]. Another studies [14-16] carried three methods of compaction (self-consolidating, half rodded, and standard proctor hammer). The most compressive strength was obtained using the traditional proctor hammer method whereas the samples of self-consolidating method gave the high infiltration rate thus found more pervious [14-16]. Studies [18] illustrates that the angularity number, Latex and fibre additions have an impact on the qualities as well and behaviour of pervious concrete in the way that Compressive strength, flexural strength, and split tensile strength all rise as fine aggregate volume decreases, which is caused by an increase in fine aggregate. However, PC's split tensile strength was the only thing that latex and fibre enhanced [17-20]. The aim of the research is to introduce the pervious concrete in urban infrastructure of Pakistan where there is severe urban flooding during the whole rainy season hence rain water remains on surface of pavement for many days. In this regard the objective of the study is to make possible provision of pervious concrete through sewage drain slabs, on sides of main highways and roads, walkways, parking lots and as a part of pavement. Moreover, the study is limited to compressive strength and infiltration rate tests of the pervious concrete without addition of any admixtures.

METHODS

Materials

The materials used for Pervious Concrete was Ordinary Portland Cement (locally available OPC 53 Grade cement with more compressive strength), Coarse aggregate (passing #4 sieve) which were available locally. The size of aggregate used for casting was limited to 20mm, not larger than 20mm and not smaller than 10mm. Mix design ratios were calculated for each trial batch. It included the required amount of Coarse aggregate, Cement and water for each sample of pervious concrete prepared in lab. Trial batches were conducted following the American Concrete Institute (ACI) guidelines ACI 522R-10 [10].

Preparation of testing samples:

For sample preparation the cylinder taken was 6-inch diameter with 12-inch height. The density of pervious concrete was considered as 125 lb/cu.ft. Hence for total volume of 0.196 cu.ft, the total mass of concrete including 15% wastage was found to be 12.783 kg. Therefore, the mix proportion for all mix ratios is shown in Table 1.

MIX RATIO	CEMENT (kg)	COARSE AGGREGATE (kg)
1:4	2.55	10.22
1:5	2.13	10.65
1:6	1.82	10.95

The five trial batches were prepared with varying curing period, mix design ratio, water to cement ratio, percentage of fine aggregate content and the size of coarse aggregate to investigate the compressive strength as shown in Figure 1. The trial batch made with varying mix design was prepared with ratios 1:4, 1:5, and 1:6. On the other hand, all the other trial batches were composed with design ratio of 1:4. The first trial batch was comprised of three cylinder samples with by varying only the curing period for which casted cylinders were kept submerged for the purpose of attaining prospective compressive strength as shown in Figure 2. To have uniformity in each trial, three cylinders were casted, each having the same constituents as the rest. This pertains to have uniform W/C ratio for all, same cement, aggregate size and shape. The primary difference to be maintained was of curing i.e. 7, 14 and 28 days. The second trial batch was comprised of samples with varying concrete mix design ratios i.e. 1:4, 1:5 and 1:6.

Third round of trial batches were conducted by varying the water to cement ratio with w/c ratios 0.25, 0.35 and 0.45 respectively with 28 days curing. The small percentage of the fine aggregate was added for the fourth trial batch. Three cylinders with 4%, 8% and 12% of fine aggregate were casted. The fifth and last trial batch was done with varying size of coarse aggregate while keeping the other factors constant i.e. mix design ratio as 1:4, w/c ratio was 0.4 and curing period of 28 days. The coarse aggregate size range selected were 19.5mm - 12.5mm and 12.5mm-9.55mm. For the size range 19.5mm-12.5mm, material passing through the sieve of ¾” and retaining on sieve of ½” was selected, whereas for size range 12.5mm-9.55mm, the material passing through the sieve ½” and retaining on the sieve 3/8” was selected.

Fig. 1 – Preparation of Trial Batch

Fig. 2 – Cylinder Samples for Testing

After conduction of trial batches of cylinders were completed, the slabs were constructed in order to experiment for Infiltration Rate. The design ratios on which slab was to be constructed were 1:4, 1:5 and 1:6 with 28 days curing period. For slab, a custom mould was made having dimensions 2' x 1' x 4" as shown in Figure 3. The size was selected by keeping in view the easiness of work with and at the same time if fulfilled the purpose to test the infiltration rate. Curing of slab was done by using jute bags. Wet jute bags were placed on slab samples making sure to dip the jute bag in water and place on slab again as shown in Figure 4.

Fig. 3 – Slab placed in its Custom Wooden Mould

Fig. 4 – Curing of Slab using Jute bags

Compressive strength and infiltration rate tests:

The cylinders were tested for compressive strength so that an idea for the compressive strength of Pervious Concrete could be established. The testing was conducted on Compression Testing Machine.

The casted slab samples were tested for infiltration rate keeping water to cement ratio constant with varying Concrete mix design. The slab samples had mix design ratio of 1:4, 1:5 and 1:6 for which the Infiltration rate was calculated. The ASTM C1701 standard test method for determining the infiltration rate of pervious concrete was used to measure the infiltration rate. The experimental setup requires an infiltration ring, a five-litre container of water, plumber's putty, water and a stop watch. Two lines should be marked on the inner surface of the infiltration ring at intervals of 4 inches and 6 inches respectively as shown in Figure 5. The infiltration ring should be placed at a clean pervious concrete pavement, after placing the ring on the pavement/slab plumbers' putty was placed so that the ring gets fixed and a water tight seal is created. Start pouring water at a steady rate so that the water level does not rise above the lines marked on the inner surface of the ring and start timing. After following these steps, we can calculate the infiltration rate easily by using the equation 1.

$$I = K\,M / D2\,t \quad (1)$$

I = Infiltration rate (in/min)

M = Mass of water absorbed/infiltrated (lbs)

D2 = Square of Inner diameter of infiltration ring (inch)

t = Time the amount of water to infiltrate the pervious concrete (sec)

K = 126870 (in3. s/ kg.min)

Fig. 5- Infiltration Rate Setup

Fig. 6 – Pervious Concrete Slab

Cost Comparison of traditional and Pervious concrete shown in Figure 6, was done. For the purpose of comparison, a fixed size on land is kept as standard. The cost is compared for construction on this land, using three different materials:

- Pervious concrete
- Traditional concrete
- Asphalt premix

A size of land measuring 100 feet long and 3 feet wide is selected for cost comparison. The cost will be calculated only for the top surface of construction. Whether the road or construction employs pervious concrete, normal concrete or asphalt premix, each of these have a sub-base layer beneath them. However, the cost of this sub-base is not calculated. The current rates of that time were

considered for cost comparison of materials. The revealed comparison that conventional concrete is less expensive than that of pervious and asphalt layer but pervious concrete is also more cost effective than asphalt layer. In general, initial costs for pervious concrete pavements are more than that for traditional concrete or asphalt paving. But the complete costs can be substantially lower.

RESULTS AND DISCUSSIONS

Results:

Compressive strength values for all the five trials batches with different properties is summarized below in Table 2. Each batch consist of three samples making it total of fourteen samples for compressive strengths and total three slab samples for infiltration test. However poorly casted or samples with defects were discarded and did not consider for results.

Tab. 2 - Summary of Trial batches with corresponding Compressive Strengths

Batch	Concrete Mix Design	W/C Ratio	Fine Aggregate (%)	Curing period	Compressive Strength (psi)
Batch 1: Varying curing period					
1	1:4	0.4	0%	7	1415
1	1:4	0.4	0%	14	1503
1	1:4	0.4	0%	28	1627
Batch 2: Varying mix design ratio					
2	1:4	0.4	0%	28	1556
2	1:5	0.4	0%	28	1149
2	1:6	0.4	0%	28	884
Batch 3: Varying W/c ratio					
3	1:4	0.25	0%	28	1644
3	1:4	0.35	0%	28	1591
3	1:4	0.45	0%	28	1538
Batch 4: Varying amount of fine aggregate					
4	1:4	0.4	4%	28	1574
4	1:4	0.4	8%	28	1645
4	1:4	0.4	12%	28	1698
Batch 5: Varying size of coarse aggregate					
5	1:4 (20-12.5mm)	0.4	0%	28	1556
5	1:4 (12.5-9.5mm)	0.4	0%	28	1715

The graphical representations of relationship of each parameter and compressive strength is shown below.

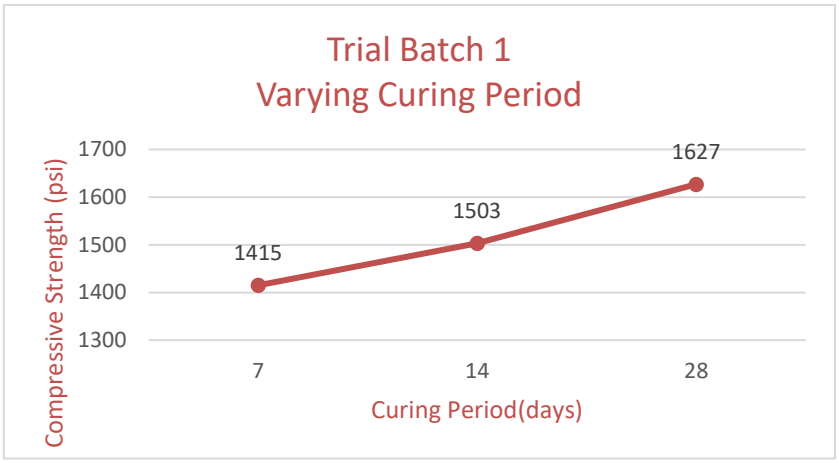

Fig. 7 – Graph between Curing Period and Compressive Strength

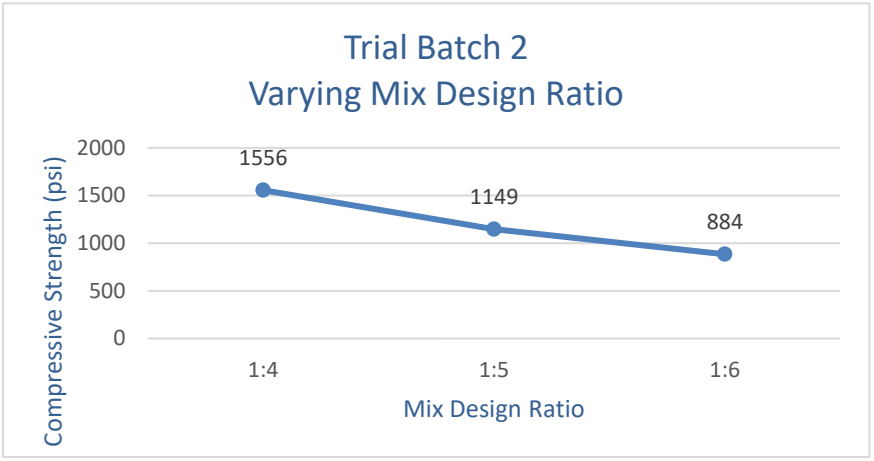

Fig. 8 – Compressive Strength and Mix Design Ratio

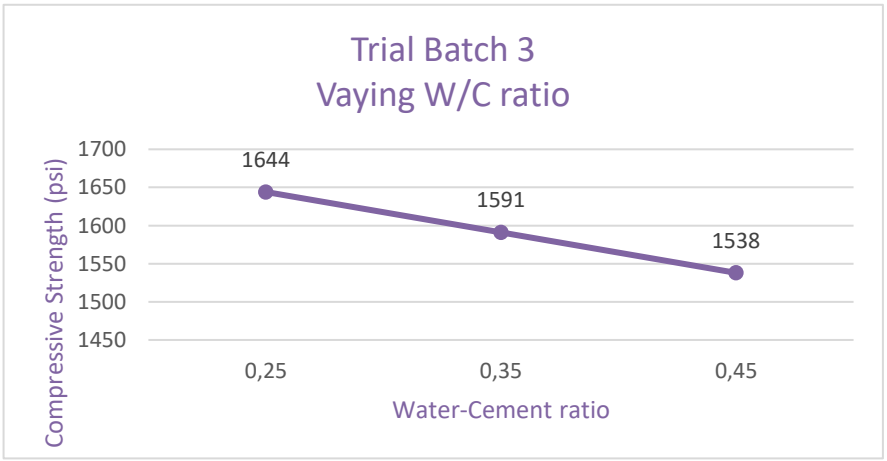

Fig. 9 – Compressive Strength and water-cement ratio

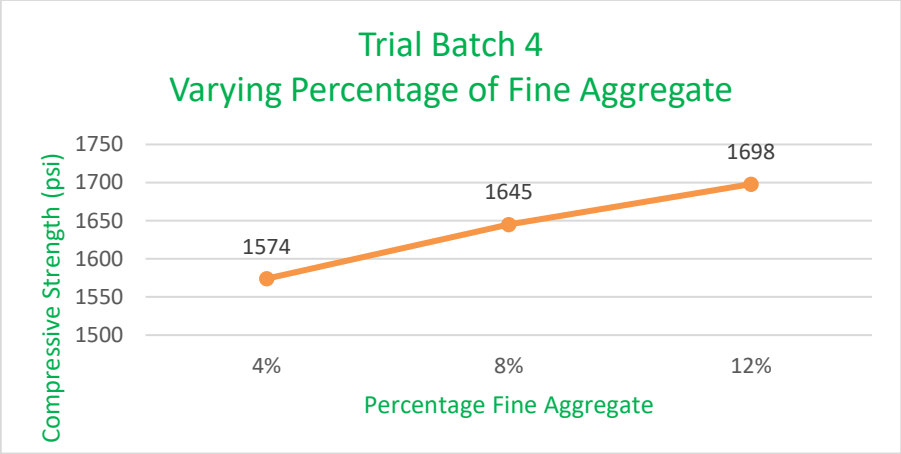

Fig. 10 – Compressive Strength and Percentage Fine Aggregate

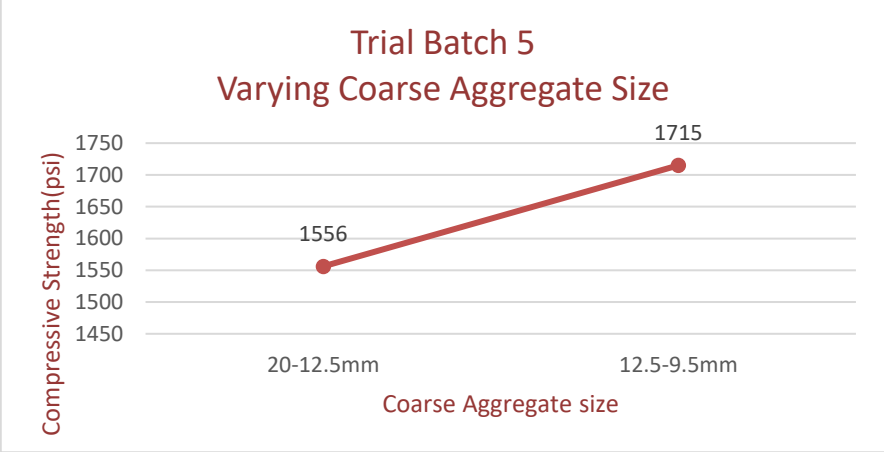

Fig. 11 – Compressive Strength and Coarse Aggregate Size

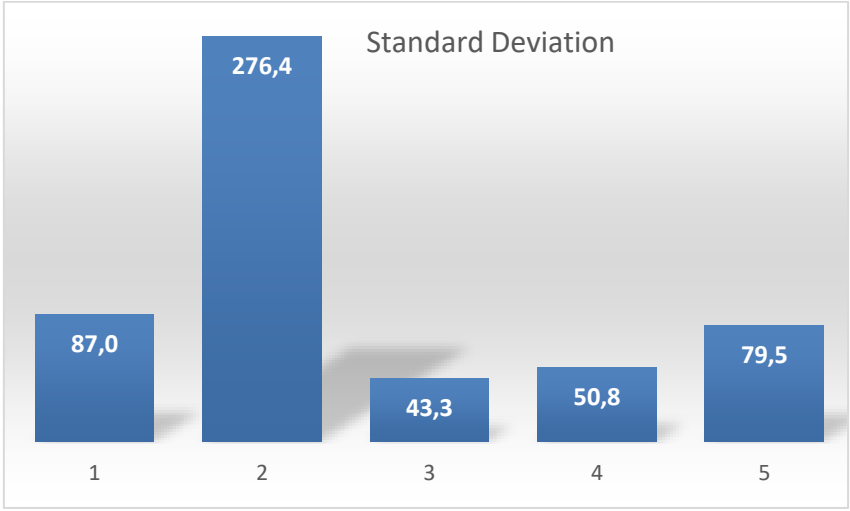

Fig. 12 - Standard deviation of Compressive strengths of each batch

Tab. 3 - Infiltration Rate with corresponding Concrete Mix Design

S #	Concrete Mix	w/c Ratio	Infiltration Rate
			(inch/min)
1.	1:4	0.45	198
2.	1:5	0.45	282
3.	1:6	0.45	335

Discussion:

Figure 7 shows the increment of compressive strength with the rise in curing days of the sample.

Figure 8 and Figure 9 represents the trial batch 2 and 3 respectively. These shows the decrease in Compressive Strength of Pervious Concrete with the increase in Mix Design ratio and water to cement ratio.

Figure 10 and Figure 11 shows the results of trial batches 4 and 5 respectively. These shows the increase in Compressive Strength of Pervious Concrete with the increase in Fine Aggregate percentage but decrease in size of Coarse Aggregate.

The infiltration rate results for three samples of slabs are shown in Table 3 having varying concrete mix design ratios and constant water-cement ratio. The results showed the increment in Infiltration rate of Pervious concrete slab with the increase in Concrete Mix Design ratio.

CONCLUSION

There is lot of research work going on in the field of pervious concrete. Due to its porosity and presence of voids it has lesser compressive strength. Hence the usage of pervious concrete is very limited in Pakistan. With the improved compressive strength and infiltration rate, it can have greater number of applications like in medium to heavy traffic rigid pavements. Therefore, it can also eliminate surface runoff of storm water, facilitates ground water recharge and make the effective use of land

Results showed that mix design ratio with higher cement to aggregate content like 1:6 is considered suitable for pavements requiring less compressive strength but higher infiltration rate. Whereas the lower cement to aggregate ratio like 1:4 showed higher compressive strength and lower infiltration rate.

The reduced water-cement ratio increases compressive strength with less workability, and makes it difficult to work with permeable concrete. The higher the water-cement ratio, decreases the compressive strength, but gives a more workable and permeable concrete. Introducing small percentage of fine aggregate to the pervious concrete although increased the strength but closed some of the pores and hence slow down the infiltration of water through the pavement.

The smaller size coarse aggregate showed greater compressive strength as well as produced more infiltration rate in contrast to large size aggregate.

It is recommended that by the addition of suitable admixture, retarders, super plasticizers and/or any supplementary cementitious materials, the pervious concrete can have more workability and compressive strength so as to achieve the desired design results.

REFERENCES

[1] Kevern, J., Wang ,K., Suleiman, M.T.,& Schaefer,V. R. (2006). Mix Design Development for Pervious Concrete in cold weather climates.Research gate. https://www.researchgate.net/publication/237226150_Mix_Design_Development_for_Pervious_Concrete_in_Cold_Weather_Climates

[2] Elango, K. S., & Revathi, V. (2019). Infiltration and clogging characteristics of pervious concrete Asian Journal of Civil Engineering, 20, Pg 1119-1127 https://doi.org/10.1007/s42107-019-00170-w

[3] Neithalath, N. , Bentz , D.P ., & Sumanasooriya, M. S.(2010). Predicting the Permeability of Pervious Concrete. A Contribution from ACI Committee 236.Concrete international , Pg 35-40

[4] Ong, S.K., Wang,K.,Ling,Y., Shi,G. (2016). Pervious Concrete Physical Characteristics and Effectiveness in Stormwater Pollution Reduction.Institute for Transportation.IOWA State University. http://lib.dr.iastate.edu/intrans_reports/197

[5] Tripathi,D.P.M., Hussain, S.M.A. ,& Madhav,P.(2017). An Experimental Study on Pervious Concrete (Mix-Ratio, Strength and Porous Properties). International Journal of Engineering Research & Technology (IJERT) ISSN: 2278-0181 ,Vol. 6, Issue 12, , Pg100-103 https://doi.org/10.17577/IJERTV6IS120054

[6] Liu,H., Luo,G., Wei,H., & Yu,H.(2018). Strength, Permeability, and Freeze-Thaw Durability of Pervious Concrete with Different Aggregate Sizes, Porosities, and Water-Binder Ratios.MDPI Appl. Sci.,8,1217. https://doi.org/10.3390/app8081217

[7] Pareek,K. & Hong,Y.M.(2019). Prediction of Permeability and Compressive strength for Pervious Concrete, IOP Conference Series: Materials Science and Engineering, 812(2020) 012013

[8] Gowri,T.(2020). Experimental Study of Pervious Concrete.International Journal of Scientific Research & Engineering Trends, Volume 6, Issue 4, Pg 2081-2087

[9] Mahboub,K.C., Canler,J., Rathbone,R., Robl,T., & Davis,B.(2009). Pervious Concrete: Compaction and Aggregate Gradation.ACI Materials Journal, Vol 6, Issue No.6, Pg 523-528

[10] ACI Committee 522.(2010).Report on Pervious Concrete. ACI 522R-10, Pg 522R (1-38)

[11] Rahangdale,S., Maran,S.,Lakhmani,S.,& Gidde,M.(2017) .STUDY OF PERVIOUS CONCRETE. International Research Journal of Engineering and Technology (IRJET), Volume 04, Issue 06, Pg 2563-2566.

[12] Pratap,S.H.,Kapil,S. ,Rakesh,S., & Kumar,K.S.(2016). Enhancement the Strength of Pervious Concrete with Different Water Cement Ratio and Admixture. International Journal of Engineering Research & Technology (IJERT) ISSN: 2278-0181, Vol.5, Issue 01, Pg 582-588, https://doi.org/10.17577/IJERTV5IS010465

[13] Ajamu,S.O., Jimoh,A.A.,& Oluremi,J.R.(2012). Evaluation of Structural Performance of Pervious Concrete in Construction. International Journal of Engineering and Technology, Volume 2, No. 5, Pg 829-836.

[14] Medhani,R. , Khan,W., & Dr. Arhin,S.(2014). Evaluation of Mix Designs and Test Procedures for Pervious Concrete. Research, Development & Technology Transfer Program.

[15] Chopra,M., Wanielista,M., & Mulligan,A.M.(2007). Compressive Strength of Pervious Concrete Pavements. Final Report, Storm water Management Academy, University of Central Florida

[16] Costa,F.B.P. ,Lorenzi,A.,Haselbach,L., & Silva Filho,L.C.P.(2018). Best practices for pervious concrete mix design and laboratory tests. IBRACON Structures and Materials Journal, Volume 11,Number 5, Pg.1151-1159, ISSN1983-4195. https://doi.org/10.1590/s1983-41952018000500013

[17] Maguesvari,M.U., & Narasimha,V.L.(2013). Studies on Characterization of Pervious Concrete for Pavement Applications.2nd Conference of Transportation Research Group of India (2nd CTRG), Procedia - Social and Behavioral Sciences 104, Pg 198 - 207. https://doi.org/10.1016/j.sbspro.2013.11.112

[18] Wang, K., Schaefer, V. R., Kevern,J. T., & Suleiman, M.T.(2006). Development of Mix Proportion for Functional and Durable Pervious Concrete. Research gate. NRMCA Concrete Technology Forum: Focus on Pervious Concrete

[19] Kovac,M.,& Sicakova,A.(2017). Changes of strength characteristics of pervious concrete due to variations in water to cement ratio. 1st International Conference on Advances in Environmental Engineering (AEE 2017), Conf. Series: Earth and Environmental Science 92 012029. https://doi.org/10.1088/1755-1315/92/1/011001

[20] Kumar,S.R.(2015). Characteristic Study on Pervious Concrete. International Journal of Civil Engineering and Technology (IJCIET), Volume 6, Issue 6, , Pp. 165-176

CIVIL ENGINEERING JOURNAL

Article no. 8

THE CIVIL ENGINEERING JOURNAL 1-2023

FIELD EXPERIMENTAL STUDY ON EXTERNAL PRESTRESSING REINFORCEMENT OF A 420M PC CONTINUOUS BEAM BRIDGE

Sun Zhonglin, Sun Quansheng, Li Jianfei and Yang Shengqi

Department of Civil Engineering, Northeast Forestry University, Harbin， 150040, China; sunquansheng@nefu.edu.cn

ABSTRACT

In this paper, the practical engineering of a 420 m prestressed concrete （PC） continuous beam bridge is taken as the research object, and an external prestressing reinforcement method is proposed to reinforce the damaged and cracked girder. The paper is to study the structural performance of a PC continuous beam bridge before and after reinforcement. The heavy vehicle loading test of the reinforced PC continuous beam bridge was carried out. A total of three test spans were selected, and each test span selected seven deflection test sections and a strain test section. The corresponding finite element model was established and verified by the test results. Finally, it was concluded in this study that the external prestressing reinforcement method has a good effect on improving the loading capacity performance of damaged bridges.

KEYWORDS

External prestressing reinforcement, PC continuous beam bridge, Static load analysis, Finite element analysis

INTRODUCTION

Current status of research

In the late 20th century, many reinforced concrete bridges were built in China[1]. With the increase of traffic load and service time, there are also construction defects and environmental changes[2]~[3]. Many bridges have problems such as excessive mid-span deflection, cracking of beam bottom and web[4]. Reinforcement or replacement of old bridges is necessary to ensure safe operation of bridges. If the main beam is replaced directly, it will cause economic losses and vehicle traffic problems[5]. In order to effectively improve the loading capacity and service life of bridges. Many effective reinforcement methods are proposed and applied to the bridge reinforcement[6]~[9].

Before the reinforcement and maintenance of an old bridge, we should first examine and analyse the existing diseases of the old bridge itself, and then select an appropriate reinforcement measure according to the specific situation [10]. External prestressing is widely used to repair existing structures and build new bridges [11] to [14]. This study selected the most suitable external prestressing reinforcement method according to the specific engineering characteristics.

In order to study the performance of external prestressing reinforcement technology, the situation before and after external prestressing reinforcement is compared. The finite element analysis model of the whole bridge is established. The test results are compared with the calculation results of the finite element analysis model, and the performance of the external prestressing reinforcement technology is analysed and evaluated.

Defects of old bridge

A 420 m PC continuous girder bridge was completed in September 1995. Cracks appeared in the roof, floor, and web of the main girder of the bridge under long-term vehicle load and the surrounding environment. Overall, there were more cracks on the outer surface of the bridge. The majority of the crack width is concentrated in the range of 0.10 mm to 0.40 mm, and the length ranges from 0.3 m to 2.6 m. The width, length, and number of these cracks tend to increase over time. The bridge layout is shown in Figure 1.

(a) Field bridge

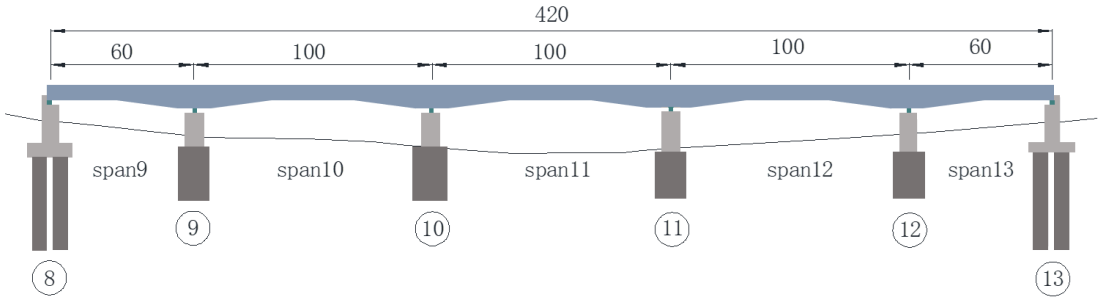

(b)Span and number

Fig.1 - Bridge type layout (unit：m)

At span 9, 5.49 m from the top of pier 9, inclined cracks began to appear on the web. Two oblique cracks were found. The crack lengths were 1 m and 0.91 m, respectively. The crack widths were 0.06 mm and 0.08 mm, respectively. The inclined cracks of spans 10, 11, and 12 were mostly concentrated between 34 and 39.5 meters from the fulcrum. The crack length was 0.41 m to 1.34 m. The crack width is 0.12 mm to 0.42 mm. They are caused by the principal tensile stress. Bending cracks appeared over a distance of 17.8 to 12.4 m. The crack height was between 0.06 m and 0.23 m. The crack width was between 0.02 mm and 0.14 mm. At span 13, 4.43 m from the top of pier 14, the web began to appear inclined. The crack length was 1.15 m. The crack width was 0.12 mm.

Secondly, the box girder floor and roof were checked. Some of the floor cracks were inclined cracks on both sides of the web extending to the middle line of the floor, while others were parallel to the bridge direction. The number of cracks increased gradually from each pier to the middle span. The number of floor cracks in span 10, span 11, and span 12 box girders increased gradually from the pier to the midspan direction. The two sides of the middle line of the floor cracks were symmetrical. In the range of 20 m on both sides of each pier, the bottom plate of the box girder had mainly longitudinal cracks. In the L/4 ~ 3L/4 section, a number of inclined cracks appeared in the bottom plate near the edge of the web. The floor crack width was mainly concentrated between 0.1 mm and 0.4 mm. The length of the crack was mostly concentrated in 0.70 m ~ 4.60 m. The roof

cracks were symmetrically distributed along the bridge deck midline and increased from the pier to the midspan direction. The longest crack was 5.34 m. The maximum crack width was 0.34 mm. In the range of 15.5 m from the piers on both sides (pier 10 and pier 11), dense intermittent longitudinal cracks appeared. The crack length was between 0.30 m and 2.60 m. The crack width was between 0.08 mm and 0.18 mm. The distribution of main cracks in box girders is shown in Figure 2. (Symbol description: crack length is expressed as *L=0.1m*, crack width is expressed as *δ=0.1mm*, crack tilt angle is expressed as *α=45°*)

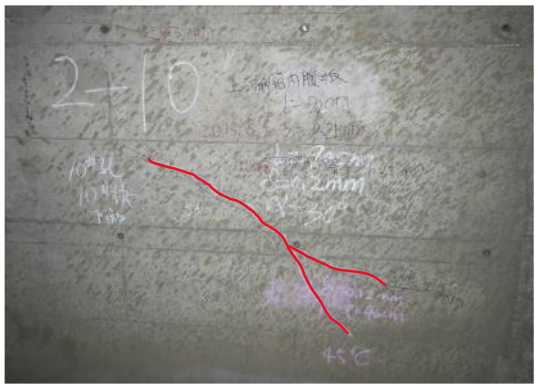

(a) Inclined cracks in the web near the roof of No.10 pier (L=0.9m δ=0.2mm α=45°)

(b) Inclined cracks of the web near the top of No.11 pier (L=2.2m δ=0.18mm α=45°)

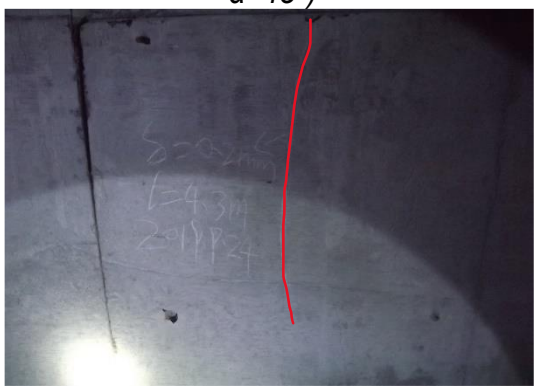

(c) Inclined cracks in the web near the top of No.9 pier (L=4.3m δ=0.2mm α=45°)

(d) Inclined cracks in the web near the top of No.13 pier (L=3.6m δ=0.1mm α=35°)

(e) Inclined cracks of the bottom plate in No.10 hole (L=4.4m δ=0.3mm α=45°)

(f) Inclined cracks of the bottom in No.12 hole (L=5.7m δ=0.4mm α=35°)

(i) Longitudinal cracks in the roof near of No.10 pier (L=2.5m δ=0.2mm α=15°)

(j) Longitudinal cracks in the roof near of No.11 pier (L=1.8m δ=0.3mm α=10°)

Fig.2 - Cracks distribution on the beam.

Finally, the crack distribution of the prestressed tooth plate and diaphragm was checked. There were many inclined cracks at the bottom of the roof at the top prestressed tooth plate of pier 9 and the top prestressed tooth plate of pier 14. The crack length was 0.15 m to 0.52 m. The crack width was 0.08 mm to 0.20 mm. The inclination angle was 30° ~ 60°. There were no stress cracks discovered in the diaphragms of piers 10, 11, 12, and 13. The diaphragm at the middle section of span 9 ~ 13 had vertical cracks on the top of the passing holes. On the one hand, the crack cracked horizontally downward along the direction of hole thickness. On the other hand, it extended vertically upward to the bottom of the roof. The width was between 0.14 mm and 0.30 mm. The length was between 0.35 m and 1.43 m. The distribution of specific cracks is shown in Figure 3.

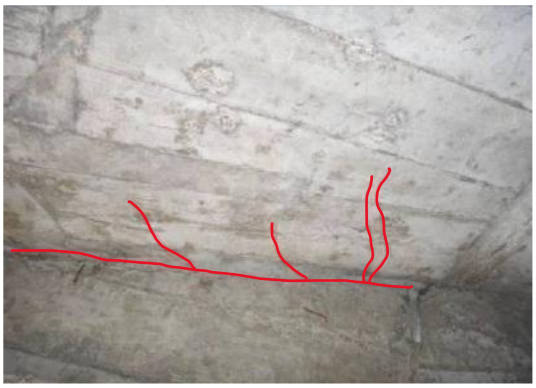

(a) Inclined cracks of tooth plate of No.11 box (L=0.52m δ=0.2mm)

(b) Cracks in diaphragm of No.12 box (L=1.43m δ=0.3mm)

Fig.3 - Crack distribution of tooth plate and diaphragm

Use a tape measure to determine the size of the crack. The crack tester measures the crack's width, and the cracks are categorized based on their placements. Classify all cracks examined as shown in Figure 4.

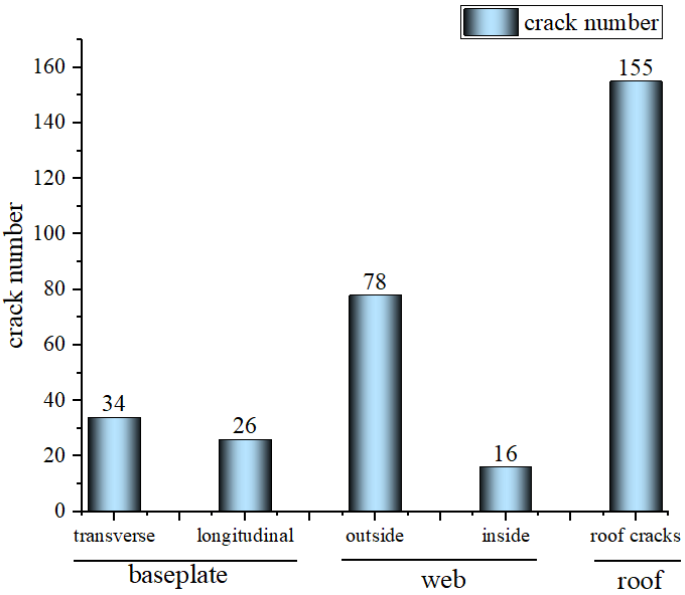

Fig.4 - Number of different types of cracks

METHODS

Layout of External Prestressed Steel Bundles

The externally prestressed tendons were added to the box girder to improve the cross-sectional strength, control the development of cross-section cracks, and effectively improve the stress of the girder. Six strands for span 9 and 13. Eight strands for span 10, 11 and 12, each consisting of 13 steel wires with a nominal diameter of 15.2 mm [15]. The two ends of the side span external prestressed steel beam were respectively anchored on the beam and the anchorage block. The middle-span external prestressed steel beam was cross-anchored on the anchorage block at the pier top. The detailed arrangement is shown in Figure 5.

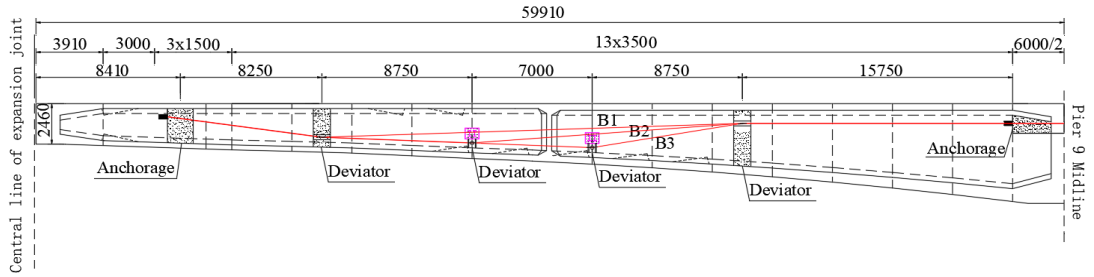

(a) span 9

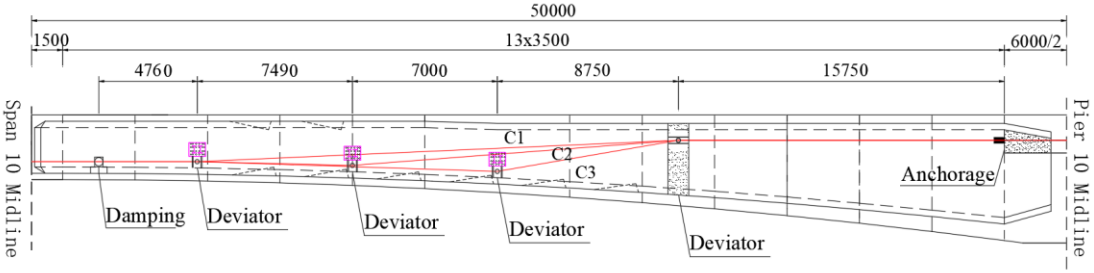

(b) span 10

Fig.5 - Detailed layout of steel beam（unit：mm）

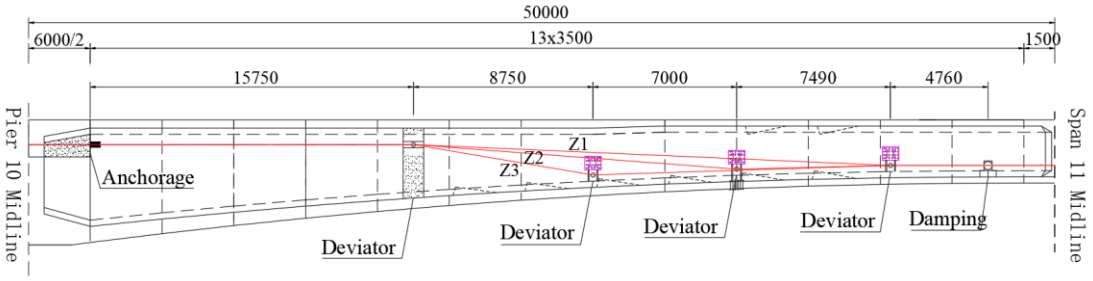

(c) span 11

Fig.5 - Detailed layout of steel beam（unit：mm）

The externally prestressed steel beam was tensioned at both ends. The tension control stress was 1209 MPa. The steel bundle was wrapped in a corrosion-resistant casing. Adjustable cable force and a replaceable anchor were used to facilitate future bridge maintenance. The field layout of externally prestressed tendons is shown in Figure 6.

Fig.6 - Field condition of external prestressed bundle

Test section and loading condition

This bridge's span combination was (60 + 3 x 100 + 60) m. Span 9, 10 and 11 were selected as the test spans. The control load was about 350 kN (according to Chinese design code JTG 021-1989[16]). Static load test using the principle of least favourable arrangement principle[17].The main test content was the deflection and strain of the test span. Finally, the structural performance parameters of the bridge before and after reinforcement were obtained.

Specific test sections were selected as follows: Seven deflection test sections and one strain test section were arranged for each span. The deflection test sections were located at L/8, 2L/8, 3L/8, 4L/8, 5L/8, 6L/8 and 7L/8. The strain test section was located at 4L/8. The specific layout is shown in Figure 7.

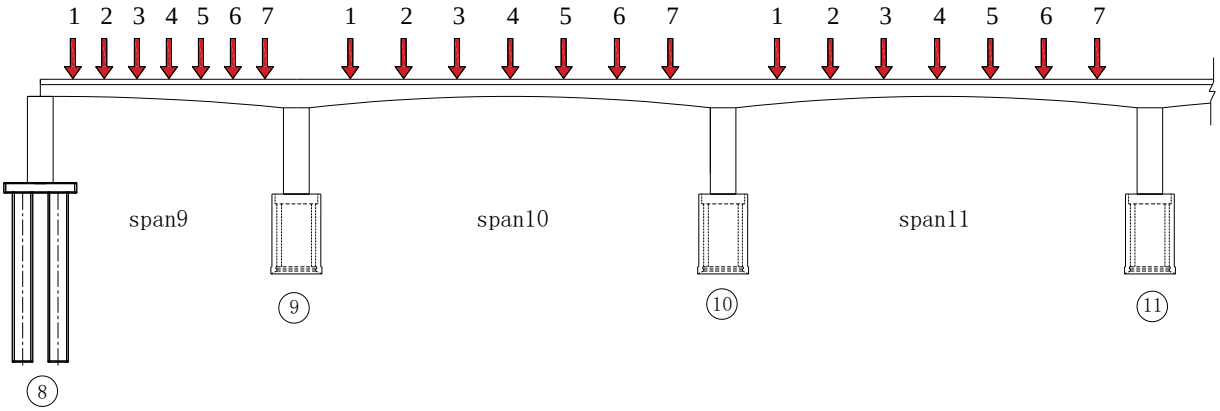

Fig.7 - Deflection and stress test sections

The static load test was divided into six conditions. Eight tri-axle trucks were used to simulate moving loads. A total weight of about 35 tons per truck. It takes 15 minutes to load each time. Then collect the data from each measuring point. Information about the loading condition is shown in Table 1. Loaded vehicle weight information is shown in Table 2. The loading vehicle arrangement is shown in Figure 8.

Tab. 1 - Test conditions and test items

Case No.	Location	Loading condition	Deflection Sensors	Strain Gauges
1	span 9 midspan	centric	√	√
2	span 10 midspan	centric	√	√
3	span 11 midspan	centric	√	√
4	span 9 midspan	eccentric	√	√
5	span 10 midspan	eccentric	√	√
6	span 11 midspan	eccentric	√	√

Tab. 2 - Characteristics of the loading truck (unit：kN)

Truck	Front axle	Middle axle	Rear axle	Total
1	70.1	140.1	140.1	350.3
2	70.2	140.5	140.5	351.2
3	69.9	140.6	140.6	351.1
4	70.4	140.5	140.5	351.4
5	70.2	140.4	140.4	351.0
6	70.3	140.2	140.2	350.7
7	70.3	140.2	140.2	350.7
8	70.4	140.3	140.3	351.0

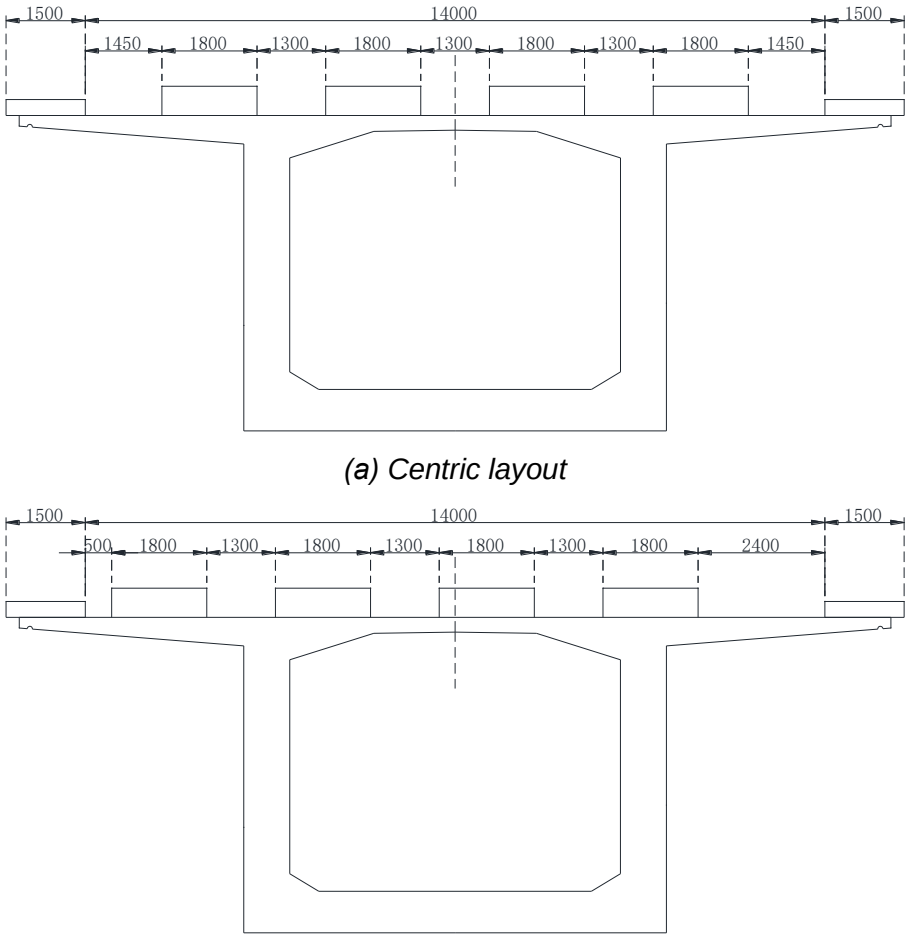

(a) Centric layout

(b) Eccentric layout

Fig.8 - Lateral arrangement of loaded vehicles (unit：mm)

The site vehicle arrangement is shown in Figure 9.

（a）Centric layout *（b）Eccentric layout*

Fig.9 - Site loaded vehicle arrangement

The strain sensors were arranged in the interior of the box girder. The measurement points were arranged on the top, web, and bottom surfaces at the mid-span position and on the top and web surfaces at the abutment position. The deflection was measured with a precision level. In deflection

measurement, the pier top was a fixed point. The tower ruler was placed on the test section. The precision level was placed on the pier top beam. The vertical deflection of the test section relative to the pier top was measured. The arrangement of measurement points is shown in Figure 10.

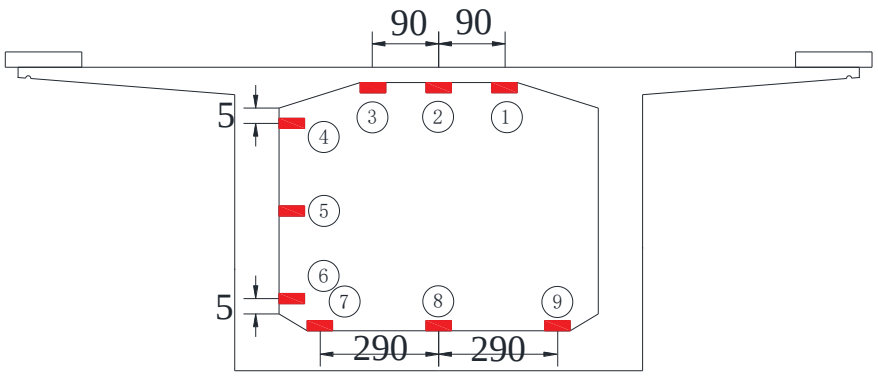

(a) Mid-span strain layout

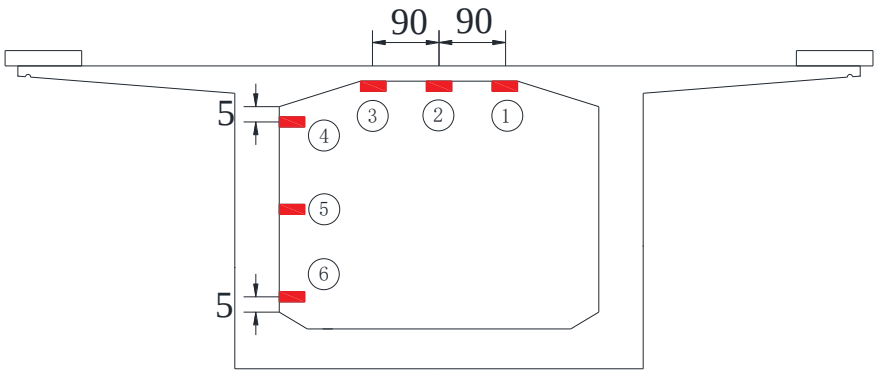

(b) Pier top strain layout

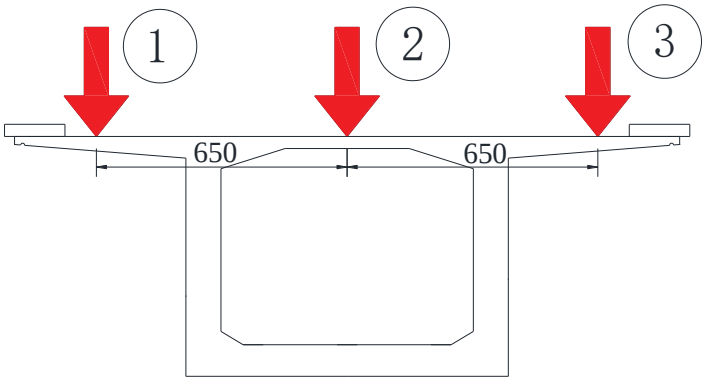

(c) Deflection sensors layout

Fig.10 - Deflection and strain sensor locations illustration(unit：cm)

The picture of the field test is shown in Figure 11.

(a) Field measurement

(b) Field measurement

Fig.11 - Field measurement

RESULTS

Deflection

Deflection is an important parameter to characterize the bearing capacity of a bridge. The vertical deflection data and theoretical finite element model data of spans 9, 10 and 11 before and after reinforcement are shown in Figure 12.

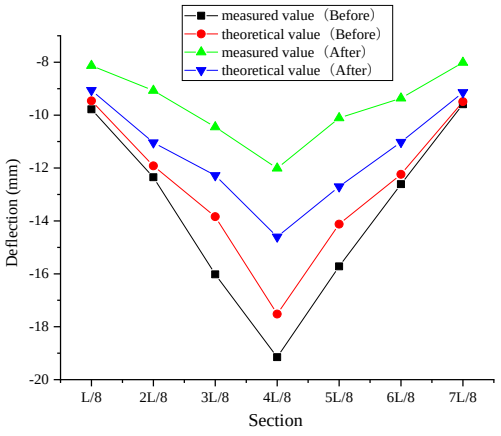

(a) Span 9 centric loadings

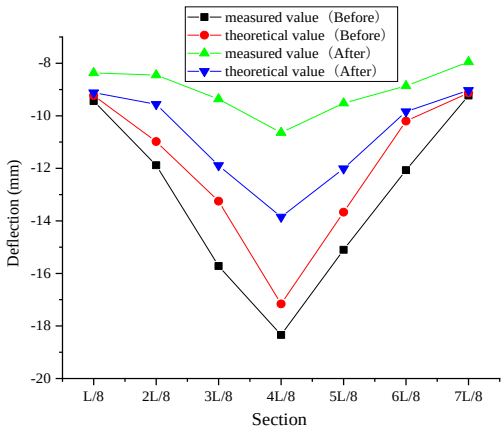

(b) Span 9 eccentric loading

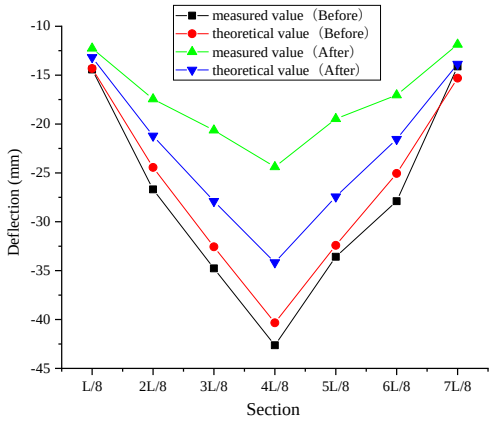

(c) Span 10 centric loadings

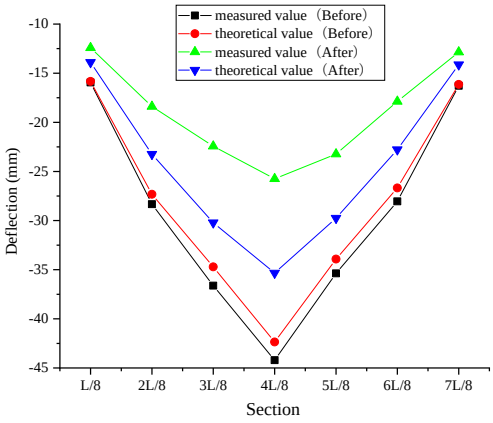

(d) Span 10 eccentric loading

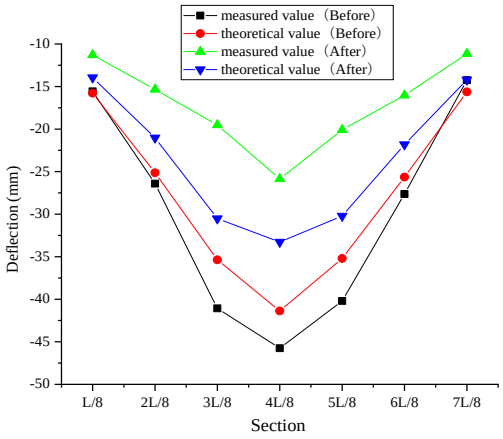

(e) span 11 centric loadings

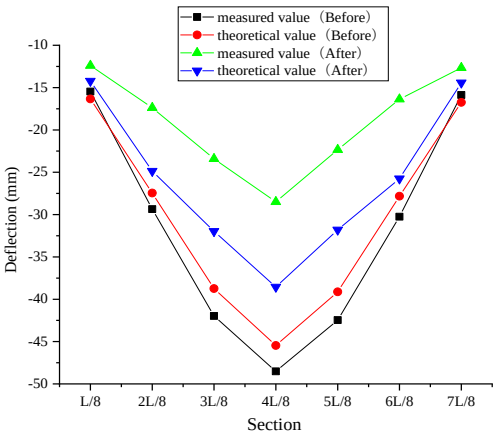

(f) Span 11 eccentric loading

Fig.12 - Vertical displacement data

According to the above curve, the bearing capacity of the No. 9 span increased by 18 %. The bearing capacity of the No. 10 span increased by 15%. The bearing capacity of No. 11 span increased by 18%. These results demonstrate how external prestress can greatly increase the structure's stiffness.

Comparison of deflection data before and after reinforcement. Most measured deflection data had exceeded theoretical data before reinforcement. After reinforcement, the measured deflection data has decreased to varying degrees. The maximum measured deflection after reinforcement is 28.49 mm, which is 41% lower than that before reinforcement of 48.52 mm.

Strain

Stress is another key data point reflecting bridge performance. The measured strain data before and after reinforcement and the theoretical data of the finite element model are shown in Figure 13.

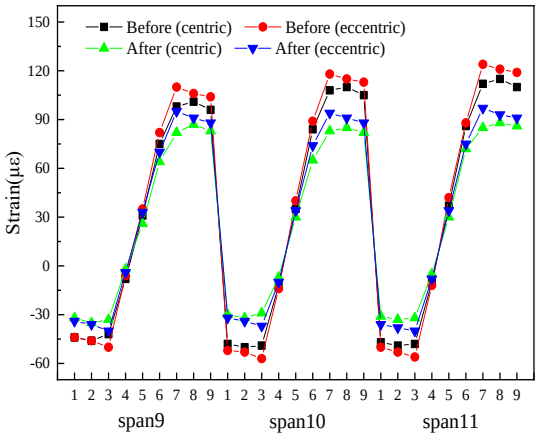

Fig.13 - Measured strain curve under static loading test

The overall performance of the three test spans improved after reinforcement. No. 9 span the strain calibration coefficient between 0.74 and 0.85, the average carrying capacity increased by 24 %, and the average calibration coefficient increased by 22 %. No. 10 span the strain calibration coefficient between 0.71 and 0.83, the average carrying capacity increased by 27 %, and the average calibration coefficient increased by 25 %. No. 11 span the strain calibration coefficient between 0.70 and 0.85, the average carrying capacity increasing by 26%, and the average calibration coefficient increasing by 23%.

From the loading position, the bearing capacity under the central loading condition is increased by 25% on average, and the verification coefficient is increased by 23% on average. Under eccentric loading, the bearing capacity is increased by 23%, and the calibration coefficient is increased by 24%.

At the top of pier 10, the bearing capacity increased by 14% on average. The calibration coefficient increased by 16% on average. The measured strain data are shown in Figure 14.

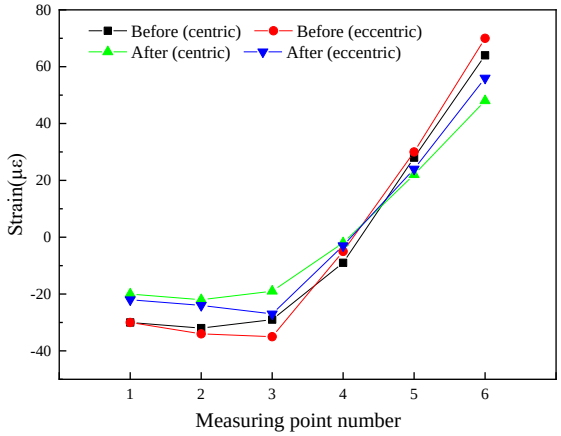

Fig.14 - Measured strain data under static loading test

After external prestressed reinforcement, the stiffness and bearing capacity of the bridge were significantly improved. The safety reserve of the bridge was increased. Which provides security for the continuous service of the bridge.

CONCLUSION

This paper describes the external prestressing reinforcement of a damaged PC continuous girder bridge. Then the static load tests of span 9, span 10, and span 11 are carried out. By comparing the measured data with the theoretical data of the finite element model. It is discovered that the bridge's overall performance has improved. The deflection and strain data after reinforcement are lower compared with those before reinforcement.

Overall, span 9, span 10, span 11 and pier 10 bearing capacity increased by 24%, 27%, 26%, and 14%, respectively. From the loading position analysis, the bearing capacity of central loading increased by 25% on average. The bearing capacity of eccentric loading increased by 23% on average. From the above data, the external prestressing reinforcement method proposed in this paper is very effective for improving the bearing capacity and overall performance of a PC continuous beam bridge with aging damage. In subsequent studies, the external prestressing reinforcement method can be applied to other types of old bridges or can be used in conjunction with some other reinforcement methods.

ACKNOWLEDGEMENTS

Funding: This work was supported by the Jilin Transportation Innovation Development Support (Science and Technology) Project [grant numbers 2020-1-9].

REFERENCES

[1] Editorial Department of China Highway Journal. (2014): Summary of academic research on bridge engineering in China. Journal of China Highway, Vol. 27(05), pp:1-96. DOI:10.19721/j.cnki.1001-7372.2014.05.001.

[2] Czaderski, C., Shahverdi, M., and Michels, J. (2021): Iron based shape memory alloys as shear reinforcement for bridge girders. Construction and building materials, Vol. 274, pp:121793. DOI:10.1016/j.conbuildmat.2020.

[3] Orta, L. (2013): Reliability Assessment of a Continuous Bridge Beam with Exposed Reinforcement. Engineering Structures, Vol. 262, pp:114281. DOI:10.1016/j.engstruct.2022.114281

[4] Editorial Department of China Highway Journal. (2021): Summary of academic research on bridge engineering in China. Journal of China Highway, Vol. 34(02), pp:1-97. DOI:10.19721/j.cnki.1001-7372.2021.02.001.

[5] Eamon, C. D., Jensen, E. A., Grace, N. F. (2012): Life-Cycle Cost Analysis of Alternative Reinforcement Materials for Bridge Superstructures Considering Cost and Maintenance Uncertainties. Journal of materials in civil engineering, vol. 24(4), pp:373-380. DOI:10.1061/(ASCE)MT.1943-5533.0000398.

[6] Michels, J., Staskiewicz, M., Czaderski, C., Kotynia, R., Harmanci, Y. E., and Motavalli, M. (2016): Prestressed CFRP Strips for Concrete Bridge Girder Retrofitting: Application and Static Loading Test. Journal of bridge engineering, vol. 21(5), pp: 4016003. DOI:10.1061/(ASCE)BE.1943-5592.0000835.

[7] Zhang, K., Sun, Q. (2018): Experimental Study of Reinforced Concrete T-Beams Strengthened with a Composite of Prestressed Steel Wire Ropes Embedded in Polyurethane Cement (PSWR-PUC). International journal of civil engineering, vol.16(9A), pp: 1109-1123. DOI:10.1007/s40999-017-0264-x.

[8] Jawdhari, A., Peiris, A., and Harik, I. (2018): Experimental study on RC beams strengthened with CFRP rod panels. Engineering structures, Vol. 173, pp: 693-705. DOI:10.1016/j.engstruct.2018.06.105.

[9] Cadenazzi, T., Dotelli, G., Rossini, M., Nolan, S., and Nanni, A. (2020): Cost and environmental analyses of reinforcement alternatives for a concrete bridge. Structure and infrastructure engineering, Vol. 16(4), pp: 787-802. DOI:10.1080/15732479.2019.1662066.

[10] Buchin-Roulie, V., Kaczkowski, N., Courcelles, C. D., and Toth, M. (2017): Innovative solution for bridge strengthening (for widening and compliance to new codes) by modification of initial static scheme. Paper presented at the IABSE Symposium, Vol. 2017, pp:2504-2511. DOI:10.2749/vancouver.2017.2504.

[11] Aparicio, A. C., Ramos, G., and Casas, J. R. (2002): Testing of externally prestressed concrete beams. Engineering structures, Vol. 24(1), pp: 73-84. DOI:10.1016/S0141-0296(01)00062-1.

[12] Tan, K. H., Tjandra, R. A. (2007): Strengthening of RC continuous beams by external prestressing. Journal of structural engineering-asce, Vol. 133(2), pp: 195-204. DOI:10.1061/(ASCE)0733-

9445(2007)133:2(195).
[13] Xu, J. L., Yi, Z. L., Yang, J. J. (2013): A Study on the Quality Assessment System of External Prestressing Reinforcement Technology. Applied Mechanics & Materials, Vol. 351-352, pp:1347-1353. DOI:10.4028/www.scientific.net/AMM.351-352.1347
[14] Shen, Y., Song, T., Li, G. (2015): Advances of external prestressing tendons in multi-span curved box-girder bridges: Multi-Span Large Bridges (pp: 1255-1262). DOI:10.1201/b18567-164
[15] JTG 3362-2018 Specifications for design of highway reinforced concrete and prestressed concrete bridges and culverts [S]. P.R. China, Ministry of Communications, 2018.
[16] JTJ 021-1989. General Code for Design of Highway Bridges and Culverts[S], P.R. China, Ministry of Communications,1989.
[17] JTG/T J21-01-2015 Load test methods for highway bridges [S]. P.R. China, Ministry of Communications, 2015.

CIVIL ENGINEERING JOURNAL

Article no. 9

THE CIVIL ENGINEERING JOURNAL 1-2023

RESEARCH AND APPLICATION OF U-BIT CONSTRUCTION METHOD IN SUBWAY STATION ENGINEERING LOCATED IN SATURATED SOFT SOIL AREA

Yan Guo[1], Yanfei Zhu[1], Weiqiang Pan[1] and Ye Jin[2]

1. Shanghai Tunnel Engineering Construction Co., Ltd. No.1099 South Wanping Road, Shanghai 200032, China; guoyanyy@foxmail.com, zyflisp@163.com, pwq21@163.com

2. Shanghai Tunnel Engineering & Rail Transit Design and Research Institute, No.1999 West Zhongshan Road, Shanghai 200235, China; 47472837@qq.com

ABSTRACT

In order to solve the problems existing in the construction of underground structures located in the downtown of saturated soft soil area, such as insufficient construction site, complex adjacent structures and great impact on the surrounding environment, the construction method of underground bundled integrate tunnel(U-BIT) is proposed. In this method, after steel pipes jacking completed, concrete is filled into the pipes, and prestress is tensioned to make each independent pipe combined to form a whole bearing structure, so as to achieve the purpose of reducing the size of structural components, improving the structural stiffness and bearing capacity. Based on the structural mechanical property test and the project of Wuding Road Station of Shanghai Metro Line 14, the failure mechanism of bundled integrate structure, the tension technology of prestressed tendons in narrow space and the variation rules of ground surface subsidence are systematically studied. The research shows that structural seam sections will be destroyed before pipe sections, so ensuring the mechanical performance of seam sections is very important to make sure the structural safety. Since each independent pipe is combined to form an overall stable structure under the prestress effect, the subsequent soil excavation has little influence on the tension of prestressed tendons and ground surface subsidence. Therefore, the above construction method can control the ground surface subsidence effectively and reduce the influence of underground engineering construction on the surrounding environment.

KEYWORDS

Underground excavation method, Underground bundled integrate tunnel, Saturated soft soil, Subway station, Prestressed tension, Ground surface subsidence

INTRODUCTION

With the rapid development of economy and urbanization process, the urban population increases with each passing day, which leads to the problems of land resource shortage and traffic congestion. The development and utilization of underground space is the most effective way to solve the above problems. And it is also the useful method to realize the sustainable development of society and economy. However, in the construction of underground structures in the urban central area, there are often problems such as insufficient construction sites and complex adjacent structures. If the open excavation method is adopted, traffic closure, pipeline relocation and demolition of surrounding buildings may be required, which not only has a long construction cycle and a high project cost, but also has a serious impact on the society. Shallow excavation method has been widely used in the construction of underground structures in the downtown because of its

advantages of not affecting traffic pipelines, small construction area and light disturbance to the surrounding environment [1-2]. However, in the saturated soft soil area represented by Shanghai, because of the characteristics of weak foundation bearing capacity, high sensitivity coefficient, fast attenuation of thixotropic strength and difficult control of construction deformation, there are great risks in the application of shallow excavation method in these areas. Although the shield construction method and pipe jacking method can reduce the risk of digging in the saturated soft soil area, the above methods cannot meet the needs of large section and shallow covering soil of urban underground structures due to the limitation of equipment section size and the construction requirement of soil depth [3-5].

As a new type of underground excavation method, the pipe-roofing method uses a small pipe jacking machine to push steel pipes into soil between the starting shaft and the receiving shaft in turn. The pipes are connected with each other by a lock filled with sealing material to form an advanced support system, and then the box culvert is pushed or the soil is excavated under the pipe-roofing structure [6-7]. Therefore, the construction method does not need to reduce groundwater, and the land subsidence is controllable, so it can be applied to the saturated soft soil area, which has been paid attention to by scholars. According to the soil characteristics of above area, Zhu Yanfei et al. [8-9] carried out researches on the technology of steel pipe jacking with sealing grease lock, soil horizontal reinforcement and soil stratified excavation inside the pipe-roof. Based on the Shanghai Tianlin Road Tunnel project, Tang Zheng et al. [10] studied the change law of ground surface subsidence, and found that the value at the stage of pipe jacking is composed of the superposition of stratum loss settlement and surface uplift caused by grouting, while the value at the stage of suspended jacking is mainly consolidation settlement. Relying on the project of Guiqiao Road Station of Shanghai Metro Line 14, Pan Weiqiang [11] concluded that the influencing factors of ground surface subsidence in the process of pipe-roofing structure construction mainly include forebay pressure, pipe jacking speed, water sealing performance of tunnel portal, frictional force between pipe and soil and quality of synchronous grouting. Cheng Panpan et al. [12] accomplished numerical simulation of pipe jacking and soil excavation, and optimized related construction parameters, in order to reduce construction disturbance and speed up the application of this method in the downtown of saturated soft soil area.

However, through applying the pipe-roofing method, engineers found that with the increasing shortage of urban land supply, the construction site may not be able to provide space for making and pushing box culvert. In addition, in the pipe-roofing method, the steel pipes are connected by sealing grease lock, which cannot cooperatively bear loads. In order to overcome the influence of soil rheological properties, soil should be strengthened before excavation, and a large number of temporary steel supports should be installed after excavation, which results in low construction efficiency and high project cost. The above factors have seriously restricted the development of the pipe-roofing method, so it is urgent to study a new kind of pipe-roofing method with small construction space demand, high construction efficiency and adaptability to the geological conditions of saturated soft soil. Based on the PCR construction method [13], the construction method of underground bundled integrate tunnel (U-BIT) is proposed, which is a method that after steel pipes jacking completed, concrete is filled into the pipes, and prestress is tensioned to make each independent pipe combined to form a whole bearing structure. Compared with the traditional pipe-roofing structure, the shape of the pipe in the bundled integrate structure is updated from circular to rectangular, and the number of the sealing grease lock is updated from single to double, as well as the prestress is applied along the ring direction to form an overall structure. Therefore, this kind of structure has smaller pipe size, higher structural stiffness and bearing capacity. Prestressed technology has the advantages of good performance, easy construction and reasonable economy, which is widely used in foundation engineering, large-span structural engineering and bridge engineering. However, due to the large load borne by underground structures and the complex interaction between soil and structures, the application of prestressed technology in underground structures is not widespread at present, and it is only applied in underground large-span structures and shield tunnels. Tang Jian [14] adopted the composite frame system of prestressed beam and

ordinary concrete longitudinal beam in the large-span underground structure, which can make the force distribution of the structure more reasonable and the economic benefit more remarkable. In order to solve the problems of heavy self-weight, obvious cracks and not being able to withstand tension of shield segment, Liu Fengjun [15] applied prestressed technology to shield tunnel, and studied its design theory and design method. For purpose of studying the response and performance of prefabricated prestressed underground pipe gallery with multi-cabin under earthquake action, Wang Jian et al. [16] conducted a finite-element analysis of soil-structure interaction. It is concluded that the setting of prestressed tendons can improve the structural integrity and reduce the structural relative displacement. As a new type of structure, the structural mechanical properties and construction technology of bundled integrate structure is still in the early research stage, and there are no similar projects for reference. In order to ensure the construction safety, based on the project of Wuding Road Station of Shanghai Metro Line 14, the engineering difficulties are studied, and the ground surface subsidence values are monitored and analysed, aiming to give an example for the future excavation project in the downtown of saturated soft soil area.

CONSTRUCTION METHOD OF U-BIT

Structural characteristics

The bundled integrate structure consists of standard steel pipes and working steel pipes, in which the working steel pipes are used for tensioning prestressed tendons. The construction method of the bundled integrate structure can improve the structural mechanical properties by applying prestress in ring direction to each steel pipe, so that the force form is upgraded from the longitudinal stress and transverse bracing to transverse prestress tensioning and cooperative bearing in longitudinal and transverse direction. Therefore, it can effectively control structural deflection, reduce ground surface subsidence, and realize underground excavation without soil reinforcement and support system, which has a significant advantage of construction period and project cost. In addition, the pipe of the above structure can be flexibly combined to form underground space with any different shape, and the construction has low demand for the site, so it can be widely used in underground engineering in complex environment of saturated soft soil area [17]. The bundled integrate structure is given in Figure 2-1.

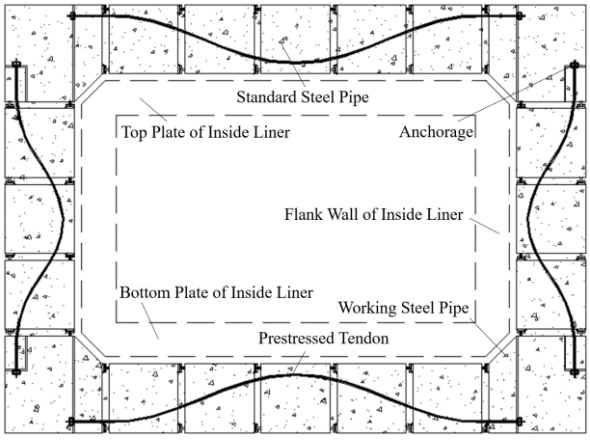

Fig.2-1 Bundled integrate structure

Construction process

Since prestress is needed to apply in each steel pipe of bundled integrate structure, the construction method is different from traditional pipe-roofing method. The specific process is as follows [18]:

(1) Pipe jacking. Between the starting shaft and the receiving shaft, standard steel pipes and working steel pipes are jacked sequentially into surrounding area of the underground structure to be built. The longitudinal direction of pipes is connected by welding, and the transverse direction of pipes is connected by sealing grease lock. Since prestress is applied to steel pipes in the later stage, each pipe has the perforation holes of prestressed tendons.
(2) Prestressed tendons installation. Install corrugated pipes into the perforation holes, and then install prestressed tendons into the corrugated pipes. After the installation of prestressed tendons is completed, concrete is poured into standard steel pipes and seam sections between the pipes.
(3) Tension and anchorage. When the concrete strength meets the design requirements, prestressed tendons are tensioned. After the tensioning force is stable, anchorages are installed to fix the prestressed tendons, so that the prestressed tendons will not retract after the tensioning equipment is withdrawn.
(4) Grout injection and anchor seal. Cement grout is injected into the gap between the corrugated pipes and the prestressed tendons. After the strength of the cement grout meets the design requirements, concrete is poured into the working steel pipes to encapsulate the anchorage.
(5) Soil excavation and structural construction. After completing the tension of prestressed tendons, the bundled integrate structure is formed. Then the soil excavation and structural construction are carried out under the bundled integrate structure.

MECHANICAL PROPERTY TESTS

Test scheme

In order to study the mechanical properties and weak points of the bundled integrate structure, the full-scale tests under design conditions and overload conditions are carried out. Considering the symmetry of the structure and the soil and water pressure load on the structure, one-quarter of bundled integrate structure is selected for the mechanical property tests. Dimensioned drawing of one-quarter of bundled integrate structure is drawn in Figure 3-1. The specimen is 4.2m wide, 3.1m high and 1.5m long. It is arranged in an inverted L shape and consists of working steel pipes, standard steel pipes and semi-standard steel pipes. The size of working steel pipe, standard steel pipe and semi-standard steel pipe are 1.4m×1.4m, 1.0m×1.0m and 0.5m×1.0m separately. And the width of the seam section is 0.1m. Along the longitudinal direction, three bundles of prestressed tendons are set in the width and height directions of the specimen, with a spacing of 500mm, and the designed tensile force is 439.425kN [19].

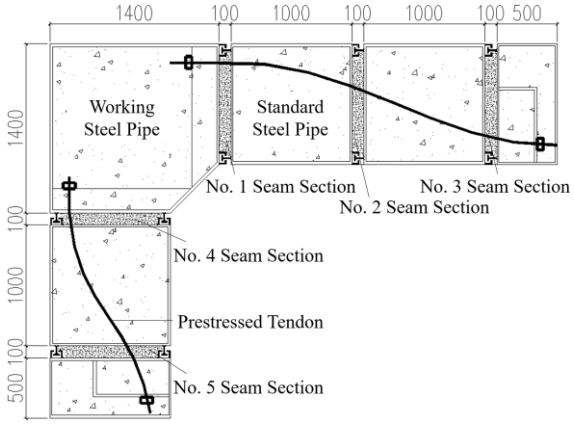

Fig.3-1 Dimensioned drawing of one-quarter of bundled integrate structure (unit: mm)

Loading equipment of structural mechanical property tests is given in Figure 3-2. In the tests, based on the actual load of structure at the service stage, the design of the test loading cases is carried out according to the principle of load equivalence that the total forces of the horizontal and vertical jacks are the same as the sum of actual water and soil pressures imposed on the one-quarter

of bundled integrate structure. The vertical water and soil pressure applied to the structure is simulated by four jacks at the top of the loading equipment, and the horizontal water and soil load applied to the structure is simulated by three jacks on the side of the loading equipment. The right and bottom of the structure are constrained by sliding bearings. Table 3-1 is the loading cases of structural mechanical property tests.

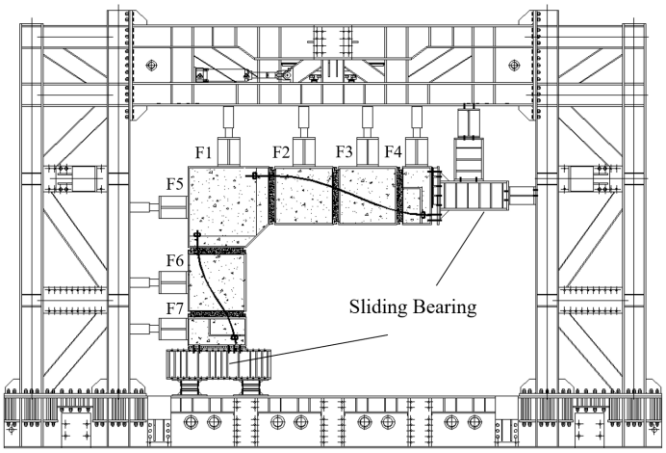

Fig.3-2 Loading equipment of structural mechanical property tests

Tab.3-1: Loading cases of structural mechanical property tests

Loading cases		Structural embedded depth/m	Lateral pressure coefficient	Load value/kN
Preload condition	1	1	0.8	F_1=53 F_2=42 F_3=42 F_4=23 F_5=105 F_6=83 F_7=45
	2	2		F_1=78 F_2=62 F_3=62 F_4=34 F_5=125 F_6=98 F_7=54
	3	3		F_1=104 F_2=81 F_3=81 F_4=44 F_5=145 F_6=114 F_7=62
Design condition	1	3.97	0.8	F_1=128 F_2=101 F_3=101 F_4=55 F_5=165 F_6=130 F_7=71
	2		0.6	F_1=128 F_2=101 F_3=101 F_4=55 F_5=124 F_6=97 F_7=53
	3		0.4	F_1=128 F_2=101 F_3=101 F_4=55 F_5=82 F_6=65 F_7=35
Overload condition	1	3.97	0.6	F_1=128 F_2=101 F_3=101 F_4=55 F_5=124 F_6=97 F_7=53
	2	5		F_1=154 F_2=121 F_3=121 F_4=66 F_5=139 F_6=109 F_7=60
	…	…		…
	13	16		F_1=431 F_2=339 F_3=339 F_4=185 F_5=306 F_6=240 F_7=131

Test result

Table 3-2 is the results of structural mechanical property tests. It can be seen from Table 3-2 that under the preload condition and the design condition, the maximum splaying value of seam section is less than 0.2mm, and the maximum deflection is less than 0.8mm. Initial state of No.2 seam section is given in Figure 3-3. Under the overload condition, when the corresponding structural embedded depth is less than 13m, there is no obvious separation phenomenon of seam section, the maximum splaying value fluctuates is less than 0.3mm, and the maximum deflection is 2.48mm. When the corresponding structural embedded depth increases to 13m, the concrete and the steel pipe are separated at the bottom of No.2 seam section, the maximum splaying value is 0.34mm, and the maximum deflection is 2.89mm. With the increasement of structural embedded depth, the range of seam section separates larger. When the corresponding structural embedded depth increases to

16m, the maximum splaying value of No.2 seam section is 0.43mm, and the maximum deflection is 3.98mm. Failure state of No.2 seam section is shown in Figure 3-4. According to the above mechanical property tests, it is found that structural seam sections will be destroyed before pipe sections. With the increase of structural embedded depth, seam sections are destroyed first, and the splaying value gradually increases, which leads to the increase of structural deflection and the decrease of structural stiffness. So, ensuring the mechanical performance of the seam section is very important to make sure the structural safety.

Tab.3-2: Results of structural mechanical property tests

Loading cases		Structural embedded depth/m	Maximum splaying value of seam section/mm	Maximum deflection/mm
Preload condition	1 2 3	1~3	＜0.2	＜0.5
Design condition	1	3.97	＜0.2	＜0.8
	2			
	3			
Overload condition	1-9	＜13	＜0.3	2.48
	10	13	0.34	2.89
	…	…		…
	13	16	0.43	3.98

Fig.3-3 Initial state of No.2 seam section

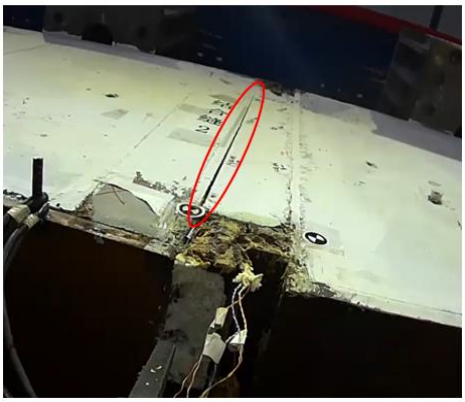

Fig.3-4 Failure state of No.2 seam section

ENGINEERING SITUATIONS

Wuding Road Station of Shanghai Metro Line 14 is located at the intersection of Wuding Road and Wuning South Road. It is an island-style station on the underground second floor. In the No.1 passageway of the station, there is a power pipe gallery that has an impact on the station construction and cannot be moved, so the construction method of bundled integrate structure is adopted. The width of the bundled integrate structure is 8.4m, the height is 6.2m, the length is 15.3m and the depth of covered soil is 3.97m. Plane graph and sectional graph of the underground bundled integrate tunnel are shown in Figure 4-1 and Figure 4-2. It can be seen from Figure 4-2 that steel pipes of the structure are mainly pushed in silty clay, muddy silty clay and muddy clay with high-water content, high compressibility and high sensitivity, which is difficult to construct. Table 4-1 is the physical properties of soils.

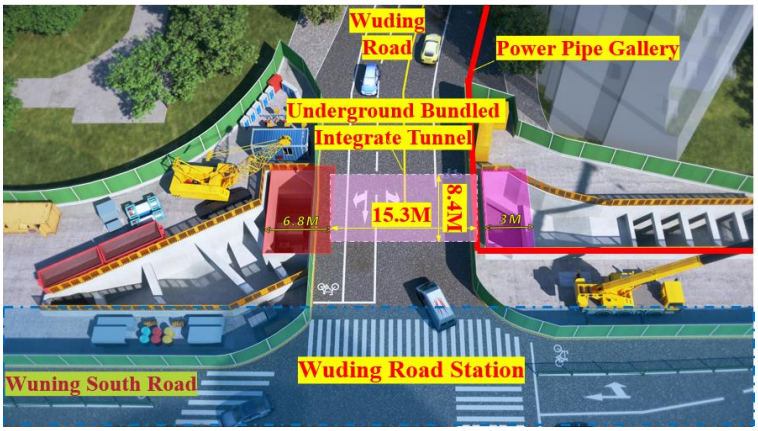

Fig.4-1 Plane graph of underground bundled integrate tunnel

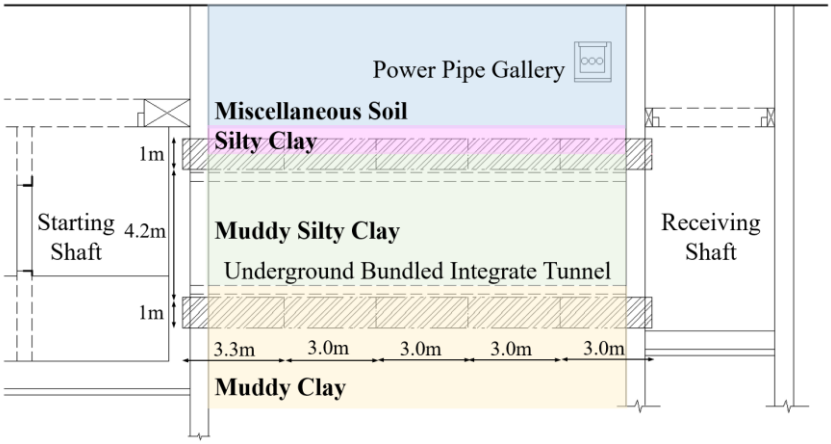

Fig.4-2 Sectional graph of underground bundled integrate tunnel

Tab.4-1: Physical properties of soils

Soil Unit	Name	Soil thickness/m	Unit weight/(kN·m^{-3})	Cohesion/kPa	Internal friction angle/°
1	Miscellaneous Soil	3.3	18.0	10	15
2	Silty Clay	0.5	18.0	18	16
3	Muddy Silty Clay	5.0	17.3	11	14
4	Muddy Clay	7.5	16.7	12	11

The bundled integrate structure is composed of four 1.4m×1.4m and sixteen 1m×1m rectangular steel pipes in the transverse direction, and four standard pipes with a length of 3m and a special pipe with a length of 3.3m are welded in the longitudinal direction. Considering the convenience of construction, prestressed tendons are changed from curve type to double-row linear type. And the model of prestressed tendons is 1×3Ø15.2, the spacing is 750mm, and the tension force is 580kN. In order to ensure the sealing effect of bundled integrate structure, the steel pipes are connected with C-T lock, which is filled with sealing grease. Schematic diagram of C-T lock is presented in Figure 4-3. Figure 4-4 introduces the cross-sectional profile of bundled integrate structure. In order to make steel pipes located in the top row can produce soil arching effect, steel pipes are pushed in the order of jacking steel pipes in the upper row first and then steel pipes in the lower row. In detail,

the upper steel pipes are jacked from A0 pipe, then the left and right sides of steel pipes are jacked, and finally the lower steel pipes are closed at A15 pipe.

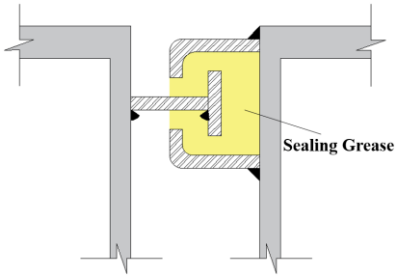

Fig.4-3 Schematic diagram of C-T lock

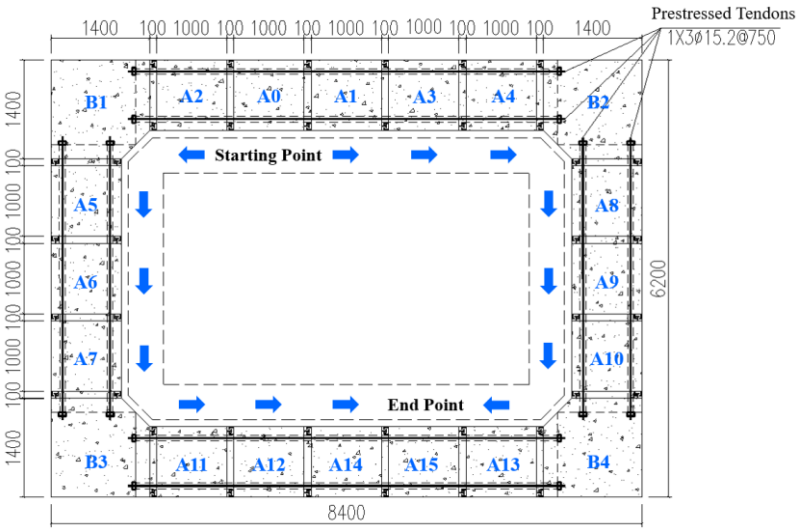

Fig.4-4 Cross-sectional profile of bundled integrate structure

As shown in Figure 4-5, based on the soil in the pipe needs to be cleaned completely, two kinds of earth-pressure balanced pipe jacking machines, which include a pipe jacking machine with three cutterheads and a pipe jacking machine with single cutterhead are adopted [20-21]. The main parameters of the earth-pressure balanced pipe jacking machines are shown in Table 4-2.

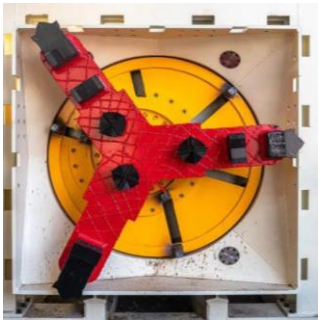

（a）*Pipe jacking machine with three cutterheads* （b）*Pipe jacking machine with single cutterhead*

Fig.4-5 Earth-pressure balanced pipe jacking machine

Tab.4-2: Main parameters of the earth-pressure balanced pipe jacking machines

Type / Item	Pipe jacking machine with three cutterheads	Pipe jacking machine with single cutterhead
Cutting size of cutterhead	1m×1m、1m×1.1m、1m×1.2m	1.4m×1.4m
Structural form of cutterhead	Three leaf-shaped cutterheads with four corner shovel teeth	Single spoke cutterhead with shovel blade
Cutting rate of cutterhead	97.8%	95.6%
Maximum soil excavation speed	3m/h	3m/h
Maximum revolution speed of cutterhead	2r/min	2r/min
Hinge form	Horizontal ±1.5° Vertical ±1.5°	Horizontal ±1.5° Vertical ±1.5° Rotation ±1.5°
Maximum torsional moment of cutterhead	30kN.m	80kN.m
Maximum jacking force of main jacking device	4000kN	

TECHNOLOGY OF TENSIONING PRESTRESSED TENDONS

Since the constraint effect of prestressed tendons is the key factor to ensure that the bundled integrate structure as a whole structure to bear the external load, it is particularly important to ensure the effective prestressing tension in construction. In this project, B1~B4 steel pipes are selected as the working steel pipe to tension prestressed tendons. As shown in Figure 5-1, the size of working steel pipe is 1.4m×1.4m, so the space is very narrow. Therefore, after all the steel pipes are jacked, prestressed tendons are installed and concrete is poured into the standard steel pipes and seam sections. After the concrete strength meets the design requirements, lightweight jack is used to tension prestressed tendons, and the tension force is 580kN. During the tensioning process, the prestressed tendons of same sections are tensioned according to the principle of first vertical, then horizontal and synchronous tensioning, and the prestressed tendons of different sections are tensioned according to the principle of symmetrical staggered tensioning from the middle to both sides. Since the prestressed tendons used in this project are very short, if the traditional anchor device is adopted, prestress loss caused by the retraction of anchorage is very large. Taking vertical prestressed tendons as an example, according to the code for design of concrete structures（GB 50010-2010）[22], the prestress loss of them due to anchor deformation and prestressed tendon shrinkage is 22.3%. Aiming at the above problems, the anchor with low retraction is selected to ensure the prestress tension is effective.

Fig.5-1 Picture of working steel pipe of bundled integrate structure

Variation curves of average tension of prestressed tendons with construction sequence are shown in Figure 5-2. As can be seen from Figure 5-2, the average tension of prestressed tendons is 466kN and the prestress loss is 19.7% after prestressed tendons are tensioned stability. When the concrete strength in the working steel pipes meets the design requirements, the relatively independent steel pipes under the constraint of prestressed tendons are combined into an overall structure, resulting in load redistribution. Part of the load is transferred from prestressed tendons to main structure, and the tension of prestressed tendons decreases by 10.0%. At the stage of soil excavation, the tension of prestressed tendons has been maintained at 410kN, indicating that after steel pipes form a stable structure, the soil excavation does not have a great impact on the structural force, and the tension of prestressed tendons is almost unchanged.

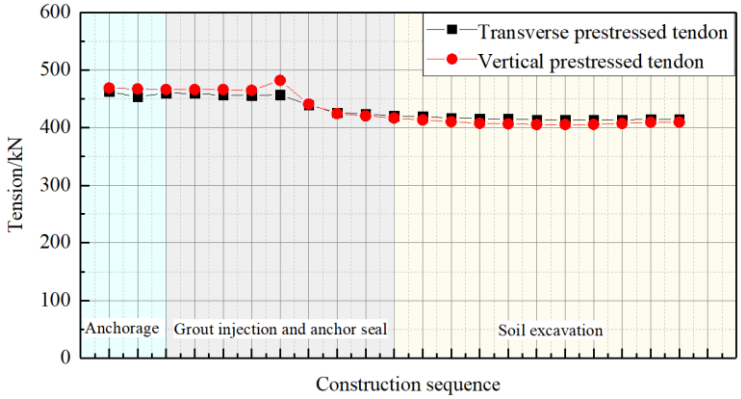

Fig.5-2 Variation curves of average tension of prestressed tendons with construction sequence

ANALYSIS OF GROUND SURFACE SUBSIDENCE

Since this project is the first underground bundled integrate tunnel in China, the influence of its construction on ground surface subsidence is still unclear. Therefore, the above values are monitored. Figure 6-1 is the measuring points layout of ground surface subsidence. A total of 28 ground surface subsidence measuring points of B1-1~14 and B2-1~14 are set up in the area of 3 times the width of bundled integrate structure. The measuring points of B1-1~14 and B2-1~14 are arranged along the fifth and half length of the structure, respectively. For the convenience of analysis, the average values of ground surface subsidence of B1-1~14 and B2-1~14 measuring points are respectively taken and plotted in Figure 6-2, indicating that the variation curves of average ground surface subsidence with construction sequence. It can be seen from Figure 6-2 that the ground surface subsidence shows a downward trend as a whole, and the subsidence mainly occurs at the stage of pipe jacking. After completing the jacking, the value of ground surface subsidence increases slightly. The above results show that steel pipes can form an overall support system under the constraint of prestressed tendons, which significantly reduces the ground surface subsidence caused by soil excavation. In addition, because the bundled integrate structure is fixedly connected with the starting shaft and the receiving shaft, the ground surface subsidence is small on both sides and large in the middle along the longitudinal direction of the structure. Ground surface subsidence curves after each construction sequence completed are given in Figure 6-3. According to Figure 6-3, the influence of structural construction on ground surface subsidence is about twice the width of the structure. After the completion of pipe jacking, the maximum ground surface subsidence of the cross section that the B1 and B2 measuring points located is 4.93mm and 9.66mm respectively. In the subsequent construction process, the values tend to be stable. After soil excavation is completed, the maximum ground surface subsidence of the cross section at B1 and B2 measuring points increases to 6.39mm and 10.16mm separately.

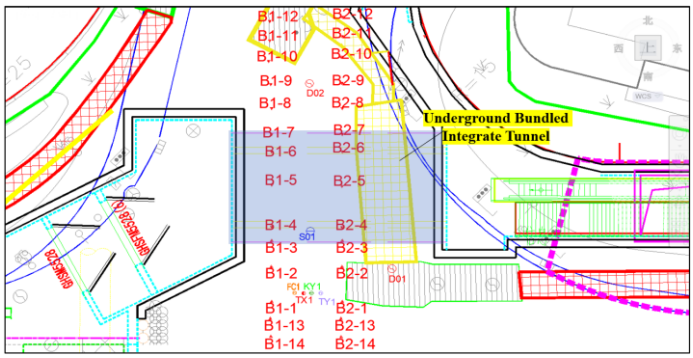

Fig.6-1 Measuring points layout of ground surface subsidence

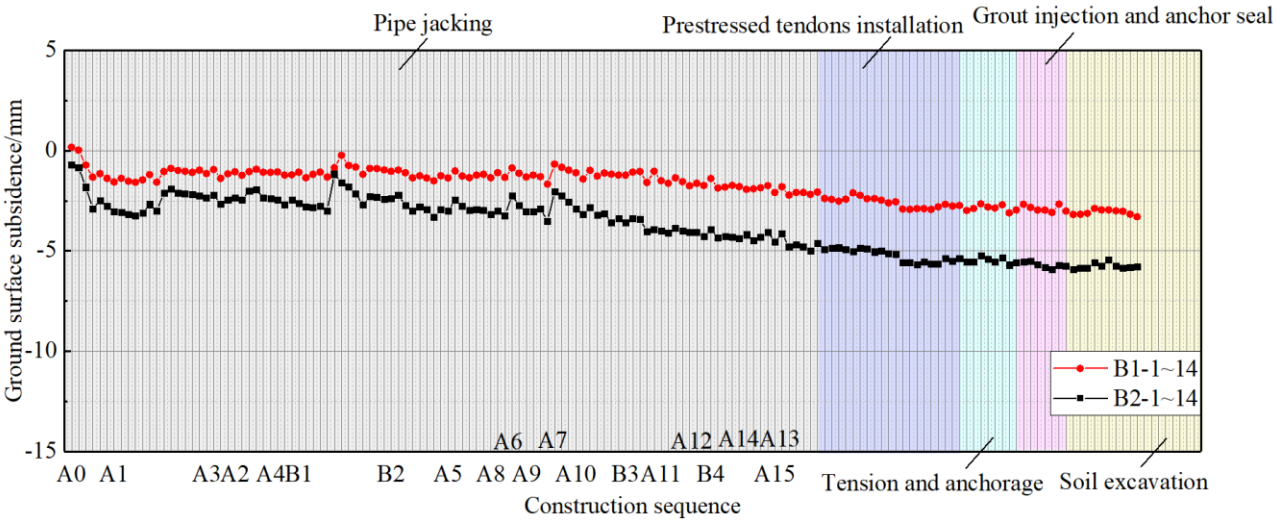

Fig.6-2 Variation curves of average ground surface subsidence with construction sequence

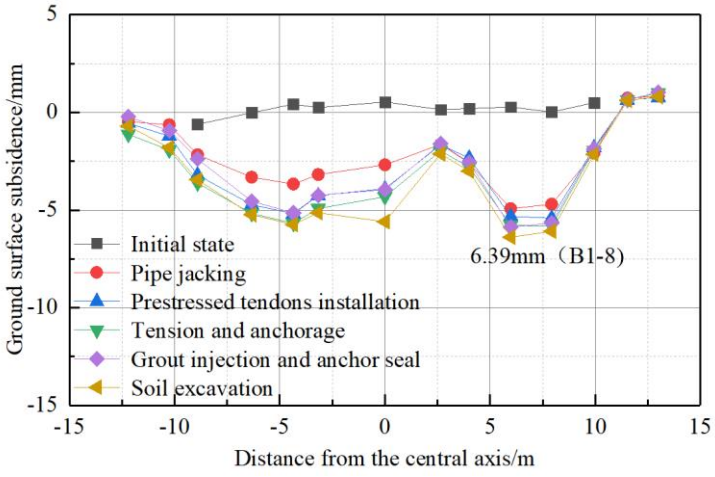

（a）*The cross section where the B1 measurement point is located*

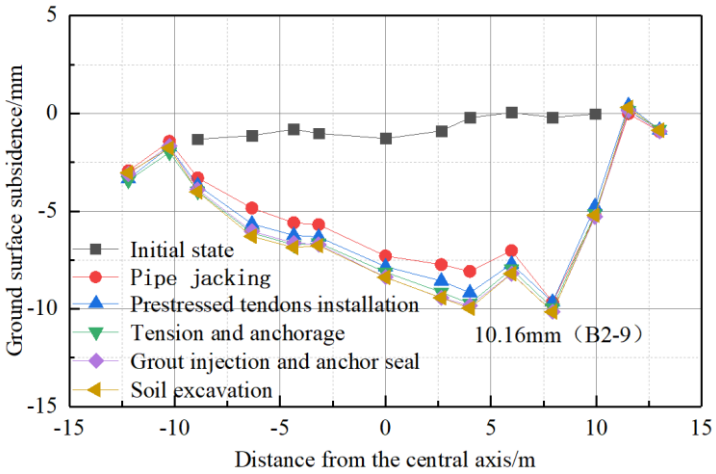

（b） *The cross section where the B2 measurement point is located*

Fig.6-3 Ground surface subsidence curves after each construction sequence completed

CONCLUSION

Based on the project of Wuding Road Station of Shanghai Metro Line 14, the research on the construction method of bundled integrate structure is carried out in this paper, and the following conclusions are obtained.

(1) Compared with the traditional pipe-roofing method, the construction method of bundled integrate structure can improve the structural mechanical properties by applying prestress in ring direction to each steel pipe, so that the force form is upgraded from the longitudinal stress and transverse bracing to transverse prestress tensioning and cooperative bearing in longitudinal and transverse direction. In addition, the pipe of the structure can be flexibly combined to form underground space with any different shape, and the construction has low demand for the site, so it is suitable for underground engineering construction in complex environment.

(2) Seam sections of the bundled integrate structure will be destroyed before pipe sections, so ensuring the mechanical performance of seam sections is very important to make sure the structural safety.

(3) Due to the space of working steel pipe is very narrow, lightweight jack is used to tension prestressed tendons. In addition, in order to reduce the prestress loss caused by anchorage retraction, the anchor with low retraction is adopted to control the anchorage retraction with 1mm. In this project, the average tension of prestressed tendons is 466kN and the prestress loss is 19.7% after the prestressed tendons are tensioned stability.

(4) When the concrete strength in the working steel pipes meets the design requirements, the relatively independent steel pipes are combined into an overall structure, resulting in load redistribution. Part of the load is transferred from prestressed tendons to main structure, and the tension of prestressed tendons decreases slightly. At the stage of soil excavation, because of the steel pipes have already formed a stable structure, the soil excavation doesn't have a great impact on the structural force, and the tension of prestressed tendons is almost unchanged.

(5) The influence of construction of bundled integrate structure on ground surface subsidence is about twice the width of the structure. In addition, the ground surface subsidence shows a downward trend as a whole, and the subsidence mainly occurs at the stage of pipe jacking. After completing the soil excavation, the value of ground surface subsidence increases slightly. In this project, the maximum ground surface subsidence is 9.66mm after finishing the pipe jacking, and the value increase to 10.16mm after soil excavation.

ACKNOWLEDGEMENTS

This work is supported by the Scientific Research Project of Shanghai Science and Technology Commission (Grant No. 19DZ1200900), Academic/Technical Leader Project of Shanghai Science and Technology Commission (Grant No. 20XD1432500).

REFERENCES

[1] Liu Fei, Wang Huiming, Li Huanqiu, Huang Xu, 2021. Numerical Analysis on Ultra-shallow Buried Excavation Method in Underground Commercial street. Chinese Journal of Underground Space and Engineering, vol.17(S1): 180-186.

[2] Chen Jingjun, 2021. Design of Double Deck Tunnel under Passing Urban Main Road with Super Shallow Buried Subsurface Excavation Method. Chinese Journal of Underground Space and Engineering, vol.17(03): 825-833.

[3] Code for Construction and Acceptance of Shield Tunnelling Method(GB 50446-2017), 2017. China Architecture and Building Press.

[4] Liu Fang, Cui Jian, Xu Wanghao, Gao Feng, 2018. Ground Settlement Characteristics for Launching Section of Shallow Overburden Excavation of Large-diameter Slurry Shield Tunnel. Journal of Railway Engineering Society, vol.35(12): 36-40+69.

[5] Zhong Xiaochun, He Chunhao, Li Yongyun, Wang Ziyi, Chen Jie, 2022. Study on Surface Uplift Caused by Construction of Shallow-buried Soil Rectangular Pipe Jacking at Subway Entrance and Exit. Journal of Southwest Jiaotong University, http://kns.cnki.net/kcms/detail/51.1277.U.20220402.1156.002.html.

[6] Xiong Xueyu, Gao Xinyu, Wang Shousheng, Xu Jun, Du Wei, 2018. Study on Technology and Design Method of Prestressed Concrete Roof. Building Structure, vol.48(8): 91-97.

[7] Zhang Yunhai. Design and Construction of Underground Passage Constructed by Pipe-curtain Method in Central Urban Area [J]. Building Construction, 2018, 40(6): 977-980.

[8] Zhu Yanfei, Guo Yan, Pan Weiqiang, Zhao Xiaopeng, 2020. Application of Pipe-roofing Method with Various Section Types in Metro Construction of Guiqiao Road Station at Saturated Soft Soil Area. Tunnel Construction, vol. 40(4): 552-560.

[9] Zhu Yanfei, Bi Xiangli, Guo Yan, Pan Weiqiang, 2021. Summary of Research on Underground Station Excavation Method of Rail Transit at Saturated Soft Soil Area. Tunnel and Rail Transit, vol.(S1): 1-7.

[10] Tang Zheng, Wang Hongxin, Sun Dean, 2022. Study on Law of Surface Displacement during Pipe Roof Construction of Pipe-jacking Group with Large Section. Rock and Soil Mechanics, vol.43(7): 1-9.

[11] Pan Weiqiang, 2019. Monitoring and Analysis of Ground Settlement during Pipe Roof Construction of Pipe-jacking Groups in Soft Soil Areas. Chinese Journal of Geotechnical Engineering, vol.41(S1): 201-204.

[12] Cheng Panpan, Shen Yi, Zhao Xiaopeng, Li Xinxing, Zhu Hehua, 2021. Numerical Analysis and Parameter Optimization of Pipe Curtain Excavation Method in Soft Soil Subway Station. Modern Tunnelling Technology, vol.58(S1): 240-250.

[13] Liu Jiguo. Design and Application of Long-distance Curved Pipe-roofing Method for Ultra-large Oval Section [C] // The International Conference on Pipelines and Trenchless Technology, 2013: 667-678.

[14] Tang Jian. Application of Prestressed Concrete in the Large Span Underground Structures[J]. Journal of Railway Engineering Society, 2013(06):97-102.

[15] Liu Fengjun. Study on the Design Philosophy of Prestressed Concrete Linings for Shield Tunnel[D]. Tongji Universty, 2007.

[16] Wang Jian, Li Mao, Fu Weiqing. Seismic Response Analysis of Prefabricated Precast Prestressed Underground Multi-compartment Municipal Tunnel[J]. Science Technology and Engineering, 2022, 22(16): 6660-6667.

[17] Bi Xiangli, Wang Xiuzhi, Zhang Zhongjie, Pan Weiqiang, Jiao Bochang, Liu Xian, 2022. Full-scale Experimental Study on Shear Performance of Joints of the Bundled Integrate Structure. Journal of Railway Science and Engineering, https://doi.org/10.19713/j.cnki.43-1423/u.T20220291.

[18] Zhang Yaosan, 2020. Study on Prestressed and Integrated Pipe Roof Technology in Saturated Soft Soil Area. Tunnel and Rail Transit, vol.(4): 35-38.

[19] Bi Xiangli, Zhang Zhongjie, Liu Shu, Jiao Bochang, Liu Xian, 2022. Full-scale Experimental Study on Mechanical Behaviors of Bundled Integrate Structure in Saturated Soft Soil Area. Tunnel Construction, vol.42(6): 953-959.
[20] Zhai Yixin, 2022. System for Square Pipe Jacking Machine with Bundle Pipe Curtain. China Municipal Engineering, vol.(2): 96-101.
[21] Peng Shibao, 2022. Bundle Tube Curtain Planetary Driving Multi Cutter Head Square Pipe Jacking Machine Development and Engineering Practice. Mechanical Equipment, vol.(1): 58-61.
[22] Code for Design of Concrete Structures (GB 50010-2010), 2015. China Architecture and Building Press.

CIVIL ENGINEERING JOURNAL

Article no. 10

THE CIVIL ENGINEERING JOURNAL 1-2023

RESEARCH ON A SAFETY EVALUATION SYSTEM FOR RAILWAY-TUNNEL STRUCTURES BY FUZZY COMPREHENSIVE EVALUATION THEORY

Yanfeng Li[1], Jialong Li[1], Jihe Zhao[2], Tongfeng Zhao[3] and Dong Guo[4]

1. *Shenyang Jianzhu University, School of Transportation and Geomatics Engineering, Shenyang 110168, China; lyfneu@126.com, lijialong@stu.sjzu.edu.cn*
2. *Liaoning Technical University, School of Civil Engineering, Fuxin 123000, China; zjh321814@163.com*
3. *Liaoning Provincial College of Communications, Department of Road and Bridge Engineering, Shenyang 110122, China; 734849351@qq.com*
4. *Dalian Branch of China Railway Ninth Bureau Group Co., Ltd., Dalian 116019, China; 457992075@qq.com*

ABSTRACT

Long-term health detection of railway-tunnels is the development direction and trend of future railway tunnel research. Based on the actual engineering of a railway tunnel, this study developed a safety evaluation model for railway tunnel structures using a fuzzy comprehensive evaluation method and examined a health state evaluation method suitable for most railway tunnel structures. The results showed that the evaluation method comprehensively reflected the impact of various factors, which had strong practicality. The evaluation results were clear, accurate, and consistent with engineering practice. When using the safety factor index to study the stress of a railway tunnel structure, Midas/civil analysis showed that different levels of the surrounding rock structural vault in railway tunnels were in a tensile, control-bearing capacity state. When calculating safety factors, the range of a 60° central angle of a railway tunnel vault was calculated according to the tensile control-bearing capacity. Theoretical formulas of the range of the centre angle φ_0 of the vault tension zone were derived and then verified by experiments and numerical analysis.

KEYWORDS

Railway tunnels, Safety factor, Tensile range of vault, Safety evaluation, Fuzzy comprehensive evaluation

INTRODUCTION

With the rapid development of China's railway tunnel engineering and the continuous extension of construction, China has put forward higher requirements for the safety and maintenance of railway tunnels. To improve maintenance efficiency and quality, long-term structural health detection and evaluation must be performed. Therefore, an evaluation method based on the safety of railway tunnels was proposed here. The evaluation method, including monitoring and evaluating the structural health status of railway tunnels, was simulated by fuzzy comprehensive evaluation theory.

Relevant experts at home and abroad have begun to pay attention to the long-term structural health status of tunnels, establishing a long-term structural-safety detection system and formulating a corresponding regulatory system [1–3]. The system has achieved great results in terms of structural-health monitoring sensor technology and detection systems [4, 5]. Long-term monitoring of tunnels

based on fiber detection technology using the Brillouin optical frequency domain (BOFDA) has been reported [6], and its technology used to analyse and study the factors of strain loss, which provides a theoretical basis for engineering practice. In the Asian Railway Tunnel Project, the risk assessment of tunnel safety is divided into four levels [7]. Based on structural destructive testing, non-destructive testing evaluations, static, and 3D nonlinear analysis, Muhammad F has proposed a proper structural health monitoring (SHM) system that will extend the life cycle of a bridge with minimal repair costs and reduced risk of failure [8]. Stanislaw W has proposed a method of structural monitoring using measurement of vertical displacements realized optically by horizontally directed laser beam [9]. Different evaluation methods for evaluating tunnels have been reported [10–13]. These methods have been applied to various types of tunnels, and their effectiveness and practicality of these methods verified. After consulting a large number of studies, the current safety assessment methods for railway tunnels have been found not unified and there is a lack of practical engineering cases and data on the health status of tunnel structures during operation and thus not convincing. Therefore, it is of great significance to establish a system of railway-tunnel structural safety evaluation indicators based on certain rationality, reliability, and practicality.

Using a railway tunnel, as the background, this study used research data, software testing, data analysis, and theoretical analytical methods. Specific research content, with potentially dangerous sources recognized as evaluation indicators, was used to combine on-site measurement information. The safety factor of a railway tunnel was analysed and determined by Midas/civil analysis. Then, different levels of surrounding rock structure of the railway tunnel vault stress state were analysed and theoretical formulas of the range of the centre angle φ0 of the vault tension zone derived and their accuracy verified. Finally, the safety of the railway tunnel was evaluated using a fuzzy comprehensive evaluation method. According to the corresponding safety assessment standards, the final safety level of the actual project of the railway tunnel was obtained. Thus, a system of railway-tunnel structural safety assessment indicators with certain rationality, reliability, and practicality was established.

THEORETICAL STUDY OF THE TENSILE CONTROL RANGE OF RAILWAY TUNNEL STRUCTURES

Railway tunnel engineering background

The engineering background of this research was as follows: the mileage of the railway tunnel was DK34+275 to DK42+895, with a total length of 8620 m, longitudinal slope of 6.0‰, and maximum depth of 398 m. The entrance to this tunnel was flat, the slope ~20o, and intersection angle with the contour line at ~80°. The exit position of this tunnel was flat land, slope ~10°, and intersection angle between the hole and contour lines at 70–80°. According to geological surveys and drilling, the railway tunnel stratum was described as gravel soil, granite, strongly weathered rock, and weakly weathered rock, from new to old, respectively. The depth of water level was 0.5–21.7 m and the permeability coefficient of the stratum recommended as K = 0.00877–0.0698 m/d. The initial support included rock bolts, steel mesh, shotcrete, and steel frame. The secondary lining was divided into 4 types of surrounding rock. The concrete grades of the secondary lining were C30 and C35 and the thickness 30–45 cm.

The calculation of the railway tunnel structure adopted the “load-structure” model [14], and the safety factors calculated by the allowable stress method [15]. According to the Midas/civil finite element simulation, the bending moments and axial forces of surrounding rock at all grades of the railway tunnel were obtained. Simulation research has indicated that the safety of the tunnel is mainly affected by axial forces. Calculating the safety factors of the vault, arch waist, and inverted arch of the surrounding rock at all levels of the railway tunnel, analysis showed that the axial force eccentricities e0 of the vault of the surrounding rock of levels II, IV, and V of the railway tunnel were greater than 0.2 h (h is the thickness of the section) and the vault controlled by tensile strength.

The establishment and analysis of the numerical model

The shaft digging method has a large laneway length, such that it can be transformed into a plane problem. The 1-m length of a longitudinal cross-section was calculated by the finite element method of a plane bar system. When the secondary lining was calculated, the carrying capacity of the initial support was not considered. The calculation diagram is shown in Figure 1.

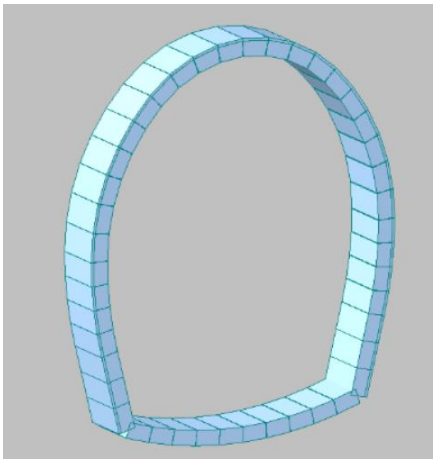

Fig. 1 – Finite element model design drawing

Lining defects mainly occurred in the granite area, with the mechanical parameters of different levels of surrounding rocks stipulated in the *Code for Design of Railway Tunnel TB10003-2016*; the reference values of these mechanical parameters are shown in Table 1. Referring to the geological prospecting of engineering field, the surrounding rock physical mechanical indicators were selected in Table 2, which contained the lining and other materials. For the elastic modulus of the surrounding rock, the deformation modulus was used as an elastic modulus to participate in calculation analysis. The main reason for this was that the deformation modulus, reflecting the stress and strain values of soil under local side limits, was obtained by *in situ* testing, which was applicable.

Tab.1 - Physical and mechanical indices of surrounding rock at all levels

Level	Volume weight γ (kN/m^3)	Elastic reaction coefficient *K* (MPa/m)	Deformation modulus *E* (GPa)	Poisson's ratio *v*	Frictional angle *φ* (°)	Cohesion *c* (MPa)	Calculation of friction angle φ_c (°)
Ⅱ	25–27	1200–1800	20–33	0.2–0.25	50–60	1.5–2.1	70–78
Ⅲ	23–25	500–1200	6–20	0.25–0.3	39–50	0.7–1.5	60–70
Ⅳ	20–23	200–500	1.3–6	0.3–0.35	27–39	0.2–0.7	50–60
Ⅴ	17–20	100–200	1–2	0.35–0.45	20–27	0.05–0.2	40–50
Ⅵ	15–17	<100	<1	1–2	<22	<0.1	30–40

Note: Loess and special surrounding rocks not included in the data and φ_c selected to calculate instead of *φ* and *c*.

Tab. 2 - Selection of basic parameters of materials

Material	Volume weight (kN/m³)	Elastic modulus (MPa)	Poisson's ratio
Initial support	23	2.6e4	0.2
Secondary lining	25	3.15e4 (C35) 2.7e4 (C30)	0.2
Anchor	78	21e4	0.3

Note: Elastic modulus of soil is deformation modulus in numerical analysis software.

Formula derivation of the tensile control range of railway tunnel structures

In practical engineering, most tunnel metrics are calculated as symmetrical hinge less arches, whose two arch toes are equivalent to height. In this study, the tensile control range of tunnel structures were studied by referring to the calculation principle of elastic centre method and polar coordinate system method [16, 17]. The basic thoughts were as follows: The foundation structure with symmetric properties was used as the research object, whose load was divided into symmetric and anti-symmetric loads and the corresponding multi-unknown force simultaneous equations established. By adding a rigid arm, the vice coefficient (δ_{21} and δ_{12}) in the force method equation was 0, such that the problem of the simultaneous equation was transformed into several independent equation-solving problems. Superfluous unknown forces, X_1, X_2, and X_3, were set in the main direction, forming the basic structure of the force method of two extension beams. Among them, unknown forces, as in X_1, X_2, and X_3, were axial, bending moment, and shear forces, respectively (Figures 2 and 3).

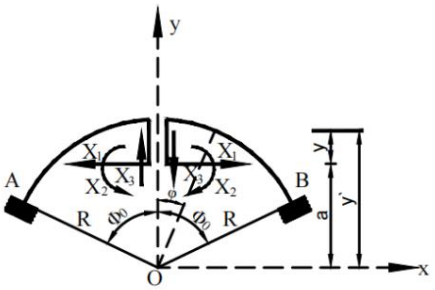

Fig. 2 – Symmetrical equal section without foot arch

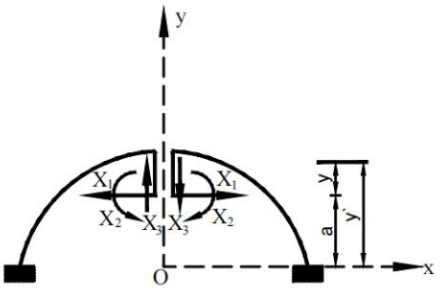

Fig. 3 – Basic structure of elastic centre method

Arched toe A and B are at the same height and the symmetry axis of the circular arch called the *y*-axis. The angle between one arched toe and *y*-axis was recorded as φ, which was represented by the arc. The radius of the scheme arch was *R*.

The following three basic equations of independent force were used to determine the multiple unknown forces, X_1, X_2, and X_3. In the following formula, δ_{11}、δ_{12} are shape constants and Δ_{1P}、Δ_{2P}、Δ_{3P} are load constants, expressed as

$$\delta_{11}X_1+\delta_{12}X_2+\Delta_{1P}=0,\ \delta_{21}X_1+\delta_{22}X_2+\Delta_{2P}=0,\ \delta_{33}X_3+\Delta_{3P}=0 \quad (1)$$

A rigid arm was added to the vault and cut off at the symmetric axis position. In the two symmetric internal forces, X_1 and X_2, when the length of the vertical rigid arm changed, $\delta_{21}=\delta_{12}=0$. The following formula was thus obtained, expressed as

$$\delta_{11}X_1+\Delta_{1P}=0,\ \delta_{22}X_2+\Delta_{2P}=0,\ \delta_{33}X_3+\Delta_{3P}=0 \tag{2}$$

On the geometric symmetry axis *y* of the circular arch, the distance between the elastic centre and arc centre *O* was *a*, expressed as

$$a=\frac{\int y'\frac{1}{EI}ds}{\int\frac{1}{EI}ds}=\frac{R\sin\varphi_0}{\varphi_0} \tag{3}$$

where y' is the height between centroid of any cross-section and arc centre in the arch ring and φ_0 the angle from arch foot section to vault section.

The shape constants δ_{11}, δ_{22}, and δ_{33}, were only related to the geometric size of the arch, while the load constants, Δ_{1P}, Δ_{2P}, and Δ_{3P}, were related to the external load. Using the superposition principle, the final internal force expression of any section of arch ring was obtained as

$$M=\overline{M_1}X_1+\overline{M_2}X_2+\overline{M_3}X_3+M_P,\ Q=\overline{Q_1}X_1+\overline{Q_2}X_2+\overline{Q_3}X_3+Q_P,\ N=\overline{N_1}X_1+\overline{N_2}X_2+\overline{N_3}X_3+N_P \tag{4}$$

where $\overline{M_i},\overline{Q_i}$, and $\overline{N_i}$ are the bending moment, shear force, and axial force, respectively, of any section of the basic structure under a unit unknown force X_i = 1 (i = 1,2,3), M_P, Q_P, and N_P are the bending moment, shear force, and axial force, respectively, of any section of the basic structure under any kind of external load, and *P* in M_P、Q_P、N_P indicate the load [18].

Under the action of a unit unknown force X_i = 1, the calculation formula of the internal force $\overline{M_i}$ and $\overline{N_i}$ of any section of basic structure is shown below.

When X_1 = 1 acts, $-\varphi_0\le\varphi\le\varphi_0$, yielding Eq. (5) as

$$\overline{M_1}=1,\overline{N_1}=0 \tag{5}$$

When X_2 = 1acts, $-\varphi_0\le\varphi\le\varphi_0$, yielding Eq. (6) as

$$\overline{M_2}=R\left(\frac{\sin\varphi}{\varphi}-\cos\varphi\right),\overline{N_2}=\cos\varphi \tag{6}$$

When X_3 = 1 acts, $-\varphi_0\le\varphi\le\varphi_0$, yielding Eq. (7) as

$$\overline{M_3}=-R\sin\varphi,\overline{N_3}=\sin\varphi \tag{7}$$

The shape constants δ_{11}, δ_{22}, and δ_{33} were calculated only considering the influence of bending moment as an example and the shape constants under axial force and shear also calculated. The shape constants were calculated as:

$$\delta_{11}=\int\frac{\overline{M_1}^2}{EI}ds=\frac{1}{EI}\times 2\int_0^{\varphi_0}\overline{M_1}^2Rd\varphi=\frac{2\varphi_0R}{EI}$$
$$\delta_{22}=\int\frac{\overline{M_2}^2}{EI}ds=\frac{1}{EI}\times 2\int_0^{\varphi_0}\overline{M_2}^2Rd\varphi=\frac{R^3}{EI}\left(\varphi_0+\sin\varphi_0\cos\varphi_0-\frac{2\sin^2\varphi_0}{\varphi_0}\right) \quad (8)$$
$$\delta_{33}=\int\frac{\overline{M_3}^2}{EI}ds=\frac{1}{EI}\times 2\int_0^{\varphi_0}\overline{M_3}^2Rd\varphi=\frac{R^3}{EI}\left(\varphi_0-\sin\varphi_0\cos\varphi_0\right)$$

where *E* is the elastic modulus of arch ring material, *I* the inertial moment of arch cross-section, and *A* the cross-sectional area.

The internal force, M_P and N_P, and load constants, Δ_{1P}, Δ_{2P}, and Δ_{3P}, of any section of the basic structure under different external loads were calculated by the following formula,

$$\Delta_{ip}=\frac{1}{EI}\int_s\overline{M_i}M_Pds(i=1,2,3),\Delta_{ip}=\frac{1}{EI}\int_s\overline{N_i}N_Pds(i=1,2,3) \quad (9)$$

According to the actual railway tunnel project and the following two kinds of external load forms, the calculation formulas of internal force, M_P and N_P, and load constants, Δ_{1P}, Δ_{2P}, and Δ_{3P}, of any section of the basic structure under different loads were deduced.

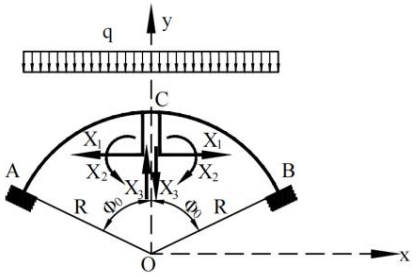

Fig. 4 – Arch span subjected to vertical uniform load q

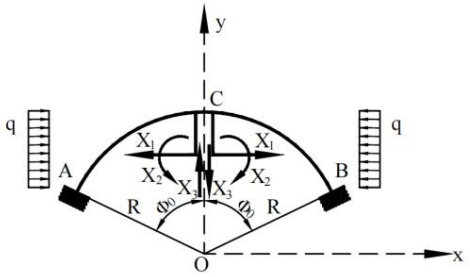

Fig. 5 – Arch span under action of horizontal distributed load q

(1) When the arch span was subjected to vertical uniform load *q* (Figure 4):

The calculation formula of internal forces, M_P and N_P, of an arbitrary section in the basic structure was

$$\begin{cases}M_P=-\frac{1}{2}qR^2\sin^2\varphi & (0\le\varphi\le\varphi_0)\\ N_P=qR\sin^2\varphi\end{cases} \quad (10)$$

The calculation formula of load constants Δ_{1P}, Δ_{2P}, and Δ_{3P} was

$$\Delta_{1P}=\frac{1}{EI}\int_0^{\varphi_0}\overline{M_1}M_Pd\varphi=\frac{qR^3}{EI}\left[\frac{1}{4}\left(\sin\varphi_0\cos\varphi_0-\varphi_0\right)\right]$$
$$\Delta_{2P}=\frac{1}{EI}\int_0^{\varphi_0}\overline{M_2}M_Pd\varphi=\frac{qR^4}{EI}\left\{\frac{\sin\varphi_0}{\varphi_0}\left[\frac{1}{4}\left(\sin\varphi_0\cos\varphi_0-\varphi_0\right)\right]+\frac{1}{6}\sin^3\varphi_0\right\} \quad (11)$$
$$\Delta_{3P}=\frac{1}{EI}\int_0^{\varphi_0}\overline{M_3}M_Pd\varphi=\frac{qR^4}{EI}\left[\frac{1}{6}\left(\cos^3\varphi_0-3\cos\varphi_0+2\right)\right]$$

(2) When the arch span was subjected to a horizontal uniform load q (Figure 5):

The calculation formula of internal forces, M_P and N_P, of the arbitrary section in the basic structure was:

$$\begin{cases} M_P = \dfrac{1}{2}qR^2\left(2\cos\varphi - 1 - \cos^2\varphi\right) (0 \le \varphi \le \varphi_0) \\ N_P = qR\left(\cos\varphi - 1\right) \end{cases} \tag{12}$$

The calculation formula of load constant Δ_{1P}, Δ_{2P}, and Δ_{3P} was:

$$\begin{aligned} \Delta_{1P} &= \frac{1}{EI}\int_0^{\varphi_0}\overline{M_1}M_P d\varphi = \frac{qR^3}{EI}\left(\sin\varphi_0 - \frac{1}{8}\sin 2\varphi_0 - \frac{3}{4}\varphi_0\right) \\ \Delta_{2P} &= \frac{1}{EI}\int_0^{\varphi_0}\overline{M_2}M_P d\varphi = \frac{qR^4}{2EI}\left[\frac{\sin\varphi_0}{\varphi_0}\left(2\sin\varphi_0 - \frac{1}{4}\sin\varphi_0 - \frac{3}{2}\varphi_0\right) - \left(\varphi_0 + \sin\varphi_0\cos\varphi_0 - 2\sin\varphi_0 + \frac{1}{3}\sin^3\varphi_0\right)\right] \\ \Delta_{3P} &= \frac{1}{EI}\int_0^{\varphi_0}\overline{M_3}M_P d\varphi = \frac{qR^4}{2EI}\left(\sin^2\varphi_0 + \cos\varphi_0 + \frac{1}{3}\cos^3\varphi_0 - \frac{4}{3}\right) \end{aligned} \tag{13}$$

The axial force of any section of the arch ring was calculated to be $N = \overline{N_1}X_1 + \overline{N_2}X_2 + \overline{N_3}X_3 + N_P$, where $X_1 = -\dfrac{\Delta_{1P}}{\delta_{11}}$、$X_2 = -\dfrac{\Delta_{2P}}{\delta_{22}}$、$X_3 = -\dfrac{\Delta_{3P}}{\delta_{33}}$.

When the arch span was subjected to a vertical uniform load q, the result was:

$$\begin{aligned} X_1 &= -\frac{\Delta_{1P}}{\delta_{11}} = -\frac{qR^2\left[\dfrac{1}{4}\left(\sin\varphi_0\cos\varphi_0 - \varphi_0\right)\right]}{2\varphi_0} \\ X_2 &= -\frac{\Delta_{2P}}{\delta_{22}} = -\frac{qR\left\{\dfrac{\sin\varphi_0}{\varphi_0}\left[\dfrac{1}{4}\left(\sin\varphi_0\cos\varphi_0 - \varphi_0\right)\right] + \dfrac{1}{6}\sin^3\varphi_0\right\}}{\left(\varphi_0 + \sin\varphi_0\cos\varphi_0 - \dfrac{2\sin^2\varphi_0}{\varphi_0}\right)} \\ X_3 &= -\frac{\Delta_{3P}}{\delta_{33}} = -\frac{qR\left[\dfrac{1}{6}\left(\cos^3\varphi_0 - 3\cos\varphi_0 + 2\right)\right]}{\varphi_0 - \sin\varphi_0\cos\varphi_0} \end{aligned} \tag{14}$$

When the arch span was subjected to horizontal uniform load q, the result was:

$$\begin{aligned} X_1 &= -\frac{\Delta_{1P}}{\delta_{11}} = -\frac{qR^2\left(\sin\varphi_0 - \dfrac{1}{8}\sin 2\varphi_0 - \dfrac{3}{4}\varphi_0\right)}{2\varphi_0} \\ X_2 &= -\frac{\Delta_{2P}}{\delta_{22}} = -\frac{qR\left[\dfrac{\sin\varphi_0}{\varphi_0}\left(2\sin\varphi_0 - \dfrac{1}{4}\sin 2\varphi_0 - \dfrac{3}{2}\varphi_0\right) - \left(\varphi_0 + \sin\varphi_0\cos\varphi_0 - 2\sin\varphi_0 + \dfrac{1}{3}\sin^3\varphi_0\right)\right]}{2\left(\varphi_0 + \sin\varphi_0\cos\varphi_0 - \dfrac{2\sin^2\varphi_0}{\varphi_0}\right)} \\ X_3 &= -\frac{\Delta_{3P}}{\delta_{33}} = -\frac{qR\left(\sin^2\varphi_0 + \cos\varphi_0 + \dfrac{1}{3}\cos^3\varphi_0 - \dfrac{4}{3}\right)}{2(\varphi_0 - \sin\varphi_0\cos\varphi_0)} \end{aligned} \tag{15}$$

Using the exchange decree $\sin\varphi_0 = x$ and $\cos\varphi_0 = y$, the axial force of any section of the arch ring was obtained as:

$$N = y\left\{\frac{-\frac{qR^4}{EI}\left[\frac{x}{\varphi_0}\left(\frac{1}{4}xy-\varphi_0\right)+\frac{1}{6}x^3\right]}{\frac{R^3}{EI}\left(\varphi_0+xy-\frac{2x^2}{\varphi_0}\right)}\right\}+x\left\{\frac{-\frac{qR^4}{EI}\left[\frac{1}{6}\left(y^3-3y+2\right)\right]}{\frac{R^3}{EI}\left(\varphi_0-xy\right)}\right\}+qRx^2+qRy\left(y-1\right)$$
$$+y\left\{\frac{-\frac{qR^4}{2EI}\left[\frac{x}{\varphi_0}\left(2x-\frac{1}{2}xy-\frac{2}{3}\varphi_0\right)-\left(\varphi_0+xy-2x+\frac{1}{3}x^3\right)\right]}{\frac{R^3}{EI}\left(\varphi_0+xy-\frac{2x^2}{\varphi_0}\right)}\right\}+\sin\varphi_0\left\{\frac{-\frac{qR^4}{2EI}\left[x^2+y+\frac{1}{3}y^3-\frac{4}{3}\right]}{\frac{R^3}{EI}\left(\varphi_0-xy\right)}\right\} \quad (16)$$

After simplification, the unary cubic equation about x was obtained as:

$$12\left(\frac{N}{qR}-x^2-y^2\right)\varphi_0^3+\left(12x-6xy^2-12x^3-18xy+2x^3y\right)\varphi_0^2+(21x^2y^2+10x^4y^2-12x^4y$$
$$+18xy^2-19x^2y^3+12x^2y^4+12x^4-36\frac{N}{qR}x^2y^2-36\frac{N}{qR}x^2)\varphi_0+24\frac{N}{qR}x^3y-24x^5y \quad (17)$$
$$-24x^3y^3+24x^5+12x^3y-24x^3=0$$

Verification and analysis of tensile control range of tunnel structure

Safety factors of concrete structure are stipulated in Chapter 8.5.2 of the *Code for Design of Railway Tunnel TB10003-2016*. Safety factors of concrete and masonry structures under main load are shown in Table 3. The minimum safety factor was 2.4 under ultimate compressive strength and the minimum safety factor 3.6 under ultimate tensile strength.

Tab. 3 - Strength safety factors of concrete and masonry structures

Material		Concrete		Masonry	
	Load combination	Main load	Main load and additional load	Main load	Main load and additional load
Damage reason	Concrete or masonry reach ultimate compressive strength	2.4	2.0	2.7	2.3
	Concrete reaches ultimate tensile strength	3.6	3.0	—	—

When the axial eccentricity $e_0 = 0.2h$, the critical state of section tensile and compressive control bearing capacity was present. The safety factor K was 3.6 when the concrete reached its ultimate tensile strength, which was used as the basis for axial force calculations. Therefore, the range of tensile control bearing capacity of a railway tunnel was obtained, which had certain convenience for safety judgment of a railway tunnel and simplified its calculation. Taking the actual railway tunnel as an example, the specific parameters for verification of surrounding rock at all levels are shown in Table 4.

Tab. 4 - Calculation parameters of different level surrounding rock in the railway tunnel

Calculation parameters / Surrounding rock level	Tensile ultimate strength R_1 (kN/m^3)	Thickness h (m)	Width b (m)	Axial force N (kN)	Radius R (m)	Vertical uniform load	Horizontal uniform load
II surrounding rock	2200	0.3	1	1604.2	2.8	27.0972	0
Ⅲ surrounding rock	2200	0.3	1	1604.2	2.8	50.0256	7.50384
Ⅳ surrounding rock	2400	0.35	1	1871.53	2.85	91.1772	20.5149
Ⅴ surrounding rock	2400	0.4	1	3500	2.9	160.9056	64.3622

According to equation derivations, specific parameters were introduced into the derivation for calculation and the angle of the tensile centre of the railway tunnel vault obtained. The specific results were as follows. The calculated central angle φ_0 of the tensile control bearing capacity was 34.9, 45.1, 38.7, and 30.3° for levels II, III, IV, and V of the surrounding rock, respectively. The vault section of the actual railway tunnel in levels II, IV, and V of the surrounding rock was tensile-controlled bearing capacity. When calculating the safety factor of the tunnel, the safety factor was calculated according to the tensile-controlled bearing capacity of the vault in the range of a 60° central angle of the railway tunnel section.

STUDY ON FUZZY COMPREHENSIVE EVALUATION THEORY OF THE RAILWAY TUNNEL

Fuzzy comprehensive evaluation theory

The safety of tunnel structure is affected by stress characteristics, geological conditions, structural defects and other factors. Therefore, in the process of safety assessment of tunnel structure, the influence of various factors must be fully considered, and its own characteristics must be considered. Using qualitative or quantitative evaluation methods alone cannot obtain accurate evaluation results.

Fuzzy comprehensive evaluation is a combination of qualitative and quantitative evaluation method. It can consider multiple factors and multiple types, and organically combine the fuzzy characteristics and diversity characteristics of influencing factors. The results are accurate and systematic. It is a more suitable evaluation method for engineering practice.

Fuzzy comprehensive evaluation is an analysis method based on fuzzy mathematics and is widely used in tunnel engineering. Multistage fuzzy comprehensive evaluation was based on fuzzy comprehensive evaluation and a basic model of vague comprehensive evaluation established, which reflected the status and functions of various evaluation factors in overall evaluation. Each influencing factor was analysed comprehensively and impact factors classified by levels. Initially, a first-level comprehensive evaluation was carried out and the evaluation results then used as evaluation indices for conducting a secondary comprehensive evaluation.

Fuzzy comprehensive evaluation theory is a comprehensive evaluation method considering multi-factor fuzzy mathematics [19]. The choice of these factors directly affected result evaluation. To ensure the accuracy, objectivity, and practicability of the evaluation results, the basic principles of systematics and universality must be followed when selecting the influencing factors for

evaluation. The evaluation was based on considered factors, such as the geological environment of the railway tunnel, structural defects, and structural stress. The safety evaluation indicators of railway tunnels were set as:

(1) Engineering geological conditions N_1: rock quality index n_{11}, leakage water n_{12}, completeness of surrounding rock n_{13}, fault fracture zone n_{14}, rock characteristics of surrounding rock n_{15}, and *in situ* stress coefficient n_{16}.

(2) Structural defect N_2: lining thickness defect position n_{21}, effective thickness ratio of lining n_{22}, concrete strength n_{23}, and defect site of lining steel bar n_{24}.

(3) Structural stress N_3: lining pressure control n_{21} and lining tension control n_{22}.

(4) Other factors N_4: construction design level n_{11}, seismic fortification intensity n_{12}, and year of service n_{13}.

Determination of algorithm theoretical weight and membership function

A judgment matrix containing various indicators was established. Experts have considered the relative importance levels of each indicator and provided corresponding scores in accordance with a 1–9 scale method [20]. With this scale, 1 means that both are equally important, 3 that the former is slightly more important than the latter, 5 the former is significantly more important than the latter, 7 the former is strongly more important than the latter, and 9 the former is extremely more important than the latter. Thus, 2, 4, 6, and 8 means the importance is between two numbers. The analytic hierarchy process (AHP) [21] was used to determine the weight of railway tunnel structural safety factors. Then, the weight of each index was obtained by normalizing the corresponding feature vector. For a judgment matrix, a consistency test is often carried out to verify whether it is consistent with reality. On this basis, the consistency test of the obtained weights was carried out to ensure reliability of the subsequent sorting and decision-making. Professor Saaty [22] has believed that, if there is no big deviation between the obtained decision matrix and the consistency requirement, the decision matrix reaches “satisfactory consistency,” which was calculated here according to the definition of consistency index, expressed as:

$$CI = \frac{\lambda_{\max} - n}{n-1} \tag{18}$$

$$CR = \frac{CI}{RI} \tag{19}$$

where CI is the consistency index, CR the consistency ratio, RI the random consistency index, and n the order of the judgment matrix.

The consistency index CI was calculated using the maximum characteristic root λ_{max} of the judgment matrix and the consistency ratio calculated by the average random consistency index RI. When CR was <0.1, the decision matrix met the condition of "satisfactory consistency." When CR was >0.1, the decision matrix needed to be adjusted accordingly. The weights of various indicators of railway tunnel engineering are shown in Table 5.

Tab. 5 - Index Weight of a Railway Tunnel

Criterion layer	Weight	Index layer	Weight
Engineering geological conditions N_1	0.086036	Rock quality index n_{11}	0.1468
		Leakage water n_{12}	0.0811
		Completeness of surrounding rock n_{13}	0.0811
		Fault fracture zone n_{14}	0.2671
		Strength characteristics of surrounding rock n_{15}	0.1468
		In situ stress coefficient n_{16}	0.2671
Structural defect N_2	0.23945	Lining thickness defect position n_{21}	0.17697
		Effective thickness ratio of lining n_{22}	0.56649
		Concrete strength n_{23}	0.07099
		Defect site of lining steel bar n_{24}	0.18554
Structural stress N_3	0.521513	Lining pressure control n_{31}	0.8333
		Lining tension control n_{32}	0.1667
Other factors N_4	0.152997	Construction design level n_{41}	0.2000
		Seismic fortification intensity n_{42}	0.4000
		Year of service n_{43}	0.4000

The membership function was a means for obtaining the membership degree, which considers the operability of the project in engineering practice as well as objectivity. As the evaluation of each influencing factor had both quantitative and qualitative characteristics, the membership functions constructed should be different. Determining the membership function of four qualitative factors includes leakage water, integrity of surrounding rock, fault, and fracture zone. In defect location of lining thickness and lining reinforcement as well as construction design level, each index requires quantification. The evaluation interval of each factor can be divided into four levels: excellent (0.9), good (0.7), medium (0.5), and poor (0.3) [23]. The membership function was expressed by a trapezoidal function:

$$A(x)=\begin{cases}1 & x<a\\ \dfrac{b-x}{b-a} & a\leqslant x\leqslant b\\ 0 & b<x\end{cases} \qquad A(x)=\begin{cases}0 & x<a\\ \dfrac{x-a}{b-a} & a\leqslant x\leqslant b\\ 1 & b<x\end{cases} \qquad A(x)=\begin{cases}\dfrac{x-a}{b-a} & a\leqslant x<b\\ 1 & b\leqslant x<c\\ \dfrac{d-x}{d-c} & c\leqslant x\leqslant d\\ 0 & x<a \text{ or } d<x\end{cases} \tag{20}$$

Smaller type Larger type Intermediate type

Miscellaneous factors and the axial force and bending moment of the main structure under load were expressed by a Gaussian distribution function, being:

$$A(x)=\begin{cases}1 & x\leqslant a\\ e^{-\left(\frac{x-a}{\sigma}\right)^2} & a<x\end{cases} \qquad A(x)=\begin{cases}0 & x\leqslant a\\ 1-e^{-\left(\frac{x-a}{\sigma}\right)^2} & a<x\end{cases} \qquad A(x)=e^{-\left(\frac{x-a}{\sigma}\right)^2} \; -\infty<x<+\infty a \tag{21}$$

Smaller type Larger type Intermediate type

where $\sigma = \frac{x_{i+1} - x_i}{2\sqrt{-\ln 0.5}}$ is the average value of the interval of each factor at the security level and σ the corresponding variance.

FUZZY COMPREHENSIVE EVALUATION OF RAILWAY TUNNEL STRUCTURAL SAFETY

Based on the theory of fuzzy comprehensive evaluation, a safety evaluation model of the railway-tunnel structure was built. Fifteen factors affecting the safety of a tunnel structure in 4 categories were analyzed in detail. According to references [24, 25], the division standards of all influencing factors were standardized. Through the analysis of relevant literature and norms at home and abroad, it has been found that the assessment level should not be too high and the application of 4 levels of division has been widely applied, with level I a safe structure, level II a basic security structure, level III a great hidden-danger structure, and level IV an unstable structure.

This article focused on explaining the stress characteristics of railway tunnels. The second lining of railway tunnels is mainly affected by axial forces and bending moments. They are long-term engineering quality monitoring projects and are related to tunnel structural safety. According to a study regarding the tensile control angle range of railway tunnels, the safety factor level of the lining structure can be divided into tension and compression zones. Among these, safety level I means that the secondary lining of the tunnel bears a relatively small load and the safety factor of the bending moment and axial load higher by 2-fold than that specified in the specification. Basic safety level II means that the secondary lining bears a relatively large load, resulting in tiny cracks, with the safety factor at 1 to 2-fold that specified by the standard. The potential unsafe level III means that the tunnel lining structure has cracked or fallen off, but it can still bear the local load, such that the safety factor is less than the specified requirements but greater than 1. The unsafe level IV means that the tunnel lining having perforations and cracks, in which the load can no longer be carried and the safety factor <1.

In view of the universality of the evaluation system, level III surrounding rock of the actual railway tunnel project was selected to represent for safety evaluation. The detection of the railway tunnel is shown in Table 6.

Tab. 6: Detection of level III surrounding rock in the railway tunnel

Fuzzy comprehensive evaluation factors of tunnel safety		Detection
Engineering geological conditions	Rock quality index	Rock granite, rock mass relatively complete
	Leakage water	No water leakage, seasonal dripping on arch
	Completeness of surrounding rock	No voids exist in surrounding rock
	Fault fracture zone	No faults or fractures nearby
	Strength characteristics of surrounding rock	Uniaxial saturated compressive strength 90 MPa
	In situ stress coefficient	Ground stress coefficient 3
Structural defect	Lining thickness defect position	Arch waist
	Effective thickness ratio of lining	Effective thickness ratio 0.93
	Concrete strength	Concrete strength 0.95
	Defect site of lining steel bar	Arch waist
Structural stress	Lining pressure control	(Pressure zone) bending moment 35.6 kN·m (Pressure zone) Axial force 815.31 kN
	Lining tension control	(Tension zone) bending moment 42.14 kN·m (Tension zone) axial force 781.89 kN
Other factors	Construction design level	High level of construction design
	Seismic fortification intensity	Seismic fortification intensity 6
	Year of service	Three years

Detection of the above factors was brought into the membership function to obtain the relationship matrix, with R_1 representing the membership matrix of engineering geological conditions, R_2 the structural defect membership matrix, R_3 the surrounding rock (compression zone) membership matrix, R_4 the surrounding rock (tension zone) membership matrix, and R_5 the membership matrix of other factors. The details were as follows:

$$R_1 = \begin{pmatrix} 0.00 & 0.606 & 0.245 & 1.00 \\ 1.00 & 0.00 & 0.00 & 0.00 \\ 1.00 & 0.00 & 0.00 & 0.00 \\ 1.00 & 0.00 & 0.00 & 0.00 \\ 0.84 & 0.00 & 0.00 & 0.00 \\ 0.89 & 0.89 & 0.34 & 0.00 \end{pmatrix} \quad R_2 = \begin{pmatrix} 0.00 & 1.00 & 0.00 & 0.00 \\ 1.00 & 0.26 & 0.28 & 1.00 \\ 0.84 & 0.01 & 0.42 & 1.00 \\ 0.00 & 1.00 & 0.00 & 0.00 \end{pmatrix}$$

$$R_3 = \begin{pmatrix} 1.00 & 0.27 & 0.44 & 0.00 \\ 1.00 & 0.00 & 0.02 & 0.00 \end{pmatrix} \quad R_4 = \begin{pmatrix} 0.97 & 0.97 & 0.91 & 0.00 \\ 1.00 & 0.67 & 0.82 & 0.00 \end{pmatrix} \quad (22)$$

$$R_5 = \begin{pmatrix} 1.00 & 0.00 & 0.00 & 0.00 \\ 0.00 & 0.06 & 1.00 & 0.06 \\ 1.00 & 0.895 & 0.17 & 0.00 \end{pmatrix}$$

First-order fuzzy comprehensive evaluation was then conducted on the above relational matrix, with C_1 representing the fuzzy relational matrix of engineering geological conditions, C_2 the fuzzy relation matrix of structural defect factors, C_3 the fuzzy relation matrix of surrounding rock (compression zone), C_4 the fuzzy relation matrix of surrounding rock (tension zone), and C_5 the fuzzy relation matrix of other factors. The details were as follows:

$$\begin{aligned} C_1 &= a_1 \times R_1 = (1.035764 \quad 0.3351236 \quad 0.130057 \quad 0.1506) \\ C_2 &= a_2 \times R_2 = (0.64589 \quad 0.49675 \quad 0.19353 \quad 0.65687) \\ C_3 &= a_3 \times R_3 = (1.00 \quad 0.225 \quad 0.37 \quad 0.00) \\ C_4 &= a_3 \times R_4 = (0.98 \quad 0.92 \quad 0.845 \quad 0.00) \\ C_5 &= a_4 \times R_5 = (0.60 \quad 0.382 \quad 0.468 \quad 0.024) \end{aligned} \quad (23)$$

The second-level fuzzy comprehensive evaluation was then carried out to obtain B_1, representing the final result of the second-level fuzzy comprehensive evaluation of the railway tunnel level III surrounding rock (compression zone) and B_2 the final result of the second-level fuzzy comprehensive evaluation of the railway tunnel level III surrounding rock (tension zone).

$$\begin{aligned} B_1 &= (0.857 \quad 0.3236 \quad 0.3221 \quad 0.17392) \\ B_2 &= (0.85 \quad 0.689 \quad 0.569 \quad 0.174) \end{aligned} \quad (24)$$

By processing the evaluation matrix with the principle of maximum membership degree, the safety level of the railway tunnel was obtained, for the level III surrounding rock monitoring section in tension zone and compression zones, the safety level was I. At this time, the tunnel was in a safe state, which was in line with the actual inspection of the engineering. Similarly, the health

status of various surrounding rock levels of the railway tunnel was evaluated using fuzzy comprehensive evaluation. The results showed that the safety levels of the railway tunnel II and IV surrounding rock were at level I safety status and the safety level of the railway tunnel V surrounding rock at level II safety status.

The safety evaluation system can be applied to most railway tunnels. Through the analysis of different grades of surrounding rock structure, and the safety evaluation of Motianling, Xidashan and other typical railway tunnels. Due to the limited space, this paper only introduced the safety evaluation process of Motianling tunnel. The evaluation method can reflect the influence of various factors, and the evaluation conclusion is clear, accurate and practical, which is consistent with engineering practice. However, the fuzzy comprehensive algorithm also has limitations, and the determination of membership function and weight has certain subjectivity.

CONCLUSION

Safety evaluation of a railway-tunnel structure is a complex research subject. Establishing a practical comprehensive evaluation index system was of great significance for railway health detection. Based on the research and analysis of tunnel structural mechanics models, a safety assessment standard suitable for defect states was proposed here. A fuzzy comprehensive evaluation method was adopted for comprehensively evaluating the safety of railway-tunnel structures. The conclusions were summarized as:

(1) When assessing the railway tunnel, the safety factor was calculated according to the tensile control-bearing capacity of the vault in the range of a 60° central angle of the railway tunnel. At this time, the safety within the range of 60° central angle of the vault was shown to be of great importance for the tunnel design. Equations for the range of the central angle assessment were derived.

(2) Based on fuzzy comprehensive evaluation theory, a safety evaluation model of the railway tunnel structure was established. The membership function model of Gaussian distribution and ladder distribution were used to determine the membership grade of each impact factor and the weight of each factor determined by AHP. The multi-level fuzzy comprehensive evaluation method was used to evaluate the safety of an actual railway tunnel. The evaluation conclusions were examined using practical engineering. The evaluation algorithm comprehensively reflected the impact of various factors, was consistent with engineering practice, had strong practicality, and the evaluation conclusions clear and accurate.

ACKNOWLEDGEMENTS

This work was supported by the National Key R&D Program of China (Nos. 2018YFC0809600 and 2018YFC0809606), the Natural Science Foundation of Liaoning Province (No. 2019-MS-265), and Key Laboratory of the Ministry of Education on Safe Mining of Deep Metal Mines (No. 2019SMDM-KF-A01).

REFERENCES

[1] Li X.J., He F., Wang Y.B. et al., 2014. Tunnel Structure Safety Monitoring System Based on BOTDA Technology. Applied Mechanics and Materials, vol. 3368: 281-284.

[2] Ni X., Goodwine B., 2020. Damage modeling and detection for a tree network using fractional-order calculus. Nonlinear Dynamics, vol. 101: 875-891.

[3] Sun H., Liu S., Zhong R., Du L., 2020. Cross-Section Deformation Analysis and Visualization of Shield Tunnel Based on Mobile Tunnel Monitoring System. Sensors, vol. 20: 1006.

[4] Judit G., Joan R.C., Sergi V., 2020. Structural Health Monitoring with Distributed Optical Fiber Sensors of tunnel lining affected by nearby construction activity. Automation in Construction, vol. 117.

[5] Yang S., Zong L., Wang Y., 2011. Review on the research of highway bridges seismic damage assessment. Applied Mechanics and Materials, vol. 1446: 1224-1229.

[6] Hou G.Y., Xie B.B., Hu T., 2017. Fiber sheath effect in tunneling monitoring based on BOTDR technology. Rock and Soil Mechanics, vol. 38: 2441-2447.
[7] Lyu H., Shen S., Zhou A., 2022. Assessment of safety status of shield tunnelling using operational parameters with enhanced SPA. Tunnelling and Underground Space Technology incorporating Trenchless Technology Research, vol. 123.
[8] Fawad M., Koris K., Salamak M. et al., 2022. Nonlinear modelling of a bridge: A case study-based damage evaluation and proposal of Structural Health Monitoring (SHM) system. Archives of Civil Engineering, vol. 68: 569-584.
[9] Wierzbicki S., Pióro Z., Osiniak M., 2022. Laser-inclinometric method for displacement measurements in structural health monitoring. Archives of Civil Engineering, vol. 68: 607-616.
[10] Kazaras K., Kirytopoulos K., Rentizelas A., 2012. Introducing the STAMP method in road tunnel safety assessment. Safety Science, vol. 50: 1806-1817.
[11] Ou G., Jiao Y., Zhang G., 2021. Collapse risk assessment of deep-buried tunnel during construction and its application. Tunnelling and Underground Space Technology incorporating Trenchless Technology Research, vol. 115.
[12] Guo K., Zhang L., 2021. Multi-source information fusion for safety risk assessment in underground tunnels. Knowledge-Based Systems, vol. 227.
[13] Zhou S., Xiang Q., Wang Y., 2014. The Evaluation Method for Tunnel Structure Health Condition Based on Asymmetric Proximity. Applied Mechanics and Materials, vol. 2014: 1721-1727.
[14] Wang H., Noori M., Zhang J., 2016. A Wavelet-energy based damage identification method for steel bridges. Proceedings of the International Conference on Smart Infrastructure and Construction, vol. 2016.
[15] Pan Q., Dias D., 2017. Safety factor assessment of a tunnel face reinforced by horizontal dowels. Engineering Structures, vol. 142: 56-66.
[16] Alexakis H., Makris N., 2013. Minimum thickness of elliptical masonry arches. Acta Mechanica, vol. 224: 2977-2991.
[17] Yuan W., Guo A., Li H., 2017. Seismic failure mode of coastal bridge piers considering the effects of orrosion-induced damage. Soil Dynamics & Earthquake Engineering, vol. 93: 135-146.
[18] Liu X., Liu Y., Qu W., 2016. Internal force calculation and supporting parameters sensitivity analysis of side piles in the subway station excavated by Pile-Beam-Arch method. Tunnelling and Underground Space Technology incorporating Trenchless Technology Research, vol. 56: 186-201.
[19] Zhong C., Yang Q., Liang J., 2021. Fuzzy comprehensive evaluation with AHP and entropy methods and health risk assessment of groundwater in Yinchuan Basin, northwest China. Environmental Research, vol. 204: 111956-111956.
[20] Bai H., Wang N., 2010. Research on the selection of scale in AHP. IEEE, vol. 2010.
[21] Zul I., Indrani S., Adi A.J., 2022. Analysing dimensions and indicators to design energy education framework in Malaysia using the analytic hierarchy process (AHP). Energy Reports, vol. 8: 1013-1024.
[22] Hamidah M., Hasmadi I., 2022. Development of a protocol for Malaysian Important Plant Areas criterion weights using Multi-criteria Decision Making-Analytical Hierarchy Process (MCDM-AHP). Global Ecology and Conservation, vol. 34: e02033.
[23] Li T., Yang B., 2010. Study on green logistics operation system of port based on AHP-fuzzy comprehensive evaluation. IEEE, vol. 2010.
[24] Zhang J.W., Wang S., Huang H.X., 2014. Study on Classification and Regulation for Defects on Railway Tunnel. Applied Mechanics and Materials, vol. 3307: 1207-1211.
[25] Wang Q., Yang J., Liang Y., 2020. Prediction of time-dependent behaviour of steel–recycled aggregate concrete (RAC) composite slabs via thermo-mechanical finite element modelling. Journal of Building Engineering, vol. 29: 101191.